DISSERTATION

submitted to the
Combined Faculties of the Natural Sciences and Mathematics
of the Ruperto-Carola-University of Heidelberg, Germany
for the degree of
Doctor of Natural Sciences

put forward by
Stephan Helmrich

born in Saalfeld, Germany
Oral examination: July 13th, 2018

Phase structure and dynamics of driven-dissipative Rydberg spin systems

Referees: Prof Dr Shannon Whitlock

Prof Dr Thomas Gasenzer

I follow the Moskva
And down to Gorky Park
Listening to the wind of change

An August summer night
Soldiers passing by
Listening to the wind of change

The world is closing in
And did you ever think
That we could be so close, like brothers

The future's in the air
I can feel it everywhere
Blowing with the wind of change

Take me to the magic of the moment
On a glory night
Where the children of tomorrow dream away
In the wind of change

Take me to the magic of the moment
On a glory night
Where the children of tomorrow dream away
In the wind of change

The wind of change blows straight
Into the face of time
Like a storm wind that will ring
The freedom bell for peace of mind
Let your balalaika sing
What my guitar wants to say

Scorpions
Wind of Change

This thesis investigates the
non-equilibrium behaviour of
a synthetic physical system created
with the depicted complex machinery,
but the theme of this work is very general.
This theme is to explore, to document,
and to understand change. Change defines history,
captured by this song text during the fall of the Soviet Union, reminding me of how these
events shaped personal lives like my own, and how change defines my research.

Abstract

This thesis presents several experiments investigating the regimes of behaviour of a prototypical open quantum many-body system far away from equilibrium. The experimental platform is based on ultracold atoms laser-excited to Rydberg states, which we engineer to emulate a strongly interacting, driven-dissipative quantum spin system. The high degree of control over the relevant microscopic processes and their parameters, as well as the ability to widely tune interaction and driving strengths provides the means to address fundamental questions on how different regimes of dynamical behaviour emerge in complex open quantum systems and how they can be characterised.

In the first part, we discuss how control over the relevant properties of Rydberg spin systems, like temperature, density, long evolution times, strong interactions, tunable driving, and dissipation can be achieved. We introduce the new experimental apparatus developed during this thesis, which combines both single-photon and two-photon Rydberg excitation schemes with high atom densities and long excitation times using an optical dipole trap. Additionally, we investigate theoretically how long coherence times exceeding motional timescales combined with strong many-body interactions can be achieved in such a system. We identify an optimal parameter regime for two-photon excitation where such conditions can be generated with coherence times and interaction strengths comparable to what is achievable for single-photon excitation.

In the second part we explore the macroscopic non-equilibrium behaviour of our system and devise suitable observables for characterising different regimes of behaviour. We discover that the slow atom loss inherent to our system provides a convenient observable for the many-body state of the system. Focussing on evolution times where the effect of the atom loss on the evolution is small, we discover that the rate of atom loss exhibits powerlaw scaling with the driving strength over several orders of magnitude. The measured scaling exponents reveal the non-equilibrium phase structure of the many-body system and allow us to distinguish dissipation-dominated, paramagnetic and critical regimes, as well as an instability. In the observed critical regime, collectively enhanced driving dominates over dissipation, leading to scaling associated to the critical point of the non-dissipative equilibrium Rydberg spin system. Based on the known microscopic processes of our system, we perform classical many-body rate equation simulations, which agree well with the observed phase structure as well as the position and associated scaling exponents of the individual regimes. These findings open up new means to study and classify out of equilibrium systems based on slow particle loss and powerlaw scaling.

In the last part of this thesis we reveal a second type of criticality in our system, which is genuinely non-equilibrium in character and arises from an absorbing state phase transition. The critical state of this phase transition dominates the system evolution at late times where particle loss is no longer negligible. We identify self-organisation as the mechanism driving the system to this critical state, which we observe through powerlaw scaling of the non-equilibrium steady-state. These experiments establish Rydberg atoms as a well controlled platform for implementing and exploring models of absorbing state phase transitions and self-organised criticality with unprecedented access to the underlying microscopic properties of the system.

Zusammenfassung

Diese Doktorarbeit handelt über die experimentelle Untersuchung der Verhaltensbereiche eines prototypischen offenen Quantensystems weit entfernt vom Gleichgewichtszustand. Unsere experimentelle Plattform basiert auf ultrakalten Atomen, die mittels Laseranregung an Rydberg-Zuständen gekoppelt werden, um ein stark wechselwirkendes, getrieben-dissipatives Quantenspinsystem nachzubilden. Der hohe Grad an Kontrolle über die entscheidenden mikroskopischen Prozesse und deren Parameter, sowie die Fähigkeit die Stärke der Wechselwirkung und des Antriebs über einen weiten Bereich einzustellen, erlaubt es uns grundlegende Fragen über die Emergenz verschiedener Regime des dynamischen Verhaltens komplexer Quantensysteme und deren Charakterisierung zu behandeln.

Im ersten Teil erörtern wir wie die Kontrolle über die entscheidenden Eigenschaften des Systems wie Temperatur, Dichte, lange Entwicklungszeiten, starke Wechselwirkungen, stimmbarer Antrieb und Dissipation erreicht werden kann. Wir stellen den Versuchsaufbau vor, welcher im Rahmen dieser Doktorarbeit entwickelt wurde und Einzelphoton- sowie Zweiphotonenanregung mit hohen Atomdichten und langen Anregungszeiten in einer optischen Dipolfalle kombiniert. Darüber hinaus untersuchen wir theoretisch, wie Kohärenzzeiten länger als typische Bewegungszeitskalen bei gleichzeitig starken Vielteilchenwechselwirkungen in solchen Systemen erreicht werden können. Wir identifizieren einen optimalen Parameterbereich der Zweiphotonenanregung, für den solche Bedingungen in vergleichbarer Stärke zu Einphotonanregung erreicht werden können.

Im zweiten Abschnitt erforschen wir das makroskopische Nicht-Gleichgewichtsverhalten und entwickeln geeignete Observablen um verschiedene Verhaltensbereiche zu charakterisieren. Wir beobachten, dass der unserem System inhärente langsame Teilchenverlust solch eine passende Observable bietet, und endecken, dass die Teilchenverlustrate über mehrere Größenordnungen eine Potenzabhängigkeit zur Antriebsstärke zeigt. Die gemessenen Skalierungsexponenten offenbaren die nicht-gleichgewichts Phasenstruktur des Vielteilchensystems und erlauben es uns dissipative, paramagnetische und kritische Bereiche sowie eine Instabilität zu unterscheiden. In dem beobachteten kritischen Bereich dominiert kollektiv-verstärkter Antrieb über Dissipation, was zu Skalierungsverhalten verbunden mit dem kritischen Punkt des nicht-dissipativen Gleichgewichtssystems führt. Basierend auf den bekannten mikroskopischen Vorgängen führen wir Simulationen mit klassischen Vielteilchen-Ratengleichung durch, welche in guter Übereinstimmung mit der beobachteten Phasenstruktur wie auch mit der Position und den Skalierungsexponenten der einzelnen Bereiche sind. Unsere Resultate eröffnen neue Möglichkeiten zur Untersuchung und Klassifikation von Nicht-Gleichgewichtssystemen basierend auf langsamem Teilchenverlust und Skalierungsverhalten.

Im letzten Teil dieser Arbeit decken wir einen zweiten Typ kritischen Verhaltens auf, welcher einen originären Nicht-Gleichgewichts-Charakter hat und von einem absorbierenden Phasenübergang herrührt. Der kritische Zustand dieses Phasenübergangs beherrscht die Systementwicklung zu Zeiten, bei denen der Teilchenverlust nicht vernachlässigbar ist. Wir bestimmen Selbstorganisation als den verantwortlichen Mechanismus, welcher das System in diesen kritischen Zustand treibt, was wir durch die Potenzabhängigkeit des Nicht-Gleichgewichts-Stationärzustands beobachten. Diese Experimente etablieren Rydberg-Atome als eine wohl-kontrollierte Plattform zur Erforschung von Modellen absorbierender Phasenübergange und selbstorganisierter Kritikalität mit beispiellosem Zugang zu den zugrundeliegenden mikroskopischen Eigenschaften des Systems.

List of publications

The results presented in this thesis have led to the following manuscripts and peer-reviewed publications, which have been written and published during the course of my doctoral studies:

- **Uncovering the non-equilibrium phase structure of an open quantum spin system**
  S. Helmrich, A. Arias and S. Whitlock
  arXiv:1605.08609v3, submitted to Physical Review X

- **Observation of self-organised criticality in an ultracold atomic gas**
  S. Helmrich, A. Arias, G. Lochead, M. Buchhold, S. Diehl, S. Whitlock
  Manuscript in preparation

- **Two-body interactions and decay of three-level Rydberg-dressed atoms**
  S. Helmrich, A. Arias, N. Pehoviak and S. Whitlock
  Journal of Physics B: Atomic, Molecular and Optical Physics 49, 03LT02 (2016)

The author furthermore contributed to the following publication:

- **Versatile, high-power 460 nm laser system for Rydberg excitation of ultracold potassium**
  A. Arias, S. Helmrich, C. Schweiger, L. Ardizzone, G. Lochead, S. Whitlock
  Optics Express 25, 14829 (2017)

Contents

Many-body physics far away from equilibrium

1

"All happy families are alike; each unhappy family is unhappy in its own way."
Leo Tolstoy, Anna Karenina

"To paraphrase Leo Tolstoy's quote about happy and unhappy families, all forms of equilibrium matter are alike whereas every form of non-equilibrium matter seemingly behaves in its own way."
Victor Gurarie, Quantum Phase Transitions Go Dynamical [1]

It is one of the most astonishing and fundamental phenomena in nature that an aggregation of many relatively simple interacting objects, i.e. a many-body system, can develop complex structures characterised by behaviour quite distinct from that of the individual object. This notion was perhaps captured most eloquently and famously by the condensed matter physicist Philip Anderson, who summarily declared *"more is different!"* [2] In his seminal work Anderson observed that new levels of complexity emerge on all scales of nature, each characterised by distinct properties which often are almost intractable to describe from fundamental principles. [3, 4, 5] For example, the shape and stability of atomic nuclei is very difficult to predict from the fundamental interaction properties of protons and neutrons [6, 7]. Turning to larger scales, the structure and intricate folding of proteins are not obviously given by the bound atoms [8]; and again on an entirely different scale, living organisms rely on complex self-regulating and self-organising mechanisms to maintain their function and to maintain life [9], which goes far beyond a mere soup of complex molecules [10]. Also in physical systems an overwhelming range of complex many-body phenomena has been uncovered and studied. Illustrative examples are the versatile phases and properties of materials, e.g. of semiconductors or glasses [11], as well as the crossing of phase transitions between different phases. In dynamically evolving systems, one investigates for example the different regimes of turbulence in fluid flow, or the spontaneous formation of intricate patterns like in snowflakes [5]. Even the universe itself is well known to be organised in a hierarchy of complex structures ranging from stellar systems and galaxies to galaxy clusters and super-clusters [12, 13].

A unifying property of many of these complex systems is that they are evolving in time, which can be observed for example by the motion of objects resulting in transport and currents and the formation of new structures in time. Such systems are not at rest, because the external forces acting on them are unbalanced, giving rise to a dynamical system evolution. This condition of a system is called non-equilibrium. This certainly applies to the universe as a whole, which is packed full with complex structures and is still very young on the timescale of the lifetime of stars like the sun, and therefore out of equilibrium ever since its volatile big bang creation. [5] It should not be a surprise then that most subsystems of the

universe, including our daily environment and physical systems, also are out of equilibrium typically. It should also not be a surprise that big branches of sciences are bent on analysing, predicting and modelling properties of complex non-equilibrium systems, including those mentioned above. However, strong quantitative measurements or predictions are often hard to obtain for "natural" systems, since it usually is not possible to directly access or manipulate the individual constituents or important system parameters, or to repeat an experiment. Many "natural" systems are also highly interconnected and governed by many different processes and system parameters, making their investigation even more difficult. Furthermore, unlike in equilibrium settings there is no unifying statistical framework for non-equilibrium settings available, inhibiting general predictions [14]. For these reasons it is typically very difficult, requiring extensive numerical and computational efforts, to establish quantitative connections between the microscopic details governing a non-equilibrium system and the observed complex macroscopic behaviour, as well as between theory predictions and experimental measurements.

To address questions like, on what microscopic details does complex and non-equilibrium macroscopic behaviour depend, what are the regimes of qualitatively different behaviour, or how this behaviour changes with the various parameters characterising a system, one can study artificial laboratory systems, which are simpler than "natural" systems, but still truly complex many-body systems. Such laboratory systems can for example be isolated from many environmental influences, have controllable system parameters, can be probed repeatedly, and have known microscopic details allowing for model descriptions. Especially physical phenomena can be isolated and studied that way, since they often are based on rather simple, inanimate and well-controllable constituents. One class of systems, which in the last decade have developed into a versatile testbed for non-equilibrium physics, are synthetic quantum platforms. These systems can, in general, be isolated from most environment couplings, have known and controllable microscopic details, have diverse means for manipulation and measurement, and their model description is founded on quantum mechanical principles. Furthermore, they can be used to study both classical (for strong dephasing of quantum mechanical coherences) and quantum non-equilibrium phenomena. However, a full theoretical prediction of the macroscopic behaviour of quantum many-body systems typically is impossible, such that experiments on quantum systems are a vital tool for advancing our understanding of complex many-body systems.

In this thesis, we will explore the non-equilibrium behaviour of a prototypical open quantum spin system, which is based on an experiment employing ultracold atoms laser-excited to Rydberg states. It is governed by strong interactions, external driving and dissipation, making its evolution genuinely non-equilibrium. We will experimentally explore the non-equilibrium dynamics of our system, map out its phase structure of non-equilibrium behaviour, and qualitatively and quantitatively elucidate the mechanisms leading to the observed many-body behaviour.

In this chapter we will summarise general characteristics of non-equilibrium conditions and discuss how non-equilibrium conditions can in general lead to the dynamical formation of complex many-body behaviour. We will furthermore highlight a selection of physical phenomena arising under non-equilibrium conditions, including turbulence, thermalisation, and non-equilibrium phase transitions. Thereafter we will outline a range of synthetic quantum platforms which are used to explore non-equilibrium physics. From these, we will introduce our platform of ultracold atoms driven to Rydberg states in more detail. Finally, this chapter will conclude by presenting an outline of the work presented in this thesis.

1.1 Complexity in non-equilibrium conditions

Systems in nature as well as artificial systems in the laboratory typically are open and in contact with an environment of one or several reservoirs, with whom the system will exchange energy, particles, or other conserved quantities. These couplings act on the microscopic level of many-body systems, but may drive macroscopic currents through the system which lead to a dynamical evolution. Such internal currents can be electric conduction, the flow of liquid media or the transport of excitation to name a few. Such non-equilibrium behaviour corresponds to finite probability currents between microstates, i.e. the microscopic configurations of the system, which is called broken detailed balance [14]. The probability currents between microstates are driven by free energy provided by the couplings to external reservoirs, such that the macroscopic entropy of a non-equilibrium system is not maximal and the macroscopic temporal evolution is in general not reversible.

Equilibrium arises naturally from non-equilibrium conditions through thermalisation in the limit that all currents of exchange with the environment, and all internal currents of the system have decayed. Typically, the internal currents characterising non-equilibrium lead to dissipation of free energy and to the relaxation towards equilibrium, such that in the thermodynamic limit, i.e. for systems with many degrees of freedom, fluctuations between microstates are marginal. In this case the system is said to obey detailed balance. Figure 1.1 illustrates the differences between a system at equilibrium and a system out of equilibrium, where equilibrium essentially is the situation where nothing changes, while away from equilibrium various processes happen, e.g. converting potential energy into fluid flow, into electric current, into marvellous new things like chocolate.

At equilibrium, statistical mechanics provides powerful tools connecting the probability distribution of microstates with the macroscopic properties of the system [15]. Away from equilibrium, the probability distribution may be dynamical, allowing for complexity, but no unifying, generally valid formalism has been found yet to describe the behaviour of such systems. Instead, case-specific master equations may be employed to describe the probability distribution of the microstates [14], highlighting that typically no non-equilibrium phenomenon is like the other. Thus investigating and classifying non-equilibrium behaviour poses a challenging research frontier both for experiment and theory.

The state and dynamical evolution of a non-equilibrium many-body system depends on a variety of system parameters, for example the interactions between the constituents, the couplings to the environment and the initial conditions. The environmental couplings can be distinguished between those that drive redistribution currents by adding energy or particles, and such couplings that dissipate energy or particles. Typical driving scenarios resulting in non-equilibrium behaviour are potential gradients or quenches of a potential, while typical dissipation mechanisms are friction, diffusion and the spontaneous emission of radiation. Dissipative processes can be conserving (e.g. diffusion) or non-conserving (e.g. spontaneous emission). In laboratory systems, desired coupling and interaction strengths are free tuning parameters or may even be engineered, the initial conditions may be controlled, and the system may also be isolated against undesired environment couplings. The routinely achieved high degree of control over synthetic open systems and their flexibility make them an ideal platform for studying non-equilibrium behaviour. In the next section we will introduce a selection of such phenomena which can be realised and studied in laboratory experiments.

1.2 Complex phenomena in non-equilibrium physics

Non-equilibrium phenomena can be categorised broadly into two different classes [16, 5]: On the one hand there are phenomena driven by a continuous injection and loss of energy or particles, such that the state of the system is maintained away from equilibrium. On the other hand a system can be brought out of equilibrium by a quench, i.e. changes in system parameters effected by the environment, with subsequent relaxation to a new equilibrium state, called thermalisation. In the following we will give a range of examples for both cases, demonstrating the wealth of non-equilibrium phenomena in physics.

The exact process of how a system reaches its thermal steady state remains a very active field of research. One example is fluid flow, where the relaxation dynamics of both quantum and classical fluids may be governed by turbulent flow due to the competition between driving and dissipation (here friction due to the finite viscosity of the fluid). Understanding turbulence in classical fluids, for example the transition from laminar flow to turbulence, remains a challenging problem in classical physics [17, 18] with tremendous applications for instance in atmospheric physics, the formation of stellar systems and engineering. Another example are material properties after rapid quenches. By way of supercooling of liquids, i.e. the abrupt reduction of temperature, a liquid can be brought into an amorphous aggregate state, the glass phase, instead of a crystalline phase [11, 19]. Closely connected to the glass transitions are (physical) ageing phenomena, i.e. extremely slow relaxation dynamics in the glass state, which shows universal non-equilibrium properties of the dynamical evolution [20, 19, 21, 22]. In quantum systems, prethermal fixed points

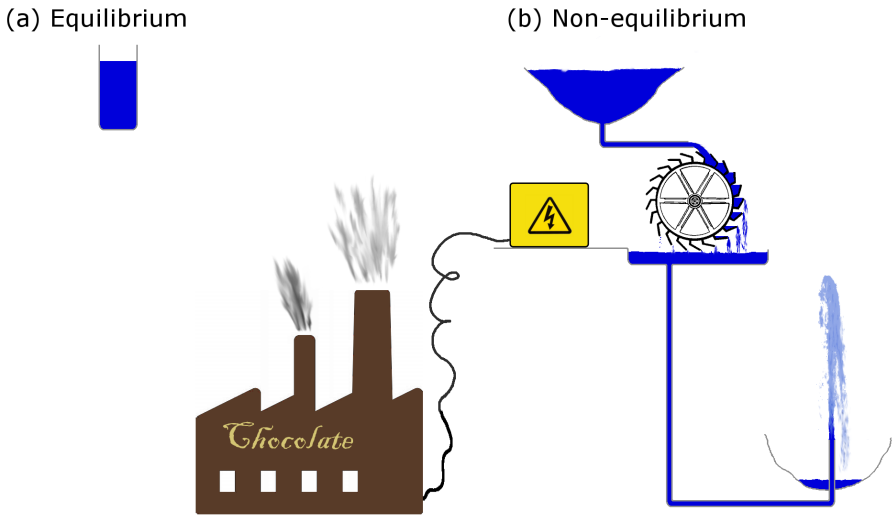

Figure 1.1: Equilibrium versus non-equilibrium, illustrated by a simple water-flow system. At equilibrium (a) there is no external driving mechanism and the water surface becomes balanced and flat representing detailed balance. Only out-of-equilibrium (b) water is driven to flow from the top reservoir to the bottom by gravity. This water flow represents the internal probability currents characterising a non-equilibrium system. This flow may drive other processes, like the water wheel and the fountain. It can also lead to an exchange of particles or energy with other adjacent systems, which we illustrate by the conversion of potential energy into an electric current, which again may drive machines producing the products our societies rely on. In all these non-equilibrium processes energy is dissipated, which we illustrate as the steam emitted by the factory chimneys.

have been revealed to govern thermalisation [23, 24, 25, 26, 27, 28]. A further type of non-equilibrium phenomena has been observed in artificial isolated quantum systems after a quench, so called dynamical phase transitions [1, 29, 30]. Here, the redistribution dynamics between eigenstates of the underlying Hamiltonian [31] shows non-analyticities signifying an abrupt change in system behaviour. Dynamical phase transitions were first observed in [31, 32] for chains of trapped ions emulating a transverse-field Ising model.

Continuously driven systems do not thermalise to an equilibrium state, since detailed balance is broken for all times, but may relax to a non-equilibrium steady state which characterises the system. For example, the transport of both non-interacting classical or quantum waves can reach distinctly non-equilibrium steady states in the presence of a disordered medium, where interference leads to the absence of diffusion. This phenomenon is called Anderson localisation [33], which has been studied for example with light [34, 35] and matter waves [36, 37]. An analogue to Anderson localisation exists for interacting quantum many-body systems, called many-body localisation [38, 39, 40, 41], where an isolated disordered quantum system fails to thermalise in the presence of strong interactions and instead retains some memory of its initial conditions. Building on this effect, isolated quantum systems with periodic driving have been shown to have periodic order and broken symmetry in time, an effect termed discrete time crystal [42, 43]. Further types of continuously driven systems showing non-equilibrium behaviour are driven-dissipative systems, with well-known phenomena being lasing and superradiance. The working principle of lasing is based on population inversion of a gain medium by an external pump, such that stimulated emission of electromagnetic radiation can lead to amplification of directed coherent light [44]. Superradiance is a non-equilibrium phenomenon in quantum optics, where collective coherent interaction of many emitters with a common light field leads to amplified spontaneous emission [45, 46, 47]. As a last typical phenomenon in continuously driven-dissipative systems we would like to introduce pattern formation and self-organisation [5], with well-known examples being the aforementioned turbulence in fluid convection, growth of snowflakes in supersaturated water vapours, solitonic waves and many others.

Phase transitions are manifestations of complexity which are of special importance in physics. Although mostly studied in the thermal equilibrium limit, they nonetheless require external control to tune system parameters to the critical point of a phase transition, or to quench the state of a system across a phase transition as discussed above. We also introduced phase transitions which are genuinely non-equilibrium in nature. Among these, non-equilibrium phase transitions characterised by absorbing states are an important class so far unmentioned, which have been conjectured as a mechanism governing the behaviour of many natural and artificial systems, including the system of Rydberg atoms studied in this thesis [48, 49, 50, 51]. Therefore we will in the following introduce the notion of phase transitions and their characteristic critical states in general, as well as of absorbing state phase transitions specifically.

1.2.1 Phase transitions and critical states

Different phases of matter are characterised by their respective distinct behaviour, which is typically described by an order parameter. If the behaviour of a system changes abruptly from one phase to another at a specific point of a system parameter, one speaks of a phase transition. At the phase transition, the order parameter is non-analytic [14]. One

distinguishes two types of phase transitions. First order phase transitions require the absorption or emission of a fixed energy density resulting in the coexistence of mixed phases at the phase transition and hysteresis effects upon dynamical crossing. Typical examples are boiling (condensation) of water and melting (freezing) of ice, but also the quantum Ising model with antiferromagnetic interactions in a longitudinal field, which shows a first order phase transition from antiferromagnetic to ferromagnetic order [52]. Second order phase transitions show a continuous transition of the entire system without phase coexistence, such that the phase transition is pinned to a singular point, the so called critical point, of a system parameter. Also second order phase transitions are abundant in nature with critical opalescence in alcohol-water mixtures, the liquid-gas transition at the critical temperature or the classical ferromagnetic Ising model at the critical temperature.

Second order phase transitions have been most intensely studied in equilibrium settings and have been shown to arise from dynamically formed long-range correlations which diverge at criticality. This has fundamental implications for the critical system, since at the critical point fluctuations dominate over microscopic details on all scales: The susceptibility to an external conjugate field diverges at the critical point, to which there is no analogous quantity in a first order phase transition [53]. In the vicinity of the critical point, all system properties and observables obey scale invariance and thus are given by power laws. It is this scale invariance which makes critical phenomena unique in nature and intensely investigated. Crucially, it renders the critical system independent of its microscopic details, a property called universality. Then only a few scaling exponents suffice to characterise the phase transition, which only depend on the number of spatial dimensions, the number of components of the order parameter and the symmetries of the interaction. This implies that totally unrelated systems can show identical critical behaviour, it is then said that they fall into the same universality class. A celebrated example of universality is the Ising universality class [54] encompassing both the aforementioned classical ferromagnetic Ising model and the critical liquid to gas transition.

It may seem surprising that the given phenomenological definition of a phase transition also applies away from equilibrium [55]. Even though detailed balance is broken, concepts like criticality, diverging fluctuations and universality hold nonetheless. A well known class of non-equilibrium critical behaviour in driven-dissipative systems are the absorbing-state phase transitions, which we will discuss in the following.

1.2.2 Absorbing state phase transitions

A second order non-equilibrium phase transition between an absorbing and an active phase is called an absorbing state phase transition. The active phase is characterised by sustained dynamical evolution at all times and finite fluctuations of the local order parameter, while the absorbing phase is governed by a set of microstates at which the evolution stops and all fluctuations freeze out fully. Such a state can not be left again by the system and is therefore also called inactive. [14] In many systems, this macroscopic irreversibility of the system evolution arises directly from irreversible microscopic dynamics. Typical microscopic processes leading to absorbing states distinguish between active and inactive states of a lattice site. To give an example, we will focus on driven-dissipative processes illustrated in Figure 1.2(a). Here, external driving causes active sites to spread by flipping an inactive site next to an active one to active also (branching), or leads to the inverse process (coalescence). Dissipation, here in the form of decay of active sites to inactive,

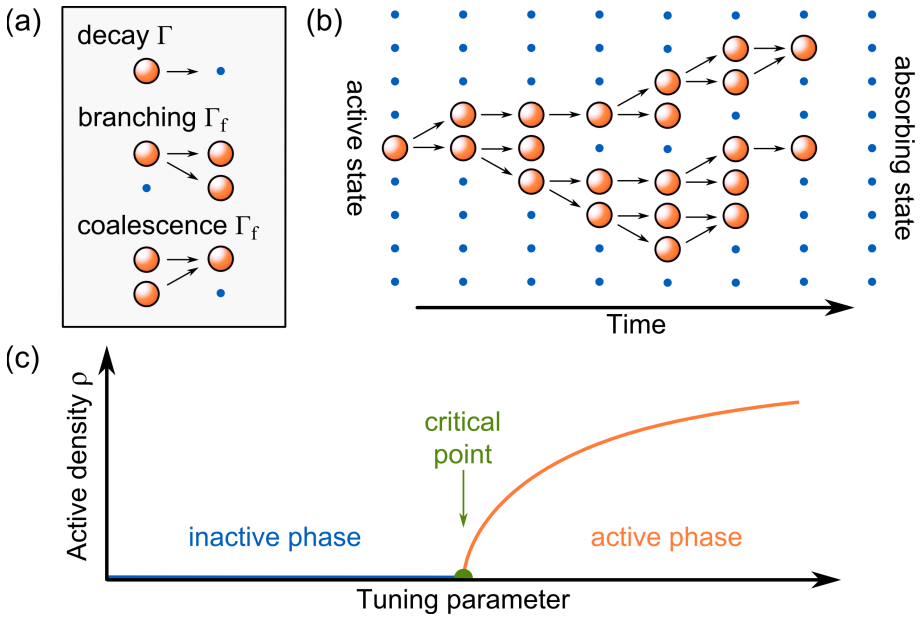

Figure 1.2: Example of an absorbing state phase transition. Here, the medium consists of a regular lattice of sites which are either in a low energy state called inactive (e.g. unoccupied or unexcited) represented by small blue circles, or in a high energy state called active (e.g. occupied or excited) represented by large orange spheres. The state of the system evolves stochastically via the microscopic rules depicted in panel (a). A high energy state may decay spontaneously, but the inverse process is forbidden. Importantly, this encodes irreversibility of time microscopically. Furthermore, active sites may spread to nearest neighbours (branching) or recombine (coalescence). Panel (b) illustrates one possible evolution scenario where the system was initialised with one active seed, leading to spreading of activity for intermediate times. But eventually the system decays fully into the absorbing state, which can not be left by the rules of panel (a). At long times, the system is characterised by a non-equilibrium steady-state with an active density ρ, depicted in panel (c). ρ is the order parameter of the system, showing a second order phase transition between inactive and active phases.

break time reversal symmetry explicitly, giving rise to genuinely non-equilibrium dynamics. A system in the absorbing state can not leave this state by the given microscopic rules, making absorbing states non-fluctuating, as is illustrated by the example evolution depicted in Figure 1.2(b). The phase transition is characterised by the density of active sites, which in the late time limit is zero in the inactive phase and finite in the active phase (Fig. 1.2(c)). The competition between driving and decay rates is a tuning parameter of the system, which has to be adjusted precisely to reach the critical transition value.

Maybe the most intensely studied class of absorbing state phase transitions is the directed percolation (DP) universality class. A large variety of systems are thought to fall into this class, e.g. catalytic reactions, granular flow, calcium dynamics in cells, turbulence and others. [14] Also the processes illustrated in Figure 1.2 lead to directed percolation. Most research in the field of absorbing state phase transitions has focussed on theoretical model systems, while only very few successful implementations in experiments exist. In the case of directed percolation, only very recently an experiment on turbulent liquid crystals [56] and two on turbulent channel flow [57, 58] were able to demonstrate that these systems both fall into the DP universality class. Research on absorbing state phase transition has

been exclusively focussed on classical dynamics, with extensions to coherent evolution recently considered in [50] and potentially enabled by modern synthetic-quantum-systems experiments. For an experimental platform based on Rydberg atoms an absorbing state phase transition was recently reported in [48].

Extending the processes of absorbing state phase transitions to open systems including external particle loss and particle addition leads to completely new behaviour and in specific limits to self-organised criticality (SOC). Here, the system drives itself, via particle exchange with the external reservoir, to the critical state of the absorbing state phase transition, such that no fine tuning of system parameters is required for the system to be critical. Pure self-organised criticality arises in a double limit of infinitely separated time scales, where the external dynamics is infinitely slower than the internal dynamics and the particle loading is infinitely slower than the particle loss.[1] Then on all time scales particle loading will increase the total population density n of an absorbing state ($\partial_t n > 0$) till the critical population is reached and the system becomes active, while the particle loss decreases the overall population density in the active state ($\partial_t n < 0$) till the system becomes subcritical. Therefore the particle density in the non-equilibrium steady-state is independent of the initial state of the system and independent of the system parameters. The state of the system fluctuates around the critical state which was reached by a self-organisation process. Thus the critical point is an attractor of the evolution. This self-organised criticality is characterised by internal redistribution avalanches with powerlaw distribution. The avalanche dynamics is critical in the sense that it shows self-similarity between small and large scales and that the average avalanche size diverges for infinitely large systems [59].

SOC has been conjectured as one possible fundamental mechanism behind the observed abundance of natural phenomena with apparent powerlaw distributed behaviour ranging from the activity in electrical circuits [60, 61], neural networks [62] and stock markets [59], to the distribution of avalanches and earthquakes [63], and to the spread of diseases [64], forest fires [65], or even how ideas spread across social networks [66]. SOC has for example been observed in rice piles [67], vortex avalanches in type-II superconductors [68] and neuronal spike avalanches in brains [69, 70]. In many of these cases the scientific debate is ongoing whether the considered systems show true SOC [71, 72], especially if the internal driven-dissipative dynamics violates local energy conservation [73, 69, 71], or whether SOC is sufficient as a mechanism to lead to observed powerlaw distributions across many orders of magnitude in system parameters [72]. Since many well studied theoretical models apply to systems where direct laboratory experiments are difficult, like earthquakes or epidemics, great importance comes to clean experimental analogues to address the unresolved questions in new ways.

In the next section we will introduce synthetic quantum systems as novel platforms where non-equilibrium behaviour may be observed in the quantum realm, but also in the classical limit. Due to their high degree of isolation, control and engineerability these platforms open up new paths to address fundamental questions in non-equilibrium physics and to establish quantitative links between experiments and theory models.

[1] For loading rate $a \to 0^+$ and loss rate $b \to 0^+$ we require $a/b \to 0$, such that loading effectively only happens after all activity has stopped. If the limits are only realised approximately a finite cut-off time scale emerges.

1.3 Experimental approaches to non-equilibrium physics based on synthetic quantum systems

In the last decade a new kind of laboratory systems has evolved which are genuinely non-equilibrium. Broadly speaking, these are synthetic open quantum systems characterised by external driving, dissipation and many-body interactions. The strength of the quantum approach lies in the ability to isolate a tailored state-space with well-known microscopic processes such that accurate models can be formulated. Even more, a variety of tools allows experimentalists to engineer a variety of macroscopic and microscopic system properties like the geometry, dimensionality and (dis)order, interactions, driving and also dissipation. [24, 74, 75, 76]

Synthetic open quantum systems study for example crystals of laser cooled ions [77, 78, 79, 74, 80], which have been employed to reveal the aforementioned time crystals [43] and dynamical quantum phase transition [31, 32] and are for example well suited to create engineered baths interacting with a system in open system quantum simulations [74, 77]. A complementary approach for open-system quantum simulation are superconducting circuits [81, 82, 83]. In yet another approach, resonator cavities can be utilised to shape properties of constituents, especially of driving and dissipation. Driven-dissipative Bose Einstein condensates have been created as exciton-polariton condensates in semiconductor microcavities [84, 85, 86, 87] and with photons in dye-filled microcavities [88, 89], where the short lifetime of the created quasiparticles leads to a competition between many-body coherence and dissipation. Also ultracold atoms in an optical cavity have been studied [90, 91, 92], where the resonator mediates both an open driven environment and controllable long-range interactions, such that the system emulates for example the non-equilibrium phase transition of the quantum Dicke model. Ultracold atoms can also be engineered to exhibit long-range interactions by laser-coupling to highly excited atomic states, so called Rydberg states. This is the approach explored in this thesis, which we will introduce in more detail in the next section.

1.4 Driven-dissipative Rydberg systems

The platform used in our experiments is a laser driven ensemble of Rydberg atoms [93, 74, 94, 95, 96, 97], which are intrinsically driven-dissipative systems [98]. Atoms excited to Rydberg states, i.e. highly excited atomic states, provide exaggerated interaction properties which are both strong and long-range in character. These interaction properties alone have opened many interesting research avenues in the past, ranging from many-body interaction effects like Rydberg blockade [99, 100, 101, 102, 103], exotic quantum phases [104, 105, 106, 107, 108, 109] and ultracold chemistry [110] over quantum non-linear optics [111] and quantum simulation [112, 113] to strongly correlated plasmas [114, 115]. Furthermore, driving and dissipation very naturally arise from the driving of the atomic transition and the finite lifetime of the excited Rydberg states, respectively, making the Rydberg approach a fantastic testbed for non-equilibrium physics.

Ultracold Rydberg atoms fulfil all the criteria for artificial laboratory experiments studying non-equilibrium physics highlighted at the beginning of this chapter. They achieve a high degree of isolation from the thermal environment and isolate an engineered state space with well-known microscopic properties. Interactions, driving and dissipation,

which govern the non-equilibrium dynamics on a microscopic level, can be manipulated by the experimentalist and can be described within the framework of the quantum master equation. Thus it is possible to uncover connections between the microscopic details of the system and observed behaviour on the macroscopic level. Furthermore, the required experimental tools, like laser and vacuum systems, and techniques, like the preparation of ultracold atom clouds and the measurement of suitable observables, are well developed and documented. [96, 97, 112, 74] Using ultracold atom gases coupled to Rydberg states, a range of non-equilibrium phenomena has already been studied in experiment and theory. These include their driven-dissipative dynamics [116, 117, 98, 118, 119, 120], aggregate formation [121, 122, 123], optical bistability [124, 125, 126, 127, 128, 129] and energy transport [130, 131]. Also signatures of an absorbing state phase transition have been reported in [48, 51]. However, the emerging non-equilibrium properties of Rydberg systems due to the competition between external driving, dissipation and many-body interactions remain subject of ongoing research, where for example the behaviour of mesoscopic systems [116] or the phase structure of classical disordered clouds [48, 117], of lattice geometries [132, 133] and of quantum degenerate clouds [134] has been examined. Hot topics are, for example, the nature of the non-equilibrium quantum states in the presence of dissipation [50, 135, 51, 133], the existence of metastable or bistable states [126, 127, 124], or the possibility to create novel phases of matter based on soft-core interactions [104, 136, 137, 138].

1.5 Outline of this thesis

In this thesis we will discuss and explore the emerging non-equilibrium behaviour of a prototypical open many-body spin system both in experiment and in theory. Based on our discussion of the general properties of complex structures and of non-equilibrium physics, we formulate two guiding questions along which we will develop our investigations:

> How can the dynamics and phase structure of a non-equilibrium system be measured and characterised?
>
> How do the dynamics and phase structure emerge from the microscopic processes of the many-body system?

To address these questions, we have designed a new experimental apparatus for creating open quantum spin systems, devised suitable experimental observables for assessing its non-equilibrium behaviour, and employed suitable models to describe the macroscopic experimental observations microscopically. In the following, we will outline the different parts of this work and their key results.

The work and the findings presented in this thesis are based on the experimental platform introduced in chapter 2, which was developed and set up as part of my doctoral studies. Our setup comprises clouds of ultracold ^{39}K atoms laser excited to Rydberg states, which endow the atoms with strong many-body interactions and dissipation. By preparing this system in ultra-high vacuum conditions it is essentially isolated from coupling to the room-temperature environment (except for blackbody radiation), such that the coherent laser excitation can isolate a two-level quantum system within the electronic level structure of an atom. In this chapter we will introduce the necessary experimental machinery to efficiently create and control ultracold atoms, which comprises a 2D-MOT as an atom

source, a 3D-MOT, a gray molasses stage for cooling to ultracold temperatures, and an optical dipole trap to suspend the atom cloud inside the vacuum chamber. Our setup allows for long interrogation times, which we will explore up to hundreds of milliseconds, much longer than the typical lifetime of excited Rydberg states. The key features of our experimental apparatus are complemented by versatile laser sources for Rydberg excitation, comprising both two-photon and single-photon excitation with strong driving strengths between ground and Rydberg states. In our experiment, important system parameters of the driven-dissipative Rydberg gases can be controlled and manipulated. Specifically, the interaction strength can be controlled by the atom density and the addressed Rydberg state, and the driving properties can be tuned by the strength and detuning of the excitation lasers. In combination, the achieved high degree of control and tunability make our experiments well-suited to experimentally studying emerging many-body behaviour far from equilibrium.

In chapter 3 we introduce the quantum spin system emulated by the Rydberg atoms in our experiments. We will show that the laser driving isolates a two-level quantum system in each atom, the effective spin-1/2, which comprises the atomic ground and the Rydberg states. Thereafter we will discuss how the driving, interactions and dissipation processes arise, which govern the effective spin system at the microscopic level, and introduce the quantum master equation describing the system. Our elaborations will also encompass particle loss inherent to our system, which can lead to non-Markovian feedback at late times compared to the effective inverse particle loss rate. Based on this understanding of the microscopic system details, we will discuss emerging many-body properties of Rydberg spin systems, which arise from the competition between interactions, driving and dissipation. These include collective blockade, facilitation dynamics, the equilibrium phase structure and Rydberg dressing. We will also develop approximate models, which will allow us to efficiently describe our experiments on a microscopic level. This will allow us in the following chapter to bridge the gap between macroscopic observations in the experiment and microscopic system properties, and to characterise the observed phase structure and many-body dynamics.

Chapter 4 will focus on the microscopic processes of the interacting Rydberg spin system and explore ways to control the dissipation of the system and to create many-body systems with long phase coherence times and strong pair-interactions at the same time. The investigated approach will be based on weak Rydberg dressing with large laser detunings, which we study self-consistently with the previously introduced quantum master equation. We will employ this framework to search for suitable dressing conditions with coherence times longer than motional timescales in two-photon dressing comparable to single-photon dressing. This is of specific interest to our experiments, since we are able to utilise both excitation schemes. Our studies will reveal a parameter regime of two-photon dressing, based on cooperative, multiphoton resonances, where two-photon dressing may work effectively.

In chapter 5 we will turn to investigate the macroscopic non-equilibrium behaviour of driven-dissipative Rydberg spin systems, tackling the first guiding question. Investigating the dynamical evolution of the system on timescales where the particle loss acts as a small perturbation to the many-body spin-1/2 system, we will find that dissipation itself provides a powerful tool for characterising the macroscopic behaviour, which we will observe as a loss of population. By measuring atom loss over orders of magnitude in driving strength and detuning, we will be able to uncover scaling properties of the system, which will provide us

with an emergent observable of the non-equilibrium phase structure. We will demonstrate that, depending on the relative strength of driving, dissipation and interactions, our system shows different regimes of non-equilibrium behaviour with clearly distinguishable scaling exponents, which include a dissipation-dominated and a paramagnetic regime dominated by the detuning of the driving field, as well as a critical and an unstable regime. Combining experimental observation and the theoretical tools developed in chapter 3, we will address the second guiding question and elucidate the mechanisms leading to the observed many-body regimes. We will show that the instability originates from facilitation dynamics competing with decay of excited Rydberg states, and that the critical regime arises from a quantum critical point of the non-dissipative equilibrium Rydberg spin system. This demonstrates that the complex non-equilibrium behaviour of Rydberg spin systems is governed by bot equilibrium and non-equilibrium properties.

Chapter 6 will then focus on driving regimes with large laser detunings and strong Rydberg facilitation, and explore the resulting non-equilibrium dynamics on all timescales. At weak driving below the instability we will observe that the paramagnetic regime persists on all timescales. At late times and strong driving above the instability, we will find that the system is characterised by a non-equilibrium steady state with finite atom density, despite the particle loss inherent to our system. We will observe that the steady state density is independent of the initial density and that it follows a powerlaw with the driving strength. These characteristics of the late time phase structure, together with a separation in time scales between the facilitation dynamics and all other processes, will lead us to identify self-organised criticality as a mechanism at work in our system leading to the emergence of genuinely non-equilibrium critical behaviour.

Finally, chapter 7 summarises the main results of the work presented in this thesis and gives an outlook onto possible ramifications of our findings.

Development of a new experiment for non-equilibrium physics using Rydberg atoms

2

To study the dynamical evolution and phase structure of any system in an experiment requires a high degree of sophistication regarding control over microscopic processes as well as strategies of measurement and characterisation. Only then may one hope to gain insight into the mechanisms linking microscopic processes to the observed macroscopic phase structure and dynamics. As we have demonstrated in section 1.3, synthetic quantum systems are established model systems for far-from-equilibrium many-body physics. Their strength lies in isolating a designed quantum state space with well defined couplings to external environments, for which desired properties can be engineered. Therefore synthetic quantum systems provide a high degree of control over initial states and widely tunable system properties such as interactions and environmental couplings. This thesis is based on the experimental realisation and investigating of driven-dissipative Rydberg spin systems. At the beginning of my doctoral studies we developed and build a new experimental apparatus tailored to this task, which will be introduced in this chapter.

Our experiments utilize clouds of ultracold ^{39}K atoms, which are to a large degree thermally isolated from the environment and suspended in an optical dipole trap. We use laser excitation to strongly-interacting Rydberg states with a finite lifetime to create strongly-interacting driven-dissipative spin systems. The non-equilibrium dynamics of our system is ruled by external laser driving (strength Ω and detuning Δ), dissipation due to decay of the excited states and the dephasing induced e.g. by the finite laser linewidth (strengths Γ and γ_{de} respectively) and atomic motion, and van der Waals interactions between excited states (strength C_6/R^6 and atom density n_0). A convenient parameter to characterise the strength of van der Waals interactions between neighbouring Rydberg excitations is $J = C_6 {n_0}^2$. In this chapter we will focus on how these microscopic processes are implemented and controlled in our experiment, and how the thermally isolated quantum system is created. For the quantum mechanical description of our system based on its atmoic details we refer to chapter 3. In the following, we will first summarise the criteria we applied to design our apparatus and to tailor its properties to study non-equilibrium phenomena. In section 2.2 we then discuss the creation and isolation of the atomic medium, and section 2.3 focuses on out implementation id one and two-photon laser driving to Rydberg states.

2.1 Design of the ultracold atoms experiment

The experiments carried out in this thesis rely on a completely new apparatus which was designed and set-up during the first half of my thesis work with the purpose of

studying non-equilibrium dynamics and relaxation of strongly-interacting many-body systems. Specifically, the following design criteria were applied:

Near-complete isolation from the thermal environment: In ultracold atom experiments, a cloud of ultracold atoms is created, which initialises all atoms in the atomic ground state such that specific desired electronic states can be addressed subsequently. This approach requires a near-total isolation from the thermal atmosphere, which can be achieved by placing the experiments inside an ultrahigh-vacuum apparatus. The atoms are cooled and suspended by a series of magneto-optical and optical traps inside the vacuum system, such that any contact with thermal surfaces is impossible. The only remaining thermal coupling to the external environment is via blackbody radiation, which leads to an important decay mechanism of Rydberg states. For Rydberg states with principle quantum numbers $n \gtrsim 30$, as will be used in this thesis, blackbody induced decay dominates over spontaneous decay, with typical total decay rates $\Gamma/2\pi \lesssim 1\,\mathrm{kHz}$.

Strong and tunable driving to Rydberg states: The internal state of the atoms will be manipulated with laser light, thereby driving the whole system away from equilibrium. The driving strength and detuning are key parameters determining the evolution of the system and will be essential tuning knobs for driving the system to different regimes of behaviour. Therefore, these parameters should be tunable over several orders of magnitude. We envisage studying regimes both on resonance and far from resonance, as well as strong and weak driving regimes. For the latter, driving should at least compete with dissipation and dephasing $\Omega \approx \Gamma + \gamma_{\mathrm{de}}$, which will be on the order of 100 kHz.

Good optical access: To manipulate matter with laser light is the core capability of our experiments. Initially hot atoms are cooled by the momentum recoil of impinging directed laser light and the geometry of the final cloud is determined solely by the shape and structure of the optical dipole trap used to suspend the atoms. The thus created ultracold atom cloud will thereafter be addressed for state manipulation by further laser beams and in the end the cloud will be imaged using again an extra laser beam and high-resolution optics. It is essential for the success of our experiments to accommodate all of these laser beams and their corresponding optics around the atom cloud.

High atom densities: The powerlaw nature of the interactions between Rydberg excitations makes the interactions dependent on the atom density n_0, with $J = C_6 {n_0}^2$ characterising the interaction strength. A strongly-interacting regime is only realised for $J > \Omega, \Gamma + \gamma_{\mathrm{de}}$, which is equivalent to $n_0 {r_b}^3 > 1$ [96]. Here ${r_b}^3$ parametrises the interaction volume by the characteristic blockade radius (cf. sec. 3.3.1). Far from resonance ($\Omega, \Gamma + \gamma_{\mathrm{de}} \ll \Delta$) this condition becomes even more stringent with the facilitation radius replacing the blockade radius. Typical interaction radii are several micrometers large, necessitating atom densities $\geq 10^{11}\,\mathrm{cm}^{-3}$. Furthermore, the atom density should be widely tunable such that J independently adjustable.

Long interrogation times: The evolution of a laser driven atomic system will progress in successive cycles of excitation and decay, whose timescales are approximately given by $\Gamma_\uparrow$ and Γ in equation (3.24). In the accessible parameter range the slowest process usually is the single-atom seed creation, which can be as low as $\sim 10\,\mathrm{Hz}$, while typical relaxation rates of the many-body system can be of similar order. To study the non-equilibrium dynamics of a system one would like to be able to cover all time scales up to the formation of a quasi-steady state, requiring long interrogation times of possibly $\sim 100\,\mathrm{ms}$.

Low temperatures and small laser dephasing noise: Dephasing noise is an important limitation for our experiments. As can already be seen from the classical rates

for (de)excitation in equations (3.24), dephasing reduces the occupation probability in the excited state and thus mitigates the impact of the driving strength. Additionally, it reduces the quantum coherence of the transitions and renders the system more classical. Although the many-body evolution in the classical limit is highly interesting in itself, crossing the threshold towards quantum coherent evolution represents an additional and exciting new frontier. Two important factors which dominate the dephasing rate are the frequency stability of the driving lasers and Doppler broadening due to thermal motion of the atoms. To improve their frequency stability, all lasers will be actively stabilised to a high stability reference. To minimise the Doppler effect, we will strive to achieve as low temperatures as possible. However, even at temperatures as low as 1 µK the atoms will still move with a thermal velocity of $\approx 20\,\mu m/ms$. Given the envisaged long interrogation times, motion will not be negligible.

For future experiments: The possibility to create ultracold fermionic or bosonic matter: The apparatus was designed such that both fermionic and bosonic isotopes of the same atomic species can be cooled and trapped. Cooling to ultracold temperatures combined with Rydberg excitation would allow for the investigation of strongly interacting quantum states with either fermionic or bosonic statistics. Among the alkali atoms, which are the most widely used group of atoms in ultracold atom experiments, only lithium and potassium have stable isotopes of both kinds. In our experiments potassium was selected, which was the first fermionic isotope to be cooled to degeneracy [139], because of its higher mass, which suppresses tunnelling in structured traps. However, quantum degenerate gases were not created in this thesis and all experiments were performed with the bosonic ^{39}K in the non-degenerate regime.

For future experiments: Multiple detection capabilities: Besides the manipulation and preparation of non-equilibrium many-body states with a high degree of control and tunability, the measurement capabilities are a central feature of a successfully experiment. For experiments relying on ultracold atoms with Rydberg excitations, typical observation strategies are optical imaging measuring the spatial distribution of atoms and Rydberg excitation counting [96]. The most widely used imaging technique is absorption imaging, which is well suited for fast image taking and large fields of view to study large samples. For high resolution imaging on small scales resolving individual atoms in an optical lattice fluorescence imaging is chosen, employing high resolution objectives with achieved diffraction limited resolutions close to the employed optical wavelengths. Counting of Rydberg excitations provides a second, independent observable, which is measured by electric field ionisation and detection of ions. Our experimental apparatus was designed to incorporate all of these complementary approaches, necessitating multiple optical imaging setups as well as an in-vacuum electric field structure and ion detectors.

Design solutions

To incorporate all the afore-noted design objectives into a single apparatus, we opted for a large-volume ultra-high vacuum steel chamber to house the required in-vacuum components and to allow for many-beam optical access along the horizontal plane and along the vertical and diagonal axes. Inside the central chamber we installed an electrode structure which can be used to both compensate for stray electric fields and to field ionise Rydberg excited atoms. The ions can be detected on two microchannel plates. To allow for high resolution imaging despite the large dimensions of the vacuum chamber, a high

resolution objective lens was installed inside above the electrode structure. This part of the setup is depicted in Figure 2.1. Furthermore, a 2D-MOT acts as an atom source of ^{39}K , which supplies a high flux of atoms facilitating rapid loading. The final trap in our setup is an optical dipole trap, which allows for long Rydberg excitation times and with tunable atom density. Additional gray-molasses cooling is utilised to achieve efficient loading of ultracold and high-density atom clouds into the dipole trap. Finally, we implemented both single-photon and two-photon excitation to Rydberg states, each based on frequency doubling of high-power lasers to reach the desired strong driving regimes (illustrated in Fig. 2.5). In the following we will detail these core features of our apparatus.

2.2 Preparation of the medium

The work horse of our apparatus is an optically trapped atom cloud at temperatures around 10 µK. At such ultracold temperatures all valence electrons will "freeze" to the energy ground state[1], which for potassium is $|4s_{1/2}\rangle$. Thus trapped atoms in their ground state are the starting point of all of our experiments. The experiment procedure is cyclic, starting from hot atoms which undergo a sequence of cooling stages employing different cooling and trapping strategies until an ultracold atom cloud has been prepared. Since we are interested in long laser interrogation times our atom clouds will be held in an optical dipole trap during the Rydberg excitation phase. The optical dipole trap does not lead to electronic excitations, leaving the ground state of the atoms unperturbed at all times except for the trapping potential. This cloud will then be manipulated and probed for experiments and finally be released for destructive absorption imaging. The cycle then restarts anew. In the following we will describe the employed apparatus used to create these atom clouds. Many aspects of the apparatus have been adapted from the Rubidium Rydberg apparatus in Heidelberg, described in [140]. Many of the components of our system, including those specific to ^{39}K , have been described in detail in a series of Bachelor and Master theses [141, 142, 143, 144, 145, 141, 146].

2.2.1 Vacuum system for thermal isolation

To isolate the ultracold atom cloud from the room temperature atmosphere, the atom cloud is prepared inside an ultra-high vacuum chamber, Figure 2.1(a). Pressures as low as 10^{-10} mbar are achieved routinely with a titanium-sublimation pump[2] combined with a 125 l/s ion pump[3]. For trapping and cooling of atoms a dedicated dual chamber system is used, with a large volume science chamber [4] and a separate glass cell for the atom source[5]. The glass cell is connected to the science chamber via a small CF16 aperture, leaving all eight large apertures along the periphery free for optical access. Care was taken to use only components made from stainless steel[6] with low magnetic permeability inside and close to the science chamber to reduce magnetisation effects due to strong changing magnetic fields.

[1] At 10 µK temperature the thermal energy is $k_B T/\hbar \approx 200$ kHz, much lower than the near-optical transition energy from the ground state $|4s_{1/2}\rangle$ to the first excited state $|4p_{1/2}\rangle$, which is ≈ 400 THz
[2] Agilent Technologies; TSP Cartridge Filament Source
[3] Agilent Technologies; VacIon Plus 150 Ion Pump StarCell
[4] Kimball Physics; 8 Multi-CF Spherical Square MCF800-SphSq-G2E4C4A16
[5] The glass cell is AR coated (780 nm) on the outer cell walls and manufactured by Japan Cell
[6] Steel code 316LN

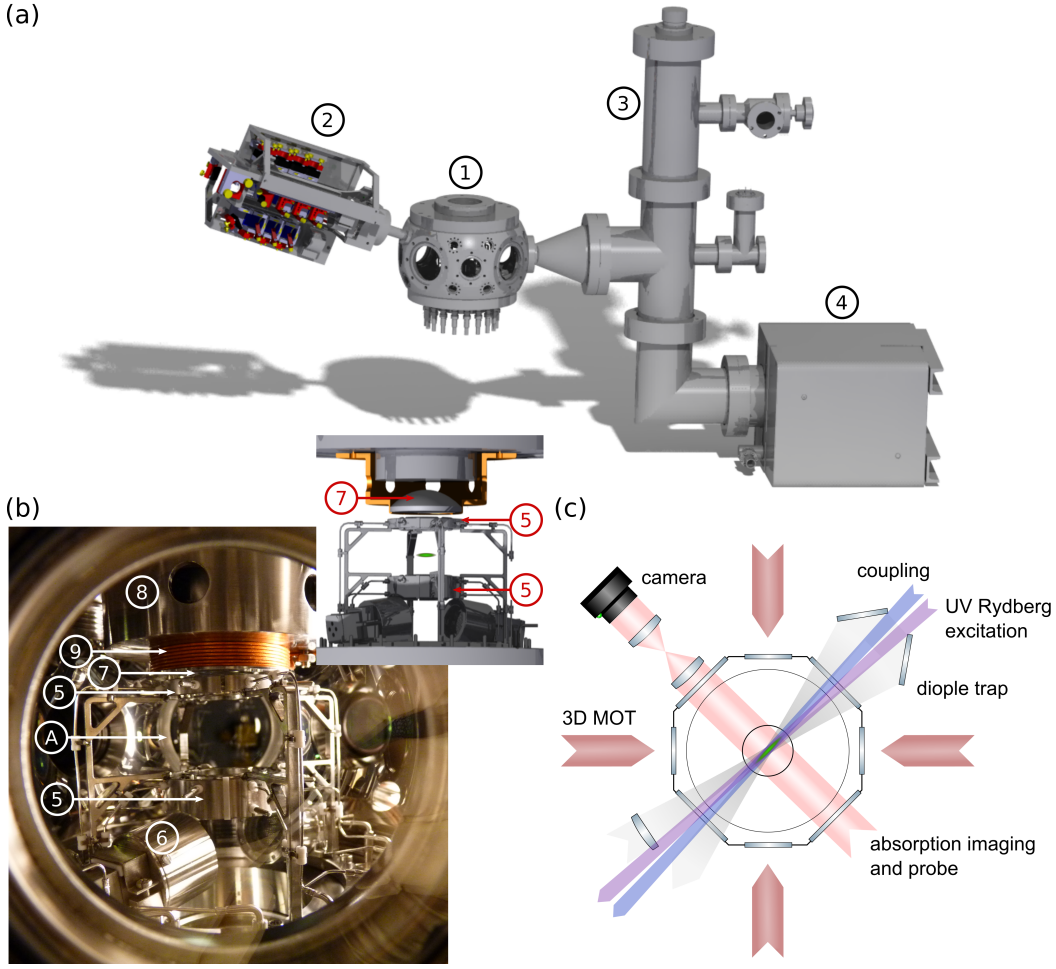

Figure 2.1: The experimental setup for cooling and trapping of atoms. (a) The vacuum system. The apparatus is based on a science chamber ① for atom trapping and manipulation, which is loaded from a separate 2D-MOT atom source ②. The whole vacuum system is maintained at ultra high vacuum by a titanium sublimation pump ③ and a 125 l/s ion pump ④. The science chamber provides optical access via multiple viewports (chiefly top and bottom, 8 sides along the equator) with optics positionable on three breadboard levels around the science chamber (not displayed). (b) Photo of the interior of the science chamber, with a rendering of the same components at the top right. Two rings of electrodes ⑤ are mounted on the bottom flange and placed symmetrically around the atom cloud at the centre of the chamber for electric field control. They are complemented by two microchannel plates ⑥ for detection of field-ionised Rydberg atoms. The atom cloud is depicted in green at the centre of the vacuum chamber rendering (not o scale). The top flange holds a high numerical aperture objective lens ⑦ inside a steel lens holder ⑧ (orange in the rendering). Around the lower part of the lens holder a radio frequency antenna was wound ⑨. The viewport on the top side is recessed inside the chamber to allow close optical access to the in-vacuum lens. (c) Beam geometry around the science chamber. Three pairs of counter propagating beams are used to create the 3D-MOT and the gray molasses at the centre of the chamber. Two dipole trap beams cross at a shallow angle to form a confining optical dipole trap. Here we show the dipole trap beam setup using a retroreflected beam (chapter 5), which was replaced by two independent crossing beams later (chapter 6). Either UV light or probe and coupling light are used to drive the transition from ground to Rydberg states. The atom cloud is absorption imaged on a CCD camera.

The chamber openings are vacuum sealed with viewports made from fused silica. We installed two types of viewports depending on the laser sources to minimise thermal lensing in high-power laser applications, loss from reflection and to prevent damage to the glass. We use five types of laser wavelengths to manipulate the external or internal degrees of freedom of the atoms in our experiments: infrared (IR) light at 1064 nm wavelength for the optical dipole traps, near-infrared light at 767 nm and 770 nm to drive the D2 and D1 transitions of potassium to the first excited state, respectively, blue light at 457 nm to excite from the first excited state to Rydberg states and ultraviolet (UV) light at 288 nm to directly couple from ground to Rydberg states. The most stringent requirements are posed by the UV beam and the high intensity dipole trap beams, which are combined on one chamber axis. Therefore we used a special kind of fused silica for the viewports along this axis, which combines both of these extreme requirements by having a low OH content to minimise thermal lensing by IR absorption and an elevated hydrogen content to suppress damage through UV absorption.[7] These viewports were not anti-reflection coated because of the risk of damage to the coating by high-intensity UV light. All other openings were sealed with viewports allowing for maximum flexibility in future experiments by being anti-reflection coated for all non-UV wavelengths. Among these wavelengths, the far-infrared light requires by far the highest intensities, wherefore an IR-grade fused silica was chosen for the substrate.[8]

Inside the science chamber an intricate electrode structure was mounted, with the purpose of minimising stray electric fields and counting Rydberg excitations via field ionisation [140, 96]. Stray electric field compensation is necessary because Rydberg states have a huge electric polarisability and we will null stray electric fields to minimise the influence of the DC-Stark effect [145]. The electrode structure comprises two quarter-split ring electrodes placed symmetrically above and below the centre of the vacuum chamber[9], as well as two microchannel plates[10] for ion detection. Additionally we placed a high numerical aperture lens[11] inside the chamber to allow for high resolution imaging in e.g. a quantum gas microscope [148, 149]. High resolution imaging and field ionisation capability were not employed before completion of this thesis, though. Furthermore, a coil was wound around the in-vacuum lens holder to serve as a radio frequency antenna.

2.2.2 Versatile laser source for D1 and D2 light

Many stages of our experiment require strong laser light on the finestructure transitions to the first excited state of ^{39}K , which are called D1 transition ($|4s_{1/2}\rangle \rightarrow |4p_{1/2}\rangle$, 770 nm)

[7] Corning HPFS 7980 KrF grade, mounted by VACOM into stainless steel viewports

[8] The viewports are manufactured by UKAEA out of Heraeus Suprasil 3001. They were anti-reflection coated for 460 nm (two-photon excitation to the Rydberg state in combination with 767 nm light), 575 nm (optional two-photon single-wavelength excitation, not used in this thesis), 767 nm (MOT and imaging light), 1064 nm (high-power dipole traps).

[9] Designed and manufactured in-house [147, 140].

[10] Hamamatsu F1551-21S

[11] Asphericon A45-32 HPX. Aspheric lens with numerical aperture 0.61 and 32 mm focal length. The planar side faces the atomic cloud and was coated with an anti-reflection coating for 767 nm combined with an an indium thin oxide (ITO) coating as the last layer (Evaporated Coating Inc. #939). This increases the electric conductivity to prevent the build-up of space charges on the glass surface as Rydberg atoms are sensitive to electric fields. The convex side was only anti-reflection coated (Evaporated Coating Inc. #6408) alone. The transmission of the ITO is specified as 98 %. In combination with an external lens, the combined optical array has a 47 fold design magnification.

and D2 transition ($|4s_{1/2}\rangle \rightarrow |4p_{3/2}\rangle$, 767 nm). An overview of the required transitions is given in Figure 2.2. Uses are the 2D-MOT, the 3D-MOT and the gray molasses, imaging of the atom cloud and also one leg of the two-photon Rydberg excitation in combination with 457 nm light. Furthermore, we need to be able to address individual hyperfine state transitions, which have different transition energies of up to several hundred MHz.

Figure 2.3 shows the laser system used to meet all the outlined tasks. The D1 and D2 laser light is created by two separate diode lasers[12], which are frequency stabilised by Doppler-free modulation-transfer spectroscopy to a linewidth of 150 kHz [142]. To enhance the stability of the D2 laser light further for the second set of experiments discussed in chapter 6, the spectroscopic reference was replaced by an ultrastable cavity (section 2.3). Four home-built tapered amplifiers[13] [150] are used to amplify the light from ≈ 30 mW to a total of ≈ 3 W, where the output can be switched between D1 and D2 light. Switching between the two sources is enabled by an electro-optic modulator (EOM), which rotates the polarisation of the overlapped D1 and D2 light, and a subsequent polarisation selecting beamsplitter cube. Specific hyperfine transitions are reached by splitting the output into several branches with dedicated frequencies set, and individually tunable, by acousto-optic modulators (AOM) [142, 141]. This way both hyperfine ground states can be addressed optically on both the D1 and D2 transition. Furthermore, by switching the diffraction order of the double pass AOMs of all three output branches in Figure 2.3 simultaneously, we can switch the trapped isotope between ^{39}K and ^{40}K [141]. We were able to demonstrate this in our experiment, but the very low abundance of ^{40}K in our atom source precluded any efficient preparation of sufficiently large ultracold clouds.

2.2.3 Source of pre-cooled atoms

Our atom trap at the centre of the science chamber is loaded from a 2D-MOT, which provides a directed beam of pre-cooled potassium atoms. The design was adapted from [147]. Magneto-optical traps provide cooling through the scattering force of near-resonant laser light [151]. Photons are absorbed from the directed laser beam and spontaneously reemitted in random direction yielding a directed momentum transfer on average. In combination with a quadrupole magnetic field and counter-propagating laser beams of orthogonal circular polarisation, confinement is also achieved. [152]

Our 2D-MOT is based on a glass cell connected to the science chamber by a small differential pumping hole. Inside the glass cell a hot vapour of potassium atoms is supplied by dispensers[14] with a natural isotope abundance[15]. Since the transition frequencies utilized in a MOT the trapping and cooling is isotope specific. We select potassium-39 in our apparatus, since it has the highest abundance. To address population in both hyperfine ground states of potassium-39, we use a two-wavelength scheme with a cooler on the $|4s_{1/2}, F = 2\rangle \rightarrow |4p_{3/2}, F' = 3\rangle$ transition, which is a closed transition, and an additional repumper on the $|4s_{1/2}, F = 1\rangle \rightarrow |4p_{3/2}, F' = 2\rangle$ transition (cf. Fig. 2.2). Repumper and cooler light is transmitted by optical fibres first to a distribution board [143], where both beams are first overlapped and mixed and subsequently split equally to yield light for

[12] Toptica: Tunable diode laser DL Pro

[13] Based on TA chips from Eagleyard (EYP-TPA-0780-01000-3006-CMT03-0000)

[14] Alvatec AS-3-K-100-F with natural abundance distribution. Procured dispensers with enriched ^{40}K AS-3-K40(14%)-10-F were empty.

[15] The natural isotope abundances of potassium are: ^{39}K 93%, ^{40}K 0.01%, ^{41}K 7%

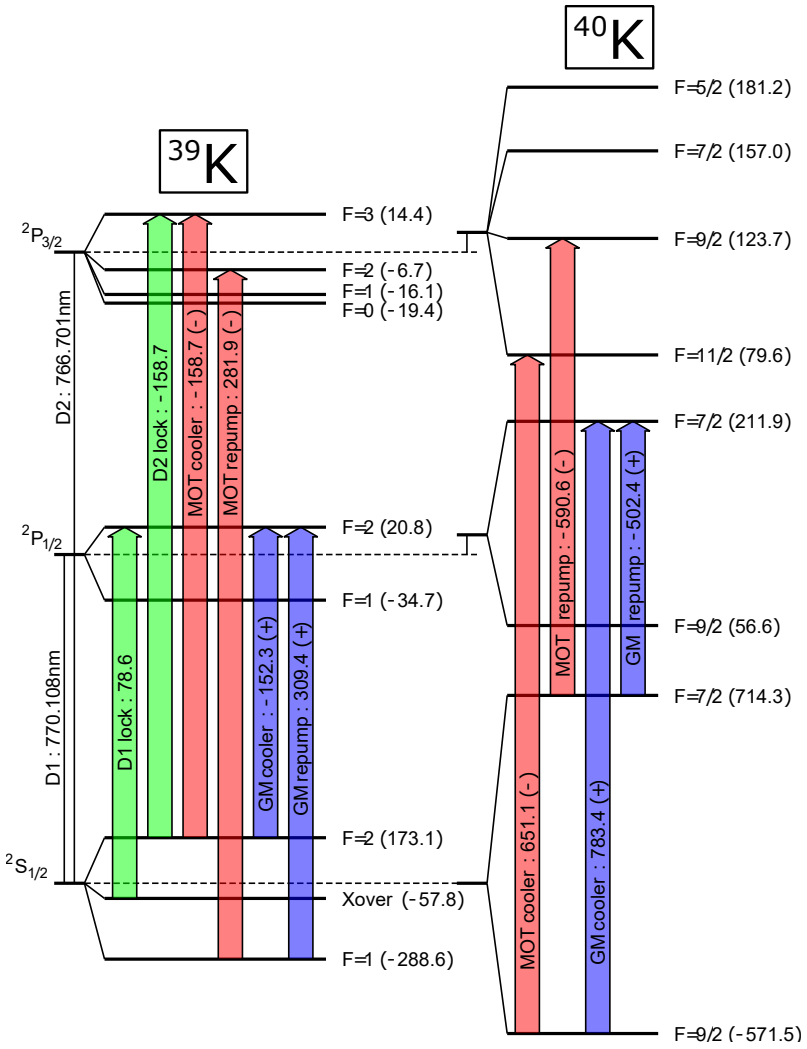

Figure 2.2: Diagram of the energy levels of ^{39}K and ^{40}K in comparison. Frequencies are given in MHz relative to the finestructure resonances of ^{39}K indicated by dashed lines. The position of the hyperfine levels are not drawn to scale. The spectroscopy transitions used for locking of the lasers are indicated in green, the MOT transitions in red and the gray molasses (GM) in blue. There, (+) and (-) indicate required blue and red laser detuning depending on the type of trap. Reproduced from [141].

both transverse cooling axes of the 2D-MOT. The light is transmitted to the 2D-MOT cooling modules via fibres. Because of the small hyperfine splitting of the excited state[16], a repumper of comparable power to the cooler is required. The magnetic quadrupole field and cooling light are provided along the transverse direction to the long axis of the glass cell. An additional red detuned pusher beam yields a pushing force along the long axis of the glass cell and into the science chamber to enhance the atom flux. Our 2D-MOT provides a strong flux of potassium atoms of up to $2 \cdot 10^9$ atoms/s (for a low dispenser current of 1.9 A) filling the 3D-MOT with $3 \cdot 10^9$ atoms to saturation within 1 s.

[16] 21.1 MHz between $F' = 2$ and $F' = 3$, which is 3.5 times the natural decay rate of the $|4p_{3/2}\rangle$ state

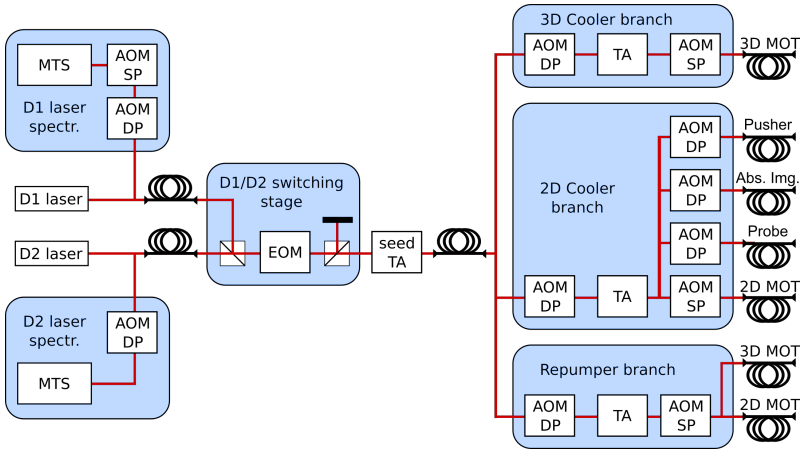

Figure 2.3: Schematic of the combined D1 and D2 laser system with spectroscopic frequency stabilisation, power amplification by tapered amplifiers (TA), frequency shifting by acousto-optic modulators (AOM) and transmission to the core apparatus by optical fibres. An electro-optic modulator (EOM) is used to switch between D1 and D2 light and to overlap the two by applying a phase shift. Double-pass AOMs (DP) are passed twice and are used to tune the frequency around an offset frequency. The frequency offset can be further enlarged or compensated by a single-pass AOM (SP), which is not used to tune the frequency of the light, but its power by changing the power in the used diffracted order of the AOM. Reproduced from [141].

2.2.4 3D-MOT

The 3D-MOT is based on the same operation principle as its 2D-MOT prestage (for details see [144, 143]), but cools and traps in all three spatial dimensions by applying three pairs of counter-propagating laser beams with superimposed cooler and repumper light. We use large diameter (1") MOT beams to create a large trapping volume. Each MOT beam carries a maximum of about 10 mW cooler and 3 mW repumper light. The quadrupole field is provided by two water-cooled coils outside the vacuum chamber. Also our 3D-MOT is fibre coupled to improve beam pointing stability. After loading for 1 s, we compress the MOT by maximising the magnetic field gradient and ramping the laser detunings accordingly to compensate the changing Zeeman shift. In this way we achieve a smaller volume of the trap to improve overlap with the dipole trap. In our setup, efficient cooling of potassium-39 in a 3D-MOT stops at 2 mK because of the narrow spacing of the excited state hyperfine structure, such that traditional sub-Doppler cooling mechanisms [152, 153] in the MOT are prevented.

2.2.5 Dipole trap

In order to confine and suspend ultracold atoms without driving electron transitions and to control the temperature and density of the cloud, we use all-optical dipole traps [152, 154]. In this scheme, a conservative trapping potential is solely realised by a high power laser beam which is far detuned from any electron transition. Thus the internal state of an atom is preserved by the trap and the trapping effect does not require any specific spin configuration. Another advantage of dipole traps is that they are created by external laser beams and optics solely and thus are rapidly switchable and can be easily adapted, moved or shaped for new experiments.

Optical dipole traps generate a gradient force on the atoms, in contrast to the scattering force employed by the previous MOT cooling stages. In the limit where the detuning of the coherent laser light interacting with an atom transition is much larger than the driving strength, the effect of the laser is not to drive a transition, but to modify the energies of the electronic states. This potential energy is proportional to the laser intensity and its spatial profile. Therefore a trapping potential can be generated this way by engineering an intensity profile with a global intensity optimum, which is trapping for red (negative) detunings and antitrapping otherwise [152].

In our experiments we employ a crossed dipole trap, see Figure 2.1(c), where the foci of two laser beams are overlapped to create a strongly confining trap in all spatial directions. The beams cross at an angle of approximately 10°. For the experiments presented in chapter 5 the second beam was derived by retroreflection from the first to double the trapping power, for the later experiments discussed in chapter 6 two independent beams were used. To avoid interference between the trap beams they have orthogonal linear polarisation. In both cases an elongated trap geometry is created, which is well suited for our Rydberg excitation experiments. The large opening angle makes it possible to guide the Rydberg excitation beams between the dipole trap arms such that the long axis of the atom cloud is almost collinear with the excitation beams. Furthermore we focus the trap beams tightly to a waist of approximately 30 µm [146], allowing for tightly focussed high intensity Rydberg excitation beams which are nearly uniform over the atom cloud volume. This is an important precondition for achieving strong driving to Rydberg excitations in the experiments of this thesis.

The dipole trap beams are derived from a single frequency laser at 1064 nm with 50 W maximum output power.[17] From this, about 10 W were split off for the trap, while the remainder was reserved for future lattice traps [155]. The power of the laser light is tuned and switched (on/off) by a high-power AOM[18] and guided by a photonic crystal fibre[19] to the designated vacuum viewport to ensure directional stability. The maximum combined trap power was 5.4 W, yielding an estimated maximum trapping depth of $\approx k_B \cdot 500\,\mu\text{K}$.

2.2.6 In-trap gray molasses cooling

To achieve efficient loading of the dipole trap one should strive for a large phase space overlap with the precursor trap. This ensures high atom densities as well as low temperatures. From the 3D-MOT we already derive a compressed cold sample, however it is not cold enough for efficient loading of our dipole trap. Therefore we additionally use gray-molasses cooling to achieve temperatures as low as 20 µK. This technique was established in [156, 157, 158] for potassium. It relies on blue-detuned light ($\Delta > 0$) coupling two hyperfine states with angular momentum $F \to F' \leq F$. Then there is at least one ground $|F, m_F\rangle$ state which is dark irrespective of the light polarisation, i.e. it is decoupled from the light field. For ^{39}K the D1 transition is used because the wider hyperfine splitting of the $|4p_{1/2}\rangle$ excited state allows for better state selectivity. Then a suitable transition presents itself for the cooler on the $F = 2 \to F' = 2$ transition, which is blue detuned to all other transitions as well (Fig. 2.4(a)). Since the alkali atoms have a second hyperfine ground state, the repumper is used analogously to the MOT scheme to couple the $F = 1$ ground state to

[17] Mephisto MOPA
[18] EQ photonics AOM 3080-1990
[19] Large mode area photonic crystal fibre LMA-PM-15 with a 14.8 micron core from NKT Photonics.

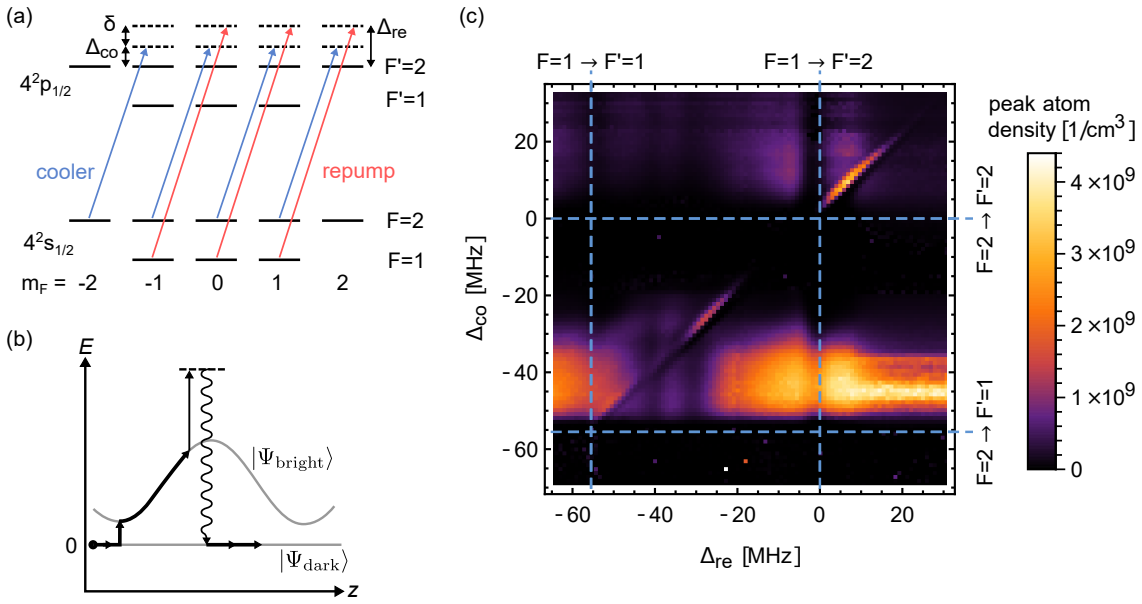

Figure 2.4: Gray molasses cooling of ^{39}K utilising the Λ-scheme. (a) Level scheme for cooling on the D1 line with σ^+ polarisation. $|F = 2, m_F = 2\rangle$ is decoupled and therefore a dark state. The cooler and repumper are blue (positive) detuned by Δ_{co} and Δ_{re}, respectively. Close to Raman detuning $\delta = \Delta_{\mathrm{re}} - \Delta_{\mathrm{co}} = 0$ this Λ-scheme has additional coherent dark states. (b) Illustration of the cooling mechanism for an atom moving in positive z direction and initially in the dark state. If a bright state is energetically close the coupling probability into the bright state is highest. From there the atom climbs the potential energy hill provided by the polarisation gradient of the cooling light. Spontaneous decay results in an average kinetic energy loss. (c) Measurement of the gray molasses cooling efficiency. The observable is the peak optical density of the atom cloud after 6 ms time of flight. Then a higher density corresponds to a lower temperature. Dashed lines indicate resonant transitions. The diagonal features correspond to the resonance condition $\delta = 0$, for which cooling is most efficient. Reproduced from [155, 156].

$F' = 2$ also. This has the additional benefit that cooler and repumper form a coherently coupled three-level system in Λ-configuration. If the two-photon Raman detuning δ is zero, this leads to extra coherent dark states which enhance the population trapping.

In contrast to the dark states, all bright states within the ground state manifold have an optical admixture of excited states, which shifts bright states above dark states for a blue laser detuning. Therefore only bright states are influenced by polarisation gradients formed by the interfering laser cooling beams, see Figure 2.4(b). An atom moving relative to the light field may couple between dark and bright states by motional coupling or dipole coupling via off-resonantly excited hyperfine states [156]. This happens preferentially when dark and bright states are closely spaced, i.e. at a potential energy valley of the bright state. Once the atom has transitioned into a bright state, motion transforms kinetic energy into potential energy much like in Sisyphus cooling [153]. Eventually the bright state will decay to a lower energy state and thus on average dissipate potential energy until eventually arriving back at the dark state.

In our experiment we reuse the optics of the 3D MOT and inject repumper and cooler branches with D1 light.[20] The configuration with three pairs of counter propagating beams

[20] For details see [141]

in $\sigma^+\sigma^-$ configuration used for the 3D-MOT is suitable for providing gray molasses cooling in all spatial directions and at the same time allows for a compact and cost-efficient setup while maintaining full independent control over all beam powers and detunings.

Figure 2.4(c) shows a detailed scan of the cooler and repumper detunings revealing optimal cooling conditions. Here gray molasses cooling was applied for 5 ms in free space prior to holding the atoms for 200 ms in the optical dipole trap. We release the atom cloud from the trap and measure the peak optical density after 6 ms free expansion. The cloud expansion is proportional to the cloud temperature, such that the peak optical density serves as a cooling performance parameter. Cooling is dominated by the cooler light leading to prominent horizontal stripes of cooling (bright) and no cooling or heating (dark). We attribute this to the dominant cooler power, which was two to four times stronger than the repumper light. The crossover between the horizontal cooling and heating bands is marked by a resonant transition matching the specified laser detunings (blue dashed lines). In addition, resonant heating by the repumper causes the vertical dark stripes in the spectrum.[21] The widths of the resonance features are in agreement with the D1 linewidth of 5.96 MHz [159]. Thus we conclude that the observed cooling corresponds to a blue detuned transition and thus gray molasses, while no cooling was observed for red detunings. Cooling works best for positive detunings of two to four linewidths for both repumper and cooler. In addition to the horizontal and vertical features, we also detect two thin diagonal stripes originating from the Λ-enhancement at resonant Raman detuning. Best gray molasses cooling was achieved with Λ-enhancement if both repumper and cooler were tuned above $F' = 2$ and this configuration was utilized for optimising the loading of the optical dipole trap.

2.2.7 Absorption imaging of the ultracold atom cloud

After Rydberg excitation, the atom cloud is measured by absorption imaging, which allows one to estimate the size, atom number and density of the cloud. The optical array used for absorption imaging is placed outside the vacuum system (Fig. 2.1) and is based on a 4f-configuration (numerical aperture 0.2, onefold magnification) and a standard near-infrared camera[22].

In total, each cycle requires approximately 1.5 s to create a ready-to-use ultracold atom cloud of ca. 100 000 atoms. We achieve densities, measured by absorption imaging, up to $5 \cdot 10^{11}\,\mathrm{cm}^{-3}$, which we can freely reduce to as low as $4 \cdot 10^{9}\,\mathrm{cm}^{-3}$ by adapting the 3D-MOT loading time. This way the atom density is independent of the dipole trap potential. The atomic cloud has $e^{-1/2}$ radii with typical values $\{\sigma_r, \sigma_z\} \approx \{10\,\mu\mathrm{m}, 200\,\mu\mathrm{m}\}$. Typical temperatures range between 20 µK and 40 µK. For these conditions, the measured lifetime of the trapped cloud is approximately 3 s.

2.3 Laser sources for one and two-photon Rydberg excitation

Within this thesis, both two photon (chapter 5) and single photon (chapter 6) excitation have been used to drive transitions to Rydberg states. A schematic of all laser sources is given in Figure 2.5. In single photon excitation $|np\rangle$ states can be addressed, while

[21] Additional vertical lines at $\Delta_{\mathrm{re}} = -31$ MHz and -40.5 MHz correspond to D2 repumper light at the $F = 2 \to F' = 2$ and $F = 2 \to F' = 1$ transitions leaking into the D1 gray molasses.

[22] IDS UI-3240ML-NIR-GL

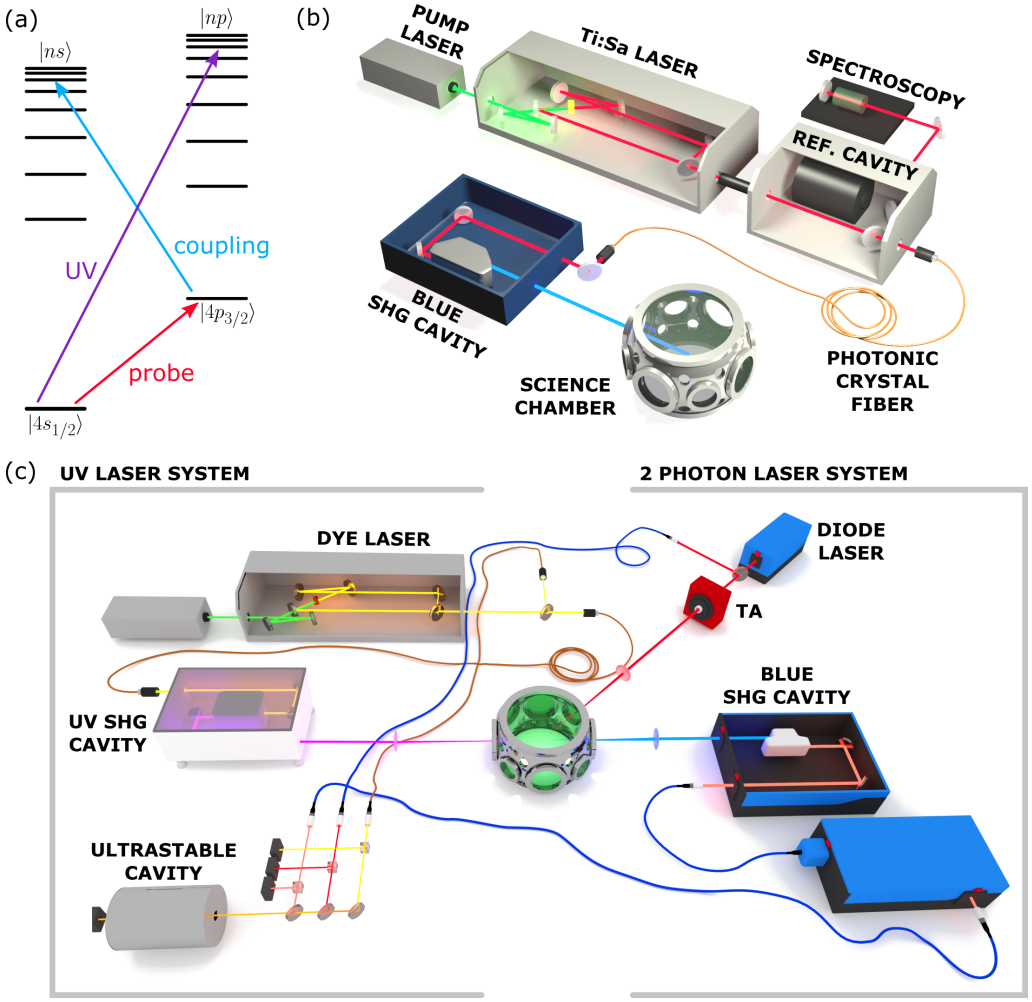

Figure 2.5: Laser sources for Rydberg excitation. (a) Direct one photon excitation (288 nm) from the ground state to a $|np\rangle$ state, or two photon excitation to $|ns\rangle$ states via the intermediate $|4p_{3/2}\rangle$ state can be used. For two-photon excitation a probe beam (767 nm, cf. Fig 2.3) is combined with a coupling beam (457 nm). (b) Laser setup for creating the coupling light, consisting of a Titanium-Sapphire (Ti:Sa) laser and a second harmonic generation (SHG) cavity. The Ti:Sa is stabilised to a reference cavity, which itself is stabilised to a ^{39}K Doppler-free spectroscopy reference. (c) Schematic of the final stage of the Rydberg excitation setup comprising both single photon and two photon excitation lasers. The UV light is derived via second harmonic generation from a dye laser (576 nm), the blue light originates from a second SHG setup seeded with a tapered amplifier (TA) laser (913 nm), and the red light is taken from the TA setup used to drive the magneto optical traps. All three lasers are stabilised to the ultrastable cavity. Reproduced from [145, 160].

two-photon excitation couples to $|nd\rangle$ and $|ns\rangle$ states. The (non-interacting) $|ns\rangle$ states have an isotropic wavefunction and therefore isotropic van der Waals interactions [96]. The small transition dipole moments between Rydberg and low lying states necessitate high power and tightly focused laser sources to achieve large Rabi frequencies (cf. section 3.2.2). Additionally a major consideration was to minimise decoherence from laser phase noise. Therefore our efforts focused on both the laser sources as well as the laser frequency stabilisation.

Focusing on laser sources, two-photon excitation allows for several choices depending on the addressed intermediate state. In the following, we will refer to the light driving transitions between ground $|g\rangle$ and intermediate $|e\rangle$ states as probe light and to the one coupling intermediate and Rydberg $|r\rangle$ states as coupling light. Typically the first excited state is used as the intermediate state (here $|4p_{3/2}\rangle$), such that laser light from magento-optical trapping is readily available as probe light (cf. Fig. 2.3). But also an alternative route via the second excited state ($|5p_{3/2}\rangle$ correspondingly), the so-called "inverted" excitation scheme, is within the range of standard lasers [96, 123, 161]. This poses an interesting alternative since then high-power infrared diode lasers become available for the coupling light. A third alternative is single-colour two-photon excitation, which is very far detuned from any intermediate state [162]. We opted for the most common technique of coupling to the first excited state with $|e\rangle = |4p_{3/2}\rangle$, since the probe laser is readily available then, requiring a coupling laser in the blue wavelength regime.

One common approach to creating high-power laser light for the coupling beam is to use frequency-doubled semiconductor laser systems with typical output powers $\lesssim 1\,\mathrm{W}$ and stabilised laser linewidths $\leq 200\,\mathrm{kHz}$. For the experiments reported in this thesis using two-photon excitation schemes we explored an alternative, which was reported in [160]. It consists of a Titanium-Sapphire laser[23] (wavelength $\sim 922\,\mathrm{nm}$) stabilised to a reference cavity and frequency-doubled[24] to the blue spectral region (Fig. 2.5(b)). The Titanium-Sapphire laser delivered 5 W in day-to-day operation, which was transmitted to the frequency-doubling cavity by a single-mode polarisation maintaining fibre[25] with 50% coupling efficiency. With this setup we achieved output powers of blue light of up to 1.5 W. To frequency stabilise this laser system the reference cavity length of the Titanium-Sapphire laser was itself stabilised to a 767 nm wavelength atomic reference via Doppler-free modulation transfer spectroscopy of a ^{39}K thermal vapour [160, 163][26]. Hereby the atomic reference light can be frequency shifted within the free spectral range of the reference cavity to tune the corresponding frequency of the blue laser light. We used a double pass AOM[27] with a centre frequency of 800 MHz and a direct digital synthesizer (DDS)[28] as a frequency source to perform this task. The reference cavity is locked to the reference light using the Pound-Drever-Hall technique [164, 165], with the required sidebands generated by an EOM. The blue laser linewidth of the thus stabilised system was measured to be 120(20) kHz.[29] One additional benefit of the frequency doubled Titanium-Sapphire laser system is the large wavelength tuning range spanning output wavelengths from 455 nm to 463 nm, which allows one to excite to Rydberg states of potassium with principal quantum numbers ranging from $n = 18$ to above the ionisation threshold, as was shown in [160].

Turning to single-photon excitation (Fig. 2.5(c)), the transition wavelengths typically lie in the ultraviolet, for which high-power lasers are more difficult to create. For potassium, transition wavelengths of $\sim 288\,\mathrm{nm}$ need to be implemented. At this wavelength, light is also prone to damage optical elements (e.g. the vacuum viewports, cf. sec. 2.2) and biological tissue. To achieve single-photon operation, we implemented a dye laser (wavelength

[23] The Titanium-Sapphire laser is a continuous wave ring-laser (Sirah Lasertechnik Matisse TX). It was pumped by a solid state laser (Spectra-Physics Millenia eV) with an output up to 22 W.
[24] Toptica SHG-pro
[25] NKT-photonics LMA-PM-15
[26] The same spectroscopic technique was used to frequency stabilise the MOT laser system, cf. section 2.2.2.
[27] Brimrose TEF-600-400
[28] Analog Devices AD9914
[29] Measured with an optical cavity. Sirah Lasertechnik, EagleEye.

$\sim 576\,\mathrm{nm}$) stabilised to an ultrastable reference cavity and frequency doubled to the UV. The dye laser was set up by exchanging the gain medium and optical elements of our Titanium-Sapphire laser[30], and the doubling cavity was swapped accordingly[31]. For this setup we achieved day-to-day powers of 3 W output of the dye laser, which was transmitted by the same photonic crystal fibre as in the precursor setup (coupling efficiency 50%) to the doubling cavity. The maximal UV output power was 80 mW. To stabilise the dye laser an ultrastable, high-finesse cavity[32] was used without an intermediate reference cavity. With this stabilisation scheme the achieved UV laser linewidth was 360 kHz [145]. As an absolute frequency reference we employed a high-finesse wavemeter[33]. The ouput light is freely tunable via a fibre-coupled EOM[34] which provides both the carrier frequency (100 - 600 MHz) to freely tune the UV laser frequency across a free spectral range of the cavity, and the sideband (20 MHz) for the laser lock. Here we opted for a fibre-coupled EOM, since it is much easier to implement than the large-tuning range AOM used beforehand. In parallel, a new seed laser[35] for the blue frequency doubling cavity was installed, but not used in this thesis.

Comparing the two different schemes and setups for laser excitation used in this thesis, single-photon excitation outperformed two-photon excitation achieving larger effective coupling Rabi frequencies from ground to Rydberg state at smaller effective loss rates. For UV excitation we were able to generate Rabi frequencies up to 200 kHz for effective Rydberg decay rates of approximately 10 kHz, including photoionisation. In contrast to Rydberg $|ns\rangle$ states, $|np\rangle$ states have a much higher ionisation cross section [166, 167]. For two-photon excitation we achieved effective Rabi frequencies up to 100 kHz and effective decay rates of 100 kHz including decay of the far-detuned intermediate state. However, the achieved dephasing noise in both excitation schemes remains large with $\gamma_{\mathrm{de}}/2\pi = 360\,\mathrm{kHz}$ for the UV laser and an estimated combined dephasing rate of 300 kHz for two-photon excitation. These strong dephasing rates limit the timescale on which phase coherent evolution can be observed, leading to dephased, effective classical behaviour on the ms timescales investigated in the experiments presented in this thesis.

Conclusion

To summarize, we have established an experimental apparatus based on ultracold ^{39}K atoms laser-coupled to Rydberg states and tailored towards studying the driven-dissipative evolution of the many-body system. This platform is characterised by wide-range control over driving, interaction and dissipation properties of the system, making it well suited to explore vastly different regimes of non-equilibrium behaviour corresponding to different system parameters. Control over laser driving encompasses strength, detuning and the addressed Rydberg state. Employing both single and two-photon excitation schemes Rydberg $|ns\rangle$, $|np\rangle$ and $|nd\rangle$ states can be addressed, extending our control to the strength and anisotropy of the interactions as well as the spontaneous lifetime of the Rydberg state.

[30] Sirah Lasertechnik provides optics sets for the required wavelength range (MOS-4) as well as the dye pump and dye injection nozzle.
[31] Sirah Lasertechnik Wavetrain II
[32] Stable Laser Systems ATF 6010-4
[33] HighFinesse WS7
[34] Jenoptik PM594
[35] Combined diode laser tapered amplifier system, Toptica TA-pro

Additionally, we achieve high densities and ultracold temperatures of the atom clouds by utilizing a 2D-MOT as an atom source and gray molasses cooling. The atom density can be tuned via the 3D-MOT loading time independent of the dipole trap potential, allowing for independent interaction strength control. Our laser systems are characterised by low phase noise resulting in low decoherence rates of quantum states, which we achieved by referencing the lasers to Doppler-free spectroscopy or an ultrastable cavity. This set of capabilities enabled the experimental studies reported in this thesis. Future experiments can also draw on an available fermionic atom species (^{40}K) to realise novel quantum states of matter [168, 104, 106, 169, 170], as well as additional detection schemes via high-resolution fluorescence imaging [148, 149] and Rydberg excitation counting [117, 116, 121]. The combination of these characteristics make this platform, and ultracold Rydberg atoms in general, a platform ideally suited for studying quantum systems close to or far away from equilibrium.

From atomic physics to interacting driven-dissipative spin systems

3

In this thesis, a platform of ultracold atoms is engineered into an analogue of open quantum spin systems. In our approach, Rydberg states, i.e. highly excited atomic states, are the means to induce and control strong and long-range interactions between spins. External driving of the spin system by the laser fields coupling atomic ground to Rydberg states, and dissipation via the finite Rydberg state lifetime complete the core characteristics of the microscopic details of our model system. In the previous chapter we discussed how our ultracold atom platform is implemented in the laboratory and how the parameters governing the microscopic processes can be controlled and manipulated by the experimentalist. In our setup, special care was taken to achieve good thermal isolation from the environment, such that the only coupling to the environment occurs via electromagnetic radiation in the form of laser fields, and additionally vacuum fluctuations and thermal blackbody radiation leading to dissipation. In particular, the excitation lasers address specific target Rydberg states, isolating an effective two-level system within the manifold of electronic states of an atom. Building on this basis, we will be able to formulate a microscopic description of our system, and map it to an open quantum spin system. Figure 3.1 illustrates this mapping from the electronic level structure of an atom to the synthetic Rydberg spin system with interactions, external driving and dissipation.

At the beginning of this chapter, the fundamental framework for describing open quantum spin systems will be introduced, where the state of the system is captured by a density matrix evolving according to a quantum master equation. Thereafter, we will turn to the properties of Rydberg states and the microscopic properties which derive from these. In section 3.2 the mapping to the spin system is introduced and the characteristic microscopic properties discussed. This will be followed in section 3.3 by a discussion of central many-body properties of Rydberg spin systems, which emerge from the interplay between interactions, driving and dissipation. In the final part of this chapter we will use the gathered knowledge on Rydberg spin systems to formulate approximate models. These will be vital in establishing quantitative links between our experimental observations of macroscopic properties of our system and the foundational microscopic details.

3.1 The quantum master equation framework

The density-matrix formalism is well suited to describe the evolution of open many-body quantum systems, where the environment couples to the system under consideration. The effect of the environment is to introduce stochastic transitions, leading to dissipation of energy and a dampening of phase coherence between states of the system. This requires a

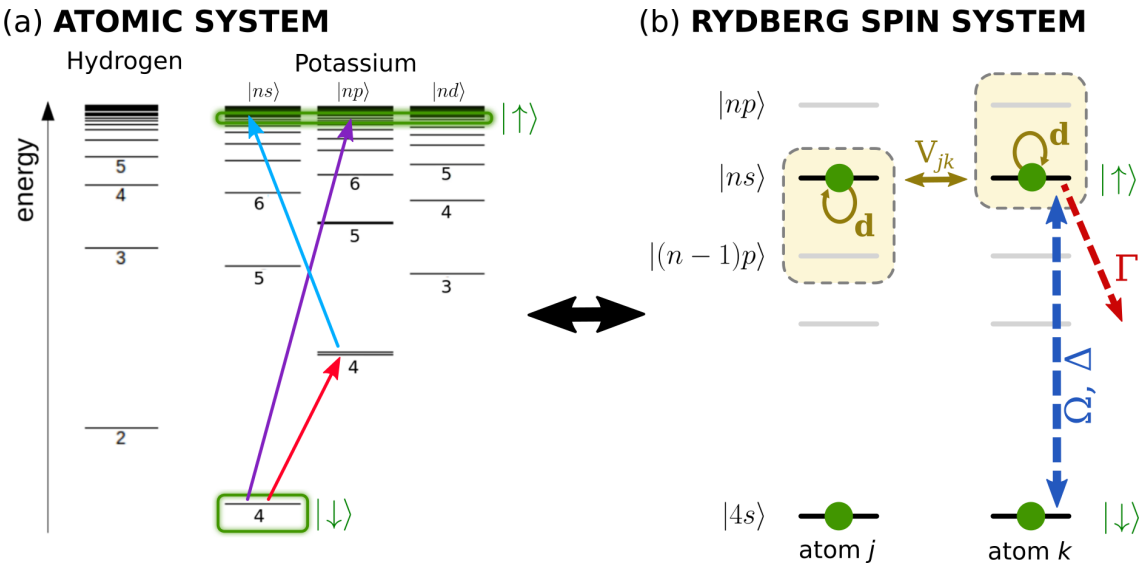

Figure 3.1: Mapping of the electronic level structure of an atom to an effective quantum spin system. (a) The manifold of electronic states of a potassium atom compared to hydrogen. In hydrogen, the angular momentum l states are degenerate, while they become energetically separated for alkali atoms like potassium. The ground state of potassium is the $|4s\rangle$ state, which we encode as a $|\downarrow\rangle$ state. We selectively address a Rydberg $|nl\rangle$ state with a laser light field, which serves as the $|\uparrow\rangle$ state. (b) Reduced spin system for the case of two-photon coupling from $|\downarrow\rangle = |4s\rangle$ to $|\uparrow\rangle = |ns\rangle$, comprising the effective laser driving field with detuning Δ and strength Ω, effective decay rate Γ and Rydberg-Rydberg van der Waals interaction V_{jk} between a pair of atoms j, k. The interactions originate from perturbative couplings to neighbouring Rydberg states, which are dominated by induced transition dipoles $\mathbf{d}$.

statistical description of observables in terms of ensemble averages, where the expectation value of an observable with operator A is given by

$$\langle A \rangle = \mathrm{Tr}[A\hat{\rho}]. \tag{3.1}$$

In general, the density matrix operator $\hat{\rho}$ gives the probability distribution of microstates on the diagonal, while off-diagonal terms give the corresponding coherences between microstates. In the limit where the coherences can be neglected, the density matrix describes an effectively classical system.

In principle, the evolution of a system including its environment and the couplings between both can be described by an extended Hamiltonian. The temporal evolution of such an extended system with density matrix $\hat{\rho}_{\mathrm{tot}}$ is governed by the von Neumann equation,

$$\partial_t \hat{\rho}_{\mathrm{tot}} = -\frac{i}{\hbar}[\mathcal{H}, \hat{\rho}_{\mathrm{tot}}], \tag{3.2}$$

which is the density-matrix equivalent of the Schrödinger equation. However, the state space of the environment typically is intractably large and the state of the environment is not observed. The equation of motion of the density matrix of the (open) system itself can then be obtained by the partial trace over all states of the environment $\partial_t \hat{\rho} = \mathrm{Tr}_{\mathrm{env}}[\partial_t \hat{\rho}_{\mathrm{tot}}]$. Under the Born-Markov approximations, which assume that system and environment

remain approximately separable for all times, and that phase correlations within the environment decay instantly, the quantum master equation can be written in Lindblad form. [171]

$$\partial_t \hat{\rho} = -\frac{i}{\hbar}[\mathcal{H}, \hat{\rho}] + \mathcal{L}(\hat{\rho}) \tag{3.3}$$

In this equation the Hamilton operator $\mathcal{H}$ governs the unitary part of the evolution, in our case interactions and coherent driving. The Lindblad superoperator $\mathcal{L}$ describes dissipative, non-unitary processes acting on $\hat{\rho}$, which we use to model decay and irreversible dephasing. The Born-Markov approximations are valid for example if the system-environment coupling is weak and the state space of the environment is much larger than the one of the system itself. These conditions also apply to environment couplings via vacuum fluctuations and thermal blackbody radiation, which lead to dissipation in our system. Additionally we also describe dephasing from laser phase noise by a Lindblad superoperator, where we assume that the amplitude of the phase fluctuations are small. The Lindblad superoperator has the general form

$$\mathcal{L}(\hat{\rho}) = \hbar \sum_{\{L_j\}} \left[L_j \hat{\rho} L_j^\dagger - \frac{L_j^\dagger L \hat{\rho} + \hat{\rho} L_j^\dagger L_j}{2} \right]. \tag{3.4}$$

In this equation the effect of the stochastic coupling to the environment is captured by a set of jump operators $\{L_j\}$, which describe the dampening of coherences and dissipation of energy. For our system, the L_j will be local operators acting on individual atoms. The local density matrix of a single atom j can be obtained by tracing over all other atoms $\hat{\rho}^{(j)} = \mathrm{Tr}_{k \neq j} \hat{\rho}$.

In the next section we will discuss how our experimental platform of ultracold atoms laser-excited to Rydberg states can be reduced to a spin system. Furthermore, we will show how laser driving, dissipation and induced interactions, which govern the evolution of the system, can be cast as Hamilton or Lindblad operators acting at the microscopic level on the density matrix $\hat{\rho}$.

3.2 Microscopic processes of ultracold atoms excited to Rydberg states

The coherent laser fields used for excitation effectively isolate a two-level system within the electronic state space of an atom (Fig. 3.1(a)), such that it may be identified as a pseudo-spin 1/2 system. The evolution of the resulting Rydberg spin system (Fig. 3.1(b)) is governed by interactions V_{jk} between two atoms j, k excited to Rydberg states, driven with strength Ω and detuning Δ, and dissipation with decay rate Γ. In the case of two-photon excitation the addressed intermediate state will be populated in addition to the ground and Rydberg states. The effect of the intermediate state population on the interaction and dissipation properties of the spin system, as well as laser driving scenarios where this population is minimal will be discussed in the next chapter and in the context of the experiments employing two-photon excitation in section 5.2. There we will also introduce appropriate expressions for the effective driving strength Ω, the two-photon detuning, and the effective decay rate of two-photon Rydberg excitation incorporating the finite lifetime of both excited states.

In our system, driven-dissipative dynamics of the internal spin-1/2 state space is additionally supplemented by pure particle dissipation to shelving states external to the coupled spin-1/2 system. Thus, our system is subject to dissipation of energy and loss of particles and intrinsically open. All the characteristic properties of this system depend on the properties of the addressed Rydberg state, especially its dipole moments for transitions to other electronic states. Therefore, we will begin our discussion with a summary of the relevant properties of Rydberg states. Subsequently, we will show how the relevant processes can be cast as Hamilton or Lindblad operators acting at the microscopic level on the many-body density matrix $\hat{\rho}$. Our goal is to establish the quantum master equation specific to our system, which describes the evolution and behaviour of its microstates. In the following descriptions, we will use the reduced internal spin-1/2 state space and treat the particle loss as a coupling to an external reservoir. [1]

3.2.1 Properties of Rydberg states

Rydberg states, i.e. highly excited states, are in many ways extreme electronic states of atoms, with very different properties compared to low-energy states. While the radial size of a ^{39}K atom in its electronic ground state is $4.7\,a_0$, the spatial extent of a Rydberg state wavefunction easily becomes as large as 100 nm for typical Rydberg states with principal quantum number $n \sim 40$, as used in this work. An electron in such a highly excited state is only loosely bound to the atom core such that the electron wavefunction overlap with the core as well as with low energy states is very small. Therefore Rydberg states can be viewed as hydrogen-like irrespective of the atomic species and the structure of the core. The properties of Rydberg states can thus be described by a modified principal quantum number $n^* = n - \delta_{n,l,j}$ for n the principal quantum number of the specific Rydberg state and $\delta_{n,l,j}$ the quantum defect for the state $|n, l, j\rangle$ [172].[2] All properties of Rydberg states, including lifetime and interaction strength, scale with powers of n^* and have been documented extensively, for example in [172, 96] with values for ^{39}K presented in [145] and calculated using the ARC library [174].

The central aspects for our non-equilibrium many-body system are driving, dissipation and interactions of Rydberg states. Their respective strengths are all determined by transition dipole moments, either to neighbouring Rydberg states (interactions) or to low energy states (driving and dissipation by spontaneous decay). Compared to the transition dipole moment between the ground and first excited state ($2.90\,e a_0$ for $|4s_{1/2}\rangle$ - $|4p_{3/2}\rangle$ of ^{39}K), the transition dipole moment between neighbouring Rydberg states ($|\langle (n-1)p| er |ns\rangle| \propto (n^*)^2$) easily reaches or exceeds a three orders of magnitude larger amplitude for typical Rydberg states around $n = 40$, while the transition dipole moment between low lying states and Rydberg states (e.g. $|\langle 4s| er |np\rangle| \propto (n^*)^{-3/2}$) typically is three orders of magnitude smaller. This disparity is caused by the very large wave function overlap between Rydberg state wavefunctions on the one hand, or their very small overlap with low energy state wavefunctions on the other hand. As a consequence, Rydberg states have long lifetimes of $\sim 10\,\mu s$, much longer than the lifetime of low energy states,

[1] The reduction from the state space $\{|g\rangle, |e\rangle$, shelving state $|s\rangle\}$ to the internal spin-1/2 states can be achieved by the projection operator $P = |e\rangle\langle e| + |g\rangle\langle g|$ acting on the local density matrix $P\hat{\rho}^{(j)}P$. The thus reduced density matrix is no longer trace preserving.

[2] Quantum defects for potassium are reported in [173] using high precision spectroscopy. We were able to verify them in our own experiments [160]

which are complemented by highly exaggerated interaction properties as we will see in the following. However, the very weak dipolar coupling strengths to low-lying states poses significant challenges to create sufficiently powerful light sources for strong laser driving of the ground-to-Rydberg state transition.

In our experiments, the energy scales associated with the atom-light interactions, the interactions between Rydberg atoms, and dissipative processes can all be made comparable with one another. This provides the interesting scenario in which the quantum many-body dynamics are governed by a competition between driving, long-range interactions and dissipation. In the following we will summarise how these processes can be modelled, such that we can formulate the microscopic quantum master equation for the probability distribution of microstates of our many-body system. We will restrict our discussion here to single-photon excitation coupling ground and Rydberg states directly. Extensions of the developed descriptions to multilevel systems will be introduced in the next chapter.

3.2.2 External laser driving

In our experiments we use coherent laser light interfacing with atoms to drive transitions between specific atomic states. In this thesis we are concerned with strong laser fields, making a semi-classical description possible[171], where the light field is treated classically as an oscillating electric wave $\mathbf{E}(t, \mathbf{x}) = \mathbf{E_0} \cos(\omega t - \mathbf{kx})$ of field strength E_0 and angular frequency $\omega = c/|\mathbf{k}|$. The intensity of such a field is given by $I = \epsilon_0 c {E_0}^2/2$ with ϵ_0 the vacuum permittivity and c the vacuum speed of light. Under the condition that the light field is near-resonant to only a single atomic transition between two atomic states labelled ground state $|g\rangle$ and excited state $|e\rangle$, the atom can be reduced to a two-level system with energy splitting $\hbar\omega_{eg}$. Then the light field is detuned from the atomic transition by $\Delta = \omega - \omega_{eg}$.[3]

To describe the interaction of the light field with the atomic transition, we employ the dipole approximation[4], where the classical light field $\mathbf{E}$ couples to the transition's electric dipole operator $\mathbf{d_{eg}} = e\mathbf{r}$ via the interaction Hamiltonian $-\mathbf{d_{eg}} \cdot \mathbf{E}$. The validity of this approximation for Rydberg states has been shown in [175]. Transforming into a co-rotating frame and applying the rotating wave approximation for near-resonant driving ($\Delta \ll \omega + \omega_{eg}$) [171], the coupling between states $|g\rangle = \begin{pmatrix} 0 \\ 1 \end{pmatrix}$ and $|e\rangle = \begin{pmatrix} 1 \\ 0 \end{pmatrix}$ induced by the light field can be modelled by the atom-light Hamiltonian operator

$$\mathcal{H}_{\text{drive}} = \frac{\hbar}{2} \begin{pmatrix} -\Delta & \Omega \\ \Omega & \Delta \end{pmatrix}. \tag{3.5}$$

This Hamiltonian describes both coherent absorption and coherent stimulated emission, where at resonance the population of an initially unexcited atom oscillates with the Rabi

[3] For this definition of the detuning, so-called red detuning corresponds to $\Delta < 0$ and blue detuning $\Delta > 0$. This classification corresponds to the optical spectrum, where high energy light has blue colour and low energy light red colour correspondingly.

[4] The dipole approximation is valid in the limit $|\langle e|\,\mathrm{r}\,|g\rangle| \ll 1/|k|$, where the transition moment $\langle e|\,\mathrm{r}\,|g\rangle$ is limited by the wavefunction of smaller size. Then higher multipole components are much weaker than the electric dipole moment. This condition is fulfilled for (near) optical transitions between low-energy states of potassium, but also for the (near) optical transitions between these and highly excited Rydberg states considered in this thesis. Even though the extent of the Rydberg-state wavefunction is $\sim 100\,\mathrm{nm}$ and therefore similar to optical wavelengths, the overlap to low-energy states remains small, as is reflected in the small electric dipole matrix elements of these transitions.

frequency Ω in time. Since the Rabi frequency characterises the strength of the atom-light coupling, we will refer to it as the driving strength in this thesis. The two-level atom-light coupling description is valid, if the condition $\omega_{e\alpha} \gg |\Delta|,\ \Omega$ holds, where $\omega_{e\alpha}$ is the frequency difference between the targeted excited state $|e\rangle$ and any other state. In our experiments, this condition is fulfilled [96, 112].

The coupling is parameterised by the detuning Δ and the driving strength Ω, which is given by

$$\Omega = \frac{|\mathbf{d_{eg}} \cdot \mathbf{E_0}|}{\hbar}. \tag{3.6}$$

Here we see how the small transition dipole moments coupling ground and Rydberg states (cf. sec. 3.2.1) lead to very small driving strengths, requiring high power and tightly focussed laser sources to compensate. In the course of this thesis we were able to achieve driving strengths between ground and Rydberg states with a free tuning range from $\approx 2\,\mathrm{kHz}$ to as high as $\approx 200\,\mathrm{kHz}$, while the detuning can be freely tuned to $\sim 10\,\mathrm{MHz}$ above and below resonance. The large tuning range over orders of magnitudes of both driving parameters and the achieved large maximal driving strengths are a central capability in the experiments reported in this thesis.

3.2.3 Van der Waals interactions

The interaction between two alkali atoms (positions $\mathbf{r_j}$ and $\mathbf{r_k}$) with a separation $R = |\mathbf{R}| = |\mathbf{r_j} - \mathbf{r_k}|$ much larger than the size of the electronic wavefunction ($R \ll n^2 a_0$) is dominated by the electrostatic interaction energy of the two valence electrons $\mathcal{V}_{jk} = \frac{q_j q_k}{4\pi\epsilon_0 |\mathbf{R}|}$.[5] Then exchange interactions can be neglected and the interaction potential can be derived in multipolar expansion [177, 178]. The dominant dipole-dipole interaction energy is given by

$$\mathcal{V}_{jk} \approx \frac{1}{4\pi\epsilon_0}\left(\frac{\mathbf{d_j}\cdot\mathbf{d_k}}{R^3} - \frac{3(\mathbf{d_j}\cdot\mathbf{R})(\mathbf{d_k}\cdot\mathbf{R})}{R^5}\right), \tag{3.7}$$

with $\mathbf{d_j}$, $\mathbf{d_k}$ electric transition dipole operators. As is illustrated in Figure 3.1, this interaction operator acts as a perturbation on the energy of a pair of atoms in state $|\psi\psi\rangle$ via dipole mediated couplings to other nearby pairstates $|\alpha\beta\rangle$ [179] (for a review cf. to [172, 112, 96]). In this thesis, we will excite atoms only to one Rydberg state isolated by the laser driving and rely on the induced interactions between atom pairs $|\psi\psi\rangle$. The resulting interaction energy then is pairwise additive in a many-body system [97, 180]. To second order in perturbation theory the dipole-dipole interaction leads to a modification of the pair energy, which is given by

$$V_{jk} \approx \sum_{\alpha\beta} \frac{|\langle\psi\psi|\,\mathcal{V}_{jk}\,|\alpha\beta\rangle\,|^2}{E_{\psi\psi} - E_{\alpha\beta}} = \hbar\frac{C_6}{|\mathbf{r_j} - \mathbf{r_k}|^6}. \tag{3.8}$$

Typically the energy spacing of any two pair states $|E_{\psi\psi} - E_{\alpha\beta}|$ is much larger than the corresponding dipole-dipole coupling strength $|\langle\psi\psi|\,\mathcal{V}_{jk}\,|\alpha\beta\rangle\,|$, such that any admixture of

[5] The minimal distance at which the overlap may be neglected can be approximated by the Le Roy radius [176], which typically is $\sim 0.5\,\mu\mathrm{m}$. Below a separation of typically two to three times the Le Roy radius, non-perturbative contributions dominate due to pair state resonances, leading to a crossover to near-resonant dipole-dipole interactions [112].

$|\psi\psi\rangle$ with other pair states is negligible and that the interaction energy is well approximated by second order in perturbation theory. [127, 112] Additionally, the bandwidth of the excitation field, which is given by Ω for strong driving, is much smaller than the dipole-dipole coupling strength, such that only the $|\psi\psi\rangle$ pair state is populated by the light field. The effective Rydberg-Rydberg interaction potential scales with $1/R^6$ and is identified as van der Waals interaction between the induced transition dipoles. In the following, the separation R can be treated as a classical variable since the atomic motion is much slower than the internal electronic dynamics. In total, the condition $|E_{\psi\psi} - E_{\alpha\beta}| \gg |\langle\psi\psi|\,\mathcal{V}_{jk}\,|\alpha\beta\rangle| \gg \Omega$, for which the van der Waals interactions act as a perturbation to the Rydberg-Rydberg pair state energy and do not populate any other states significantly, holds in our experiments. Hence the two-level approximation of the atomic level structure is valid also under the influence of van der Walls interactions.

The effective interaction strength C_6 scales dramatically with principal quantum number, owing to the n^{*2} scaling of the dipole moment and the n^{*-3} scaling of the energy of adjacent pair states, in total resulting in $C_6 \propto n^{*11}$. According to our definition, $C_6 > 0$ corresponds to repulsive interactions, which is the case for the used Rydberg states of potassium with typical interaction coefficients being $C_6/2\pi \sim 10^3\,\mathrm{MHz\,\mu m^6}$. Because the interaction strength falls off as a power law with separation, the interactions are long-range in the sense that an excitation can influence the state of many nearby atoms far beyond nearest neighbours. Therefore the effective interaction strength depends on the local density of atoms n_0, such that a convenient parameter characterising the interaction strength between neighbouring atoms in the Rydberg state is $J = C_6 {n_0}^2 \sim 10\,\mathrm{MHz}$ for typical atomic densities in our experiments.

3.2.4 Dissipation from decay and dephasing

The state of the atoms is not only influenced by coherent driving and interactions, but also by decay of excited states and pure decoherence mechanisms. These dissipative processes are irreversible and break the conservation of total energy. In particular, our system also realises decay to states which are not coupled by the internal (de)excitation dynamics, for instance by decay to a subset of decoupled hyperfine states of the ground state manifold or ionised states, leading to non-conservation of the total particle number also. This will be an important property in our experiments, which we make use of as an observable in chapters 5 & 6.

One source of decay in the experiments reported in this thesis is coupling to the vacuum electromagnetic field modes, i.e. spontaneous decay. The electromagnetic field has many degrees of freedom, corresponding to all possible directions of the emitted photon, making the deexcitation process dominant and essentially irreversible. Additionally, we treat the coupling to the environment electric fields as not being part of the system, such that this contribution to the evolution of the system is non-unitary and causes decoherence [171]. The spontaneous decay rate in vacuum has the form $\Gamma = \frac{\omega^3}{3\pi\epsilon_0\hbar c}|\mathbf{d_{eg}}|^2$ and is dominated by transitions to low energy states due to the ω^3 scaling of the spontaneous decay rate. Thus Rydberg states have a much larger lifetime compared to low energy atomic states. For Rydberg states an additional cause of decay is the coupling to finite temperature blackbody radiation [96], for which approximate expressions are documented in [181]. Typical combined decay rates including spontaneous and blackbody contributions are $\Gamma/2\pi \sim 10\,\mathrm{kHz}$. If excitation to Rydberg states is carried out while the atoms are held

in an optical dipole trap, an additional photoionisation loss is possible [116, 175]. For Rydberg $|ns\rangle$ states photoionisation rates lie below 1 kHz, while for Rydberg $|np\rangle$ states photoionisation has a typical magnitude of $\sim$ 10 kHz for principle quantum numbers ~ 40. [166, 167, 116]

We describe decay by the Lindblad superoperators given in equation (3.4). To include particle loss out of this internal state space due to decay, the modified operator

$$\mathcal{L}(\hat{\rho}) = \hbar \sum_j \left[(1-b) L_j \hat{\rho} L_j^\dagger - \frac{L_j^\dagger L_j \hat{\rho} + \hat{\rho} L_j^\dagger L_j}{2} \right] \tag{3.9}$$

can be used. The branching parameter $0 \geq b \geq 1$ gives the ratio of decay to coupled and uncoupled states, with the total particle number conserved for $b = 0$. In our experiments we observe that $b \sim 0.1$. The jump operator L_j for decay acts on individual atoms and is defined as

$$L_j = \sqrt{\Gamma} \left| g_j \right\rangle \left\langle e_j \right| . \qquad \Rightarrow \qquad \mathcal{L}(\hat{\rho}^{(j)}) = \hbar\Gamma \begin{pmatrix} -\rho_{ee}^{(j)} & -\rho_{eg}^{(j)}/2 \\ -\rho_{ge}^{(j)}/2 & (1-b)\rho_{ee}^{(j)} \end{pmatrix} \tag{3.10}$$

In the last step we gave the Lindblad decay operator from equation (3.9) explicitly, using the single spin density matrix components $\rho_{\alpha\beta}^{(j)}$. We note that the given form of the Lindblad decay operator is not trace preserving by incorporating the loss of particles.[6] This loss with rate $b\Gamma\rho_{ee}^{(j)}$ depends on the bare particle loss rate $b\Gamma$ and the population of the excited Rydberg state, leading to a macroscopic loss rate by ensemble averaging. Since this particle loss couples population of the Rydberg state to the total population, the driven-dissipative evolution of the internal many-body state can depend on the previous evolution of the system, which is sometimes referred to as non-Markovian evolution. This may have important consequences on the dynamics of the many-body system. In chapters 5 and 6 we will explore possible consequences of the particle loss dynamics on the non-equilibrium dynamics and phase structure of Rydberg spin systems.

In addition to decay, our system is influenced by pure dephasing, e.g. from laser phase noise, which reduces coherences in the system and broadens the apparent spectral width of transition resonances. Assuming that the dephasing mechanisms are spatially uncorrelated they can be accounted for by equation (3.4) and the phenomenological local jump operator [182, 183]

$$L_j^{\mathrm{de}} = \sqrt{\gamma_{\mathrm{de}}} \left| e_j \right\rangle \left\langle e_j \right| . \qquad \Rightarrow \qquad \mathcal{L}^{\mathrm{de}}(\hat{\rho}^{(j)}) = \hbar\gamma_{\mathrm{de}} \begin{pmatrix} 0 & -\rho_{eg}^{(j)}/2 \\ -\rho_{ge}^{(j)}/2 & 0 \end{pmatrix} \tag{3.11}$$

The explicit form of the dephasing operator $\mathcal{L}^{\mathrm{de}}$ shows that it has the effect of reducing coherences. In our experiments, typical dephasing rates are $\sim$ 100 kHz.

3.2.5 Mapping to a spin system

In the previous sections we have established that in our experiments the coupled atom-light system isolates an effective two-level system between the atomic ground state and a targeted

[6] The quantum master equation is trace preserving if the Lindblad superoperator $\mathcal{L}$ is extended to include the shelving state, i.e. $\mathcal{L}(\hat{\rho}) = \hbar \sum_j \left[b \left| s_j \right\rangle \left\langle e_j \right| \hat{\rho} \left| e_j \right\rangle \left\langle s_j \right| + (1-b) L_j \hat{\rho} L_j^\dagger - \frac{L_j^\dagger L_j \hat{\rho} + \hat{\rho} L_j^\dagger L_j}{2} \right]$.

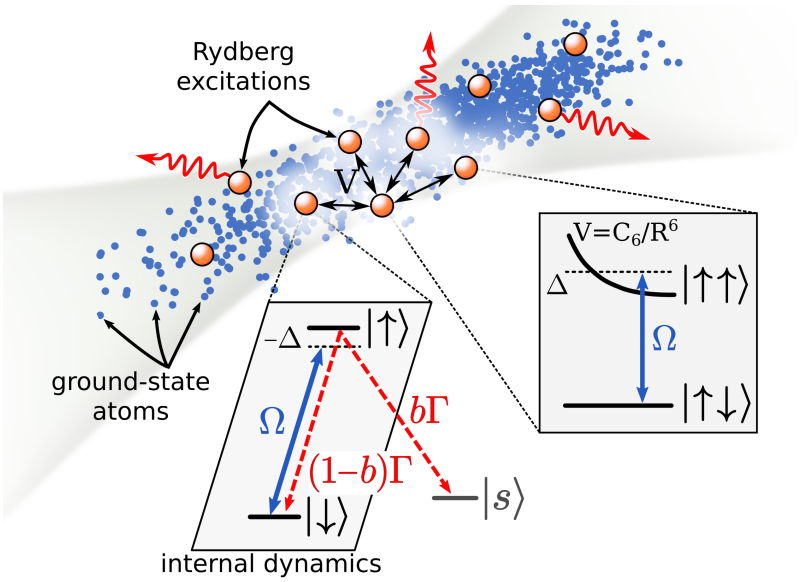

Figure 3.2: Prototypical non-equilibrium quantum spin system based on a laser trapped gas of ultracold atoms driven to Rydberg states and subject to decay. Ground state atoms are depicted as blue dots and identified as $|\downarrow\rangle$ state, which are suspended in a cigar-shaped trapping geometry throughout the temporal evolution. The optical dipole trap is indicated as a grey shaded area in the background. An external coherent laser source drives transitions between the ground state and the highly excited Rydberg state, which is depicted as red spheres ($|\uparrow\rangle$). The driving field is parametrised by the driving strength Ω and detuning Δ, which compete with the decay rate Γ and Rydberg-Rydberg interactions V in the internal state space. Decay of excited states may transfer population to the ground state, which is coupled by the driving laser fields, or to decoupled shelving states $|s\rangle$. Both lead to dissipation of excitation energy, and the latter additionally leads to particle dissipation. Pairs of Rydberg excitations interact via repulsive van der Waals interactions V altering the pair state energy, which have a long-range power law shape.

Rydberg state. Thereafter we found that the van der Waals interactions Rydberg pair states act as a perturbation to the pair state energy, for which the two-level approximation is appropriate. This allows us to identify the two-level atom as a pseudo-spin 1/2 system, assigning $|\downarrow\rangle = |g\rangle$ and $|\uparrow\rangle = |e\rangle$ and introducing the Pauli spin matrices σ_x and σ_z. The full Hamiltonian, comprising both atom-light coupling and Rydberg-Rydberg interactions, can then be written as

$$\mathcal{H} = -\frac{\hbar\Delta}{2}\sum_j \sigma_z^{(j)} + \frac{\hbar\Omega}{2}\sum_j \sigma_x^{(j)} + \frac{\hbar C_6}{2}\sum_{k,j\neq k}\frac{n^{(k)}n^{(j)}}{|\mathbf{r_j}-\mathbf{r_k}|^6}. \tag{3.12}$$

The operator $n^{(j)} = (\sigma_z^{(j)} + 1)/2$ projects on the excited state. We discuss the phase structure of this many-body Hamiltonian in section 3.3.2 for repulsive interactions, which is the relevant case for this thesis.

The driven-dissipative Rydberg spin system emulated by our experiments is depicted in Figure 3.2. Here, the state of the system is determined by the external longitudinal field Δ, transverse field Ω, long-range spin-spin interactions parametrised by C_6 and decay to internal $|\downarrow\rangle$ states or external shelving $|s\rangle$ states.

In the next section we will discuss important phenomena emerging for many-body Rydberg spin systems in the limit of weak or no dissipation, including Rydberg blockade

and facilitated excitation as well as Rydberg dressing and equilibrium many-body phases.

3.3 Emergent many-body effects in Rydberg-interacting driven systems

In the course of this thesis we aim to explore the large parameter space afforded by the interplay of driving (Ω and Δ), dissipation (Γ and γ_{de}) and interactions ($J = C_6 {n_0}^2$). We introduced the relevant frequency scales for our experiment in the previous section already. To set the stage for this task, we will now introduce a number of many-body effects of Rydberg spin systems arising in special parameter regimes. We will focus on those phenomena applicable to the low-temperature, homogeneous atomic gas regime realised in our own experiments.

3.3.1 Rydberg blockade and facilitation dynamics

For strongly interacting systems the dynamical evolution of an atom strongly depends on the state of its neighbours. On resonance ($\Delta = 0$) the interaction energy shift equation (3.8) of an excited atom can suppress the excitation of neighbouring atoms. This effect is called Rydberg blockade [184, 96, 112, 185, 186] and originates from the competition between the interaction energy and the excitation bandwidth. Thus only atoms sufficiently far away from the seed can undergo a transition where the energy shift due to the interactions is sufficiently small. For weak dissipation the excitation bandwidth is dominated by power broadening with width $\hbar\Omega$ giving the blockade condition $V \geq \hbar\Omega$ and therefore a characteristic blockade distance

$$r_b = \left(\frac{C_6}{\Omega}\right)^{1/6}. \tag{3.13}$$

Rydberg blockade leads to an effective reduction of accessible many-body states since multiply excited are far-detuned inside a blockade volume. This effect is of particular interest for quantum information processing since it can be utilised to realise fast two-qubit gates [187, 184, 167, 188] (for reviews see [112, 97]). Additionally, Rydberg blockade was found to lead to collective excitation of entangled states [189, 186, 190] and spatial correlations of excitations in the system [191]. Within a Rydberg blockade volume, only states comprising a single Rydberg excitation can be accessed, which is given by the totally symmetric Dicke state $\sum_i |g_1 \ldots, e_i \ldots, g_N\rangle / \sqrt{N}$ for N atoms within the blockade volume.[7] The excited many-body state is a fully entangled state, opening the possibility for deterministic entanglement creation [192]. Effectively Rydberg blockade reduces the entire multi-atom system within the blockade volume to an effective two-level system, which is sometimes called superatom [193]. Its driving strength is collectively enhanced to $\sqrt{N}\Omega$.[8] We would like to point out that the emergence of this new energy scale makes the definition of the blockade radius ambiguous, with the collectively modified blockade radius being

$$r_b = \left(\frac{C_6}{\sqrt{N}\Omega}\right)^{1/6}. \tag{3.14}$$

[7] The light field preserves symmetry under particle exchange

[8] These simple phenomenological definitions are in good agreement with the cited experiments as well as numerical many-body simulations [194]

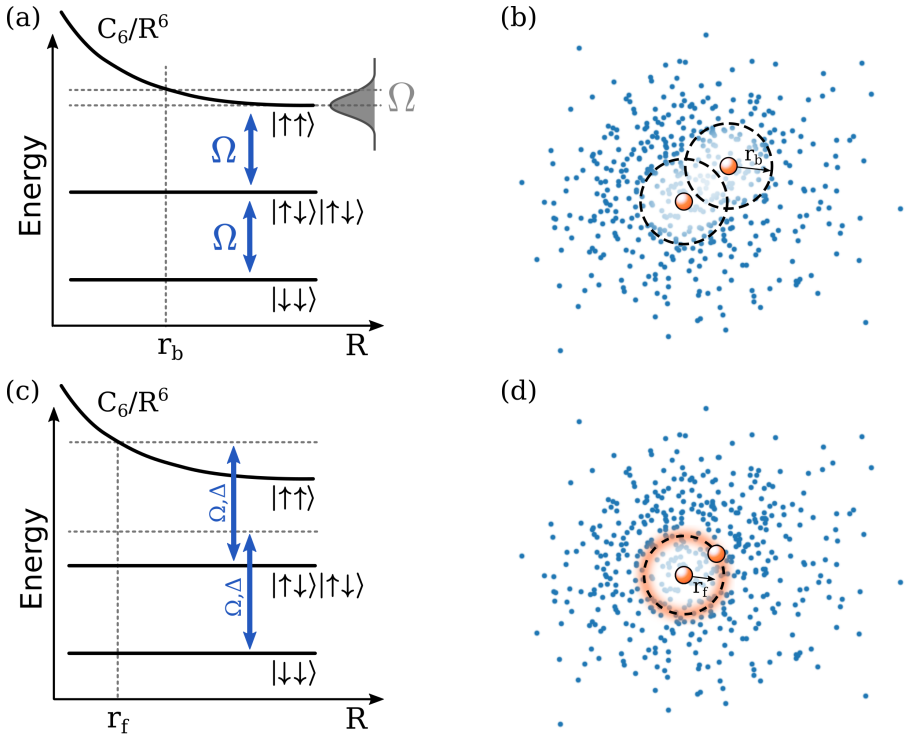

Figure 3.3: Collective effects in Rydberg excitation for two atoms. For resonant excitation (a,b) the long-range powerlaw tail of the interaction potential leads to Rydberg blockade. (a) For large separations R, both atoms can be excited simultaneously. Below a critical distance r_b, determined by the excitation bandwidth Ω, the doubly excited state $|\uparrow\uparrow\rangle$ becomes off-resonant, giving rise to the excitation blockade. (b) Sketch of the Rydberg blockade effect in an atomic cloud. A Rydberg excitation is associated with a blockade volume denoted by a dashed line, inside which no further atoms can be excited. Far away from resonance (c,d) the excitation dynamics is dominated by facilitation. An off-resonantly excited Rydberg seed leads to resonant excitation of further Rydberg atoms for separations R in the vicinity of the facilitation radius r_f, where the detuning compensates the Rydberg-Rydberg interaction potential. Inside the facilitation radius Rydberg blockade suppresses further excitation.

Here, N has to be determined self-consistently from the blockade volume V_b and the atom density n_0. We will be able to determine in chapter 5 the relevant blockade scale in our experiments.

In the case of a large detuning from resonance ($|\Delta| \gg \Omega$) with the same sign as the interactions, a present excitation will shift the excited state energy of atoms at a specific distance into resonance ($\Delta = V$), leading to the opposite effect to blockade which is referred to as anti-blockade [195] or facilitation, illustrated in Figure 3.3(c). The facilitation distance is given by the competition between detuning and interactions as

$$r_f = \left(\frac{C_6}{|\Delta|}\right)^{1/6}. \tag{3.15}$$

Based on Rydberg facilitation, for example the dynamical creation of Rydberg aggregates [121, 122, 123], optical bistability [124, 125, 126, 127] and the observation of kinetic constraints [196, 93] has been reported.

3.3.2 The coherent Ising-like quantum spin system

The non-dissipative Rydberg spin system has been explored intensively, where the quantum state of the system is governed purely by the Hamiltonian (3.12). Then the longitudinal and transversal fields realised by the laser driving and Rydberg-Rydberg interactions govern the system. It closely resembles the quantum Ising model with long-range interactions [197, 190]. The correlations between Rydberg excitations [194] arising from repulsive van der Waals interactions (realised in all our experiments) are predicted to endow the many-body ground state with crystalline long-range order for $\Delta \gg \Omega$ [132, 198], which has also been successfully observed in mesoscopic systems [199]. Moreover, [197] revealed the phase diagram of this system, which we show in Figure 3.4. It features a second order quantum phase transition at $\Omega,\ \Delta = 0$ connecting a crystalline phase of regularly spaced Rydberg excitations ($\Delta > 0$) to a paramagnetic phase of weakly excited atoms without correlations ($\Delta < 0$). For finite driving strengths close to the critical point an additional quantum critical region appears. The notion of phase transitions and critical states was introduced in section 1.2.1. In a quantum system, the properties of the individual phases are given by the respective energy ground states of the many-body system. At the quantum critical point, the energy gap between crystalline and paramagnetic many-body eigenstates becomes zero, creating a nonanalytic point in the ground state energy. [200] For finite Ω the energy gap between the ground state and higher energy states becomes finite, giving rise to the quantum critical region close to resonance. In this regime the behaviour of the order parameter is governed by the vicinity to the critical point as a function of the driving strength, leading to powerlaw scaling. Microscopically, the vicinity to the critical point is determined by the collectively enhanced Rydberg blockade introduced in equation (3.14). [197] based their investigations of the phase structure of Rydberg spin systems on mean field calculations which incorporate the density-density correlations of the Rydberg blockade to lowest order and use the fraction of Rydberg excitation m as the order parameter.[9] The predicted on-resonance critical scaling $m \propto \Omega^{\alpha}$ has a mean field scaling exponent $\alpha_{\mathrm{MF}} = 2/5$ in three dimensions. Powerlaw scaling is also predicted in the critical phase as $m \propto \Delta^{\beta}$ with $\beta_{\mathrm{MF}} = 1/2$ (also in three dimensions). Subsequent experiments by [201] revealed the resonant critical scaling as a function of Ω for the first time in an experiment. These theoretical and experimental efforts combined established that the Rydberg-interacting spin system belongs to a new universality class.

It is an important question whether, and under which conditions, properties of the equilibrium and non-equilibrium phase structures are linked. In this thesis we will explore such connections experimentally and theoretically in chapter 5. To this end, we will extend the afore-mentioned theoretical mean field treatment of the coherent Rydberg spin system to its non-equilibrium counterpart in section 3.4.1. This will provide us with a powerful tool to guide our experimental explorations.

3.3.3 Rydberg dressing

We have seen that atoms excited to Rydberg states offer a promising approach to create strongly correlated matter allowing us to engineer the strength and range as well as the anisotropy of the interactions. However, the energy scale associated with the Rydberg-Rydberg interaction ($J/2\pi \sim 10\,\mathrm{MHz}$) is incompatible with the energy scales of driving and

[9] This model is extended to dissipative Rydberg spin systems in the following section.

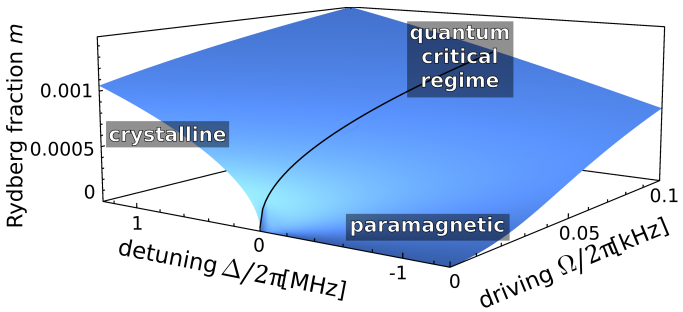

Figure 3.4: Phase structure of a quantum many-body system with van der Waals Rydberg-Rydberg interactions as a function of the laser driving parameters Ω (strength) and Δ (detuning). The ground state of the continuously driven system is characterised by the Rydberg fraction as the order parameter and shows a second order phase transition at $\Omega, \Delta = 0$. It separates a paramagnetic phase of low excitation fraction from a phase of high excitation fraction with crystalline order. Around $\Delta = 0$ and for finite Rabi frequencies, these two phases are separated by a quantum critical regime.

dissipation (Ω, $\Gamma + \gamma_{\mathrm{de}} \lesssim 2\pi \cdot 100\,\mathrm{kHz}$), making a large sector of highly excited many-body states inaccessible. Additionally, the relatively short lifetime of Rydberg states ($\sim 10\ \mu$s) is seemingly incompatible with the typical time scales associated with ultracold atomic motion or equilibration ($\sim 10\,$ms). A possible resolution is offered by off-resonant driving, as was first proposed in [202], realising "Rydberg dressed" states. Here, the atomic state of each atom is described by a coherent superposition of the atomic ground $|g\rangle$ and Rydberg $|e\rangle$ states as $|\psi\rangle \approx |g\rangle + \beta\,|e\rangle$. The small Rydberg-state admixture $\beta \ll 1$ is tunable by the laser driving parameters. If the laser detuning can compensate the interaction ($\Delta = V(R)$), an avoided crossing is created at separation R which strongly mixes ground and excited states. In the opposite case the resulting interaction potential of a pair of Rydberg dressed atoms shows a characteristic soft-core potential, as is illustrated in Figure 3.5. It arises from the Rydberg blockade in second order light coupling between the $|gg\rangle$ and $|ee\rangle$ pair states. Its characteristic size is approximately given by the facilitation radius (eq. 3.15) and its maximum strength ($R \to 0$) is proportional to β^3. This interaction strength is shared amongst all particles within the interaction range, such that the strongest interaction effect is expected for intermediate densities where on average two atoms share an interaction volume [138]. Outside the characteristic distance the Rydberg dressed atoms do not interact significantly, leading to essentially independent atoms which each exhibit an energy shift $\beta^4 V$. At the same time, the decay strength of the dressed atoms is reduced to $R_{\mathrm{sc}} = \beta^2\Gamma$, which would allow Rydberg dressed atoms to coherently evolve under the influence of strong and long-range interactions for up to tenths of a second.

The presented Rydberg dressing idea has generated considerable research efforts, with predicted many-body phenomena ranging from novel strongly correlated phases [105, 203, 106, 137, 136, 104, 204], phases with topological order [168], to solitons in a BEC [205] and proposed applications for quantum annealing [206]. Effects of Rydberg dressing haven been predicted to be measurable as mechanical deformations of Bose Einstein condensates [207, 208], however, first experiments have been unsuccessful [138] because of the large densities in BECs suppressing the interaction strength. As an alternative, Ramsey interferometry has been proposed [209]. Further experiments in large systems were also unsuccessful in observing signatures of Rydberg dressed interaction because of reported

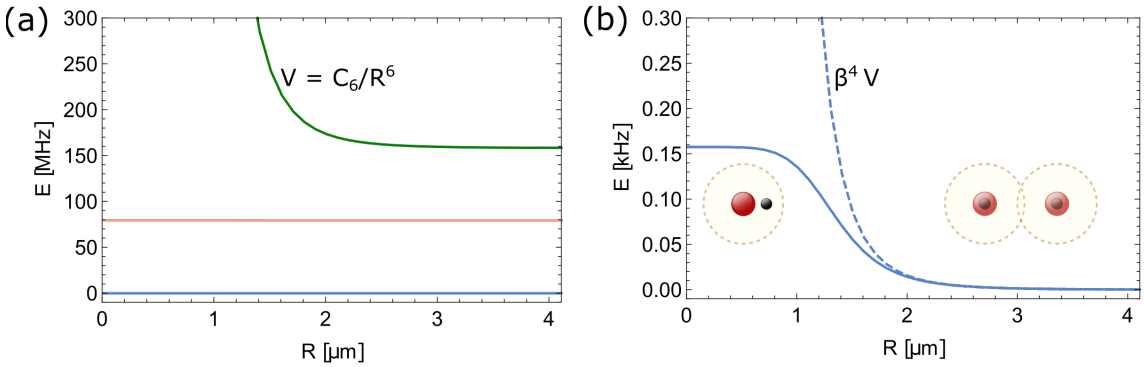

Figure 3.5: Soft core interaction potential between two dressed Rydberg atoms. (a) The dressed pair energies for the same laser parameters as given in chapter 4 in the case of negative detuning and repulsive interactions. Starting from lowest energy, the depicted eigenstates are the dressed pair ground state and dressed singly and doubly excited states. (b) Zoom in on the dressed ground state, which shows a characteristic soft core potential (solid line). For large separations, independent atom behaviour with a small energy shift $\beta^4 V$ per atom is recovered (dashed curve).

anomalous interaction induced broadening [98, 120]. However, Rydberg dressing has been successfully applied to mesoscopic systems to entangle two atoms [210] and to observe coherent evolution of approximately 100 atoms in a quantum gas microscope [211, 212].

In chapter 4 we will explore the Rydberg dressing concept further and establish optimal parameter regimes for Rydberg dressing minimising decay and maximising interactions. To this end we will theoretically study the minimal system of two atoms with the full master-equation treatment introduced previously in this chapter, allowing us to self-consistently determine the relevant interaction and dissipation characteristics.

In chapters 5 and 6 we will experimentally explore the dynamics and phase structure of open Rydberg quantum spin systems. To establish quantitative links between our macroscopic observations and the microscopic model description, we will introduce approximate models in the next section, which can be solved efficiently.

3.4 Approximate models for efficient simulation

To solve the quantum master equation introduced in section 3.1 is computationally intractable for large systems with atom numbers $\gtrsim 10$ and long times since the Hilbert space of the many-body system grows exponentially with spin number. To facilitate a model description of our experiments and to guide the interpretation of our results we will now introduce two approximate models reducing the complexity of the description to a mean field model with approximate two-point correlations and a classical master equation.

All our reduced models can be derived starting from a set of coupled single-atom quantum master equations. As was shown in section 3.1, single-atom quantum master equations can be obtained from the quantum master equation governing the density matrix $\hat{\rho}$ of the full system by tracing over all other atoms:

$$\partial_t \hat{\rho}^{(j)} = \mathrm{Tr}_{k\neq j} \partial_t \hat{\rho}. \tag{3.16}$$

The dynamics of each atom j is given by single-body dissipation and the Hamiltonian

$$\mathcal{H}^{(j)} = -\frac{1}{2}(\Delta - V_j)\sigma_z^{(j)} + \frac{\Omega}{2}\sigma_x^{(j)} \qquad \text{with} \qquad V_j = \sum_{k\neq j} V_{jk}\rho_{ee}^{(k)}, \tag{3.17}$$

where the effect of the sum of all Rydberg pair interactions on atom j is captured by V_j. We also set $\hbar = 1$ in the following.

3.4.1 Mean-field approximation including two-point correlations

This subsection is based on the following manuscript, from which parts of the text are reproduced verbatim with permission by the American Physical Society:
Uncovering the non-equilibrium phase structure of an open quantum spin system
S. Helmrich, A. Arias and S. Whitlock
submitted to Physical Review X

Mean-field theory provides a relatively simple way to qualitatively understand the different phases of the driven dissipative spin system by providing analytic expressions for the magnetisation. The mean-field equations can be obtained by assuming each spin interacts with the average field produced by all other spins. However, to account for the strong correlations which arise due to the Rydberg blockade effect (cf. sec. 3.3.1) in a self-consistent way, we include a distance dependent cutoff to the interaction term V_j. This model has previously been shown to reproduce the quantum critical behaviour associated with the antiferromagnetic Ising model in the absence of dissipation [197, 201, 119]. Here we extend this description to open system dynamics, by applying the self-consistent mean-field approximation to the full master equation (eq. (3.3)). In the following we briefly describe the derivation of this model and its quasi-steady-state magnetisation. We will present the derivation for arbitrary dimensions d and Rydberg-Rydberg interactions with power law exponent $p > d$, which is the experimentally relevant regime. In chapter 5 we will experimentally explore the phase structure of our Rydberg spin system and in our discussion also draw on the mean field model presented here. There, further inspection of the mean-field solution will allow us to identify different regimes of behaviour.

Mean-field theory applies an approximation to many-body terms, which in our system are given by the Rydberg-Rydberg interactions. This approximation is given by

$$V_j \to \sum_{k\neq j} V_{jk} m g_2\big(|\mathbf{r_j} - \mathbf{r_k}|\big). \tag{3.18}$$

This describes the effective interaction of a single spin with all other spins weighted by the local average Rydberg fraction m. Following [197], we approximate the two-point correlation function by the Heaviside step function $g_2(|\mathbf{r}|) = \Theta(|\mathbf{r}| - r_\mathrm{c})$, where r_c is a characteristic distance for the correlations characterising blockade and facilitation. Next we replace the discrete sum by an integral with homogeneous local atom density n_0,

$$V_j \approx \int_{r_\mathrm{c}}^{\infty} m n_0 V_{jk}\, \mathrm{d}^d\mathbf{r_k}, \tag{3.19}$$

which is a good approximation in the experimentally relevant situation that the mean interparticle distance is much less than r_c. Substituting $V_{jk} = C_p/|\mathbf{r_j} - \mathbf{r_k}|^p$ (where $p = 6$

for van der Waals interactions) and using the spherical symmetry allows one to carry out the integration explicitly. Furthermore, we self-consistently set r_c by requiring that there is on average only one excitation within the correlation distance due to Rydberg blockade [102], $\int n_0 m\big(1 - g_2(\mathbf{r})\big)\, \mathrm{d}^d\mathbf{r} \equiv 1$, yielding:

$$V_j = \frac{C_p d\,(m n_0 \mathcal{V}_d)^{p/d}}{p-d} = Jc\,m^{p/d}, \tag{3.20}$$

where we have introduced the volume of the d-dimensional unit sphere $\mathcal{V}_d$ and $c = \mathcal{V}_d{}^{p/d} d/(p-d)$ is a dimensionless constant. Thus the mean-field interaction strength is parametrised by $Jm^{p/d} = C_p n_0 m^{p/d}$, which is the interaction coefficient times the average local density of Rydberg excitations.

The resulting mean-field Hamiltonian, using $n = (\sigma_z + 1)/2$ and dropping the atom index (j) as well as a constant energy offset, is

$$\mathcal{H} = -\frac{1}{2}\left(\Delta - Jc\,m^{p/d}\right)\sigma_z + \frac{\Omega}{2}\sigma_x, \tag{3.21}$$

which can be readily inserted into the master equation (3.16) for the single-spin density matrix $\hat{\rho}$. The mean-field master equation is solved self-consistently for the Rydberg population $m = \mathrm{Tr}[\hat{\rho}\,] = \rho_{ee}$, whose solution can be expressed implicitly for small Rydberg fraction as

$$\Omega^2 \approx \left(4\big(\Delta - Jc\,m^{p/d}\big)^2 + (\Gamma + \gamma_{\mathrm{de}})^2\right)\frac{m\Gamma}{\Gamma + \gamma_{\mathrm{de}}}. \tag{3.22}$$

In chapter 5 we will discuss the different regimes of this solution and the resulting different regimes of non-equilibrium behaviour, in association to our experimental exploration of the phase structure of driven-dissipative Rydberg spin systems. There, a numerical solution of the Rydberg fraction as a function of detuning and driving strength is provided in Figure 5.4(b). We would like to point out here already that the dissipative mean field model predicts in the string driving limit the same resonant critical scaling as in the non-dissipative equilibrium case described above (cf. sec. 3.3.2). It remains for our experiments to see whether such critical behaviour can be found away from equilibrium.

3.4.2 Classical master equation model

To efficiently simulate many-body systems, including e.g. disordered microscopic atom distributions and effects due to the locally varying cloud trapping potential, we introduce the classical master equation model (also known as rate equation model). It is valid for long times, where decoherence processes and decay have washed out phase coherence in the system, which is the studied regime in our experiments.

The main idea behind the classical master equation model is to reduce the full quantum master equation (3.3) to a rate equation of populations. This can be achieved by adiabatically eliminating coherences on the single atom level [195, 213, 94] given by equation (3.16). This is sufficient since coherent transitions $\propto \sigma_x^{(j)}$ and dissipation processes only act on individual spins, while the Rydberg-Rydberg interactions $V_{jk} = C_6/|\mathbf{r_j} - \mathbf{r_k}|^6$ act as an additional local detuning on atom j [213]. We perform the adiabatic elimination step on $\partial_t \hat{\rho}^{(j)}$ by setting the temporal evolution of off-diagonal coherences ($\partial_t \rho^{(j)}_{\alpha\beta}$ for $\alpha \neq \beta$) to

zero, which is a valid approximation on time scales $t > {\gamma_{\mathrm{de}}}^{-1}$. Solving for the coherences we finally obtain rate equations for the total population $n^{(j)} = \rho_{gg}^{(j)} + \rho_{ee}^{(j)}$ and the population of the excited state $\rho^{(j)} = \rho_{ee}^{(j)}$ of a two-level atom

$$\begin{aligned} \partial_t \rho^{(j)} =& \Gamma_\uparrow (n^{(j)} - \rho^{(j)}) - \Gamma_\downarrow \rho^{(j)} \\ \partial_t n^{(j)} =& -b\Gamma \rho^{(j)}, \end{aligned} \tag{3.23}$$

with the microscopic excitation and deexcitation rates $\Gamma_\uparrow$ and $\Gamma_\downarrow$ respectively. For the last equation above we have taken into account the finite particle dissipation with rate $b\Gamma$.

The processes coupling the various microstates of the system can be expressed elegantly by the microscopic rates $\Gamma_\uparrow$ and $\Gamma_\downarrow$, which reveal the competition between the energy scales for driving (detuning Δ and strength Ω), dissipation Γ and pair interactions $V_j = \sum_{k \neq j} V_{jk} \rho_{ee}^{(k)}$ very naturally.

$$\begin{aligned} &\text{Excitation rate of atom } j\text{:} && \Gamma_\uparrow^{(j)} = \frac{(\Gamma + \gamma_{\mathrm{de}})\Omega^2}{(\Gamma + \gamma_{\mathrm{de}})^2 + 4\big(\Delta - V_j\big)^2} \\ &\text{Deexcitation rate of atom } j\text{:} && \Gamma_\downarrow^{(j)} = \Gamma_\uparrow^{(j)} + \Gamma \\ &\text{Loss rate of excited atom } j\text{:} && \Gamma_{\mathrm{loss}}^{(j)} = b\Gamma \end{aligned} \tag{3.24}$$

This classical many-body master equation can be solved efficiently using kinetic Monte Carlo techniques [214], including the temporal evolution. Furthermore, this model retains the local information of the atom positions within an atom cloud, such that the locally varying distribution of atom density and trap lightshifts can be accounted for in a simulation. This will allow us to compare our experimental observations in chapter 5 to classical rate equation simulations directly. We use the implementation presented in [215]. Additionally, we incorporate the effect of motion, which is described in appendix A.

In the framework of the classical master equation we recover the illustrative picture discussed in the section 3.3.1, in which an atom in the Rydberg state shifts the Rydberg states of nearby atoms out of or into resonance of the excitation transition. For resonant laser driving ($\Delta = 0$) this results in Rydberg blockade, and for far off-resonant driving ($|\Delta| \gg \Omega,\ \Gamma + \gamma_{\mathrm{de}}$) compensating the interactions V_j we can identify facilitation. In the latter case the excitation rate separates into fast near-resonant excitation (rate Γ_f) facilitated by neighbouring seed excitations for $\Delta \approx V_j$, and slow off-resonant excitation (rate Γ_s) for $\Delta \not\approx V_j$. These excitation rates, as well as the corresponding externally driven deexcitation rates, can be approximated by

$$\Gamma_f \approx \frac{\Omega^2}{\Gamma + \gamma_{\mathrm{de}}}, \qquad \Gamma_s \approx (\Gamma + \gamma_{\mathrm{de}}) \frac{\Omega^2}{4\Delta^2}. \tag{3.25}$$

Facilitation and seed (de)excitation additionally compete with decay and loss of excited atoms in our system. In combination, these microscopic transition rules bear striking similarities to the processes leading to absorbing state phase transitions discussed in section 1.2.2. Facilitation then acts analogously to branching (facilitated excitation) and coalescence (facilitated deexcitation), while the correspondence of decay is direct. However, the slow off-resonant excitation in principle introduces a small amount of fluctuations to any absorbing state, making it an open question whether the perturbation is sufficiently small to allow one to observe features of an absorbing-state phase transitions in our experiments.

Also the influence of the particle loss on this dynamics, including potential non-Markovian evolution suggested in section 3.2.4, can be elucidated in our experiments. We will perform such experiments in chapter 6 and interpret these building on the presented analogy between microscopic processes in the facilitation limit and the processes leading to absorbing state phase transitions.

Conclusion

In this chapter we showed that ultracold atoms excited to Rydberg states provide an experimental platform which is well suited to emulate driven-dissipative quantum spin systems. In our experiments, the Rydberg excitation laser isolates an effective pseudo-spin 1/2 within the manifold of atomic states, whose dynamics is governed by the external laser driving, dissipation and interactions between Rydberg states. Subsequently we showed how these microscopic processes can be described within the framework of the Lindblad quantum master equation in terms of Hamilton and Lindblad operators, such that the whole non-equilibrium dynamics of the spin system can in principle be described. Thus we have shown that we can both create non-equilibrium spin systems in the laboratory and also describe the microscopic processes governing their dynamics. In the next chapter we will extend our discussions to include effects of intermediate states weakly populated by two-photon excitation on the resulting interaction and dissipation characteristics of Rydberg atoms. In combination, the theoretical description introduced in this chapter puts us in a position where we will be able to explore quantitative links between macroscopic observations in the experiments and microscopic model descriptions in the following chapters.

Based on the microscopic properties of Rydberg spin systems, we reviewed emerging many-body properties of such systems, which will also influence the non-equilibrium dynamics observed in this thesis. In the last part of this chapter we introduced the dissipative mean field and classical master equation as approximate models of our system, which we will use to efficiently describe and interpret our experimental findings to establish the various regimes of non-equilibrium behaviour emerging in our system. An important feature of our system is particle dissipation, in addition to dissipation of energy, which can lead to non-Markovian evolution on times long compared to the inverse effective particle loss rate. In chapter 5 we will first study the many-body dynamics on timescales where the impact of particle loss on the dynamics of the spin-1/2 system is small, and establish the non-equilibrium phase structure of the system in this limit. Thereafter, we will study the full temporal dynamics in the facilitating limit, including non-Markovian effects, to explore the striking analogy between classical (de)excitation processes occurring in our system and processes leading to absorbing state phase transitions. Beforehand, we will use the quantum master equation of our system and apply it to explore the microscopic properties of atoms dressed to Rydberg states by multiple laser fields in the next chapter.

Two-body interactions and decay of Rydberg-dressed atoms

4

This chapter is based on the following publication, from which parts of the text are reproduced verbatim with permission by IOP Publishing:

Two-body interactions and decay of three-level Rydberg-dressed atoms
S. Helmrich, A. Arias, N. Pehoviak and S. Whitlock
Journal of Physics B: Atomic, Molecular and Optical Physics 49, 03LT02 (2016)

Engineering the properties of synthetic quantum systems at the microscopic level, for example by controlling the shape and range of interactions or the strength of dissipation, is a central capability of modern experimental platforms [24, 74, 75, 76, 92]. For example, this is of great interest for quantum simulation[77, 216, 113, 95], and allows for the creation of novel states of matter [217, 199, 168, 134, 104, 106, 169]. One approach facilitating engineered interactions and dissipation is Rydberg dressing. In this scheme the electronic ground state of atoms is weakly admixed with highly excited Rydberg states by coherent laser coupling [202]. This way the longevity of the ground states is combined with the strong and long-range interactions of the Rydberg states. The Rydberg admixture can be set by the parameters of the laser fields arbitrarily, allowing control over the strength and range of interactions and decay. This way, the seemingly incompatible energy scales associated with the Rydberg-Rydberg interactions ($\sim h \cdot 10\,\mathrm{MHz}$) and atomic motion ($\sim h \cdot \mathrm{kHz}$), as well as the relatively short lifetimes of Rydberg states ($\sim 10\,\mu\mathrm{s}$) compared to the time scales of equilibration ($\sim 10\,\mathrm{ms}$) can be reconciled for small Rydberg admixtures. The typical laser parameter choice for this weak dressing regime is a large detuning from all relevant atomic states ($\Delta \gg \Omega,\ \Gamma$).

The smallest unit for which engineered interactions and decay can be investigated is a binary system. In the following, we will use this minimal unit to explore the large parameter space afforded by multiple dressing laser fields and theoretically analyse the resulting dressed interactions and decay rates. Specifically, we will focus on two and three-level dressing, which are the two most widely used excitation schemes in experiments [201, 112, 97]. So far, theoretical and experimental studies have employed a two-photon excitation scheme with a large detuning from an intermediate state (effective two-level regime) [203, 105, 207, 218, 205, 219, 106, 138, 136, 220, 98, 208] or direct excitation via a single laser field [210, 221, 222, 223, 224, 204, 206, 211, 212]. However, experimentally reaching conditions where lifetimes exceed motional timescales still remains an important challenge. The implementations of two and three-level dressing in our experiments and the achieved laser driving parameters are summarised in sec. 2.3.

To study both interactions and decay self-consistently in a unified framework we will employ the quantum master equation approach in this chapter, whose foundation was

already outlined in sec. 3.1. As a first step we will revisit the quantum master equation and adapt it to a three-level scheme. Thereafter we will will apply it first to the standard Rydberg dressing approach which is far detuned from intermediate and Rydberg states [207]. In the following section we will investigate the full parameter space available to three level dressing to find optimal parameters beyond far detuned dressing for this scheme. We will discover that optimal three-level dressing coincides with destructive interference of the intermediate state population and a cooperative enhancement of the Rydberg admixture due to multiphoton excitations shared by multiple atoms [225]. For these parameters the dressed-state interaction strength and lifetime can be comparable to, or even exceed what is possible for two levels.

4.1 Quantum master equation description

To self-consistently calculate the effective interaction potential U and the residual photon scattering rate R_{sc} as a function of the bare Rydberg-Rydberg interaction strength V we use a quantum master equation treatment which includes spontaneous decay from the excited states. The master equation, which was introduced in sec. 3.1, of the two-particle system is $\partial_t\hat{\rho} = -i[\mathcal{H},\hat{\rho}] + \mathcal{L}[\hat{\rho}]$ (here and in the following we use units where $\hbar = 1$). The Hamiltonian consists of three parts $\mathcal{H} = \mathcal{H}^{(1)} + \mathcal{H}^{(2)} + \mathcal{V}$, where the $\mathcal{H}^{(j)}$ are the individual atom-light Hamiltonians of atom (j), respectively, in the rotating wave approximation (cf. sec. 3.2.2) and $\mathcal{V} = V\left|r_1\right\rangle\left|r_2\right\rangle\left\langle r_1\right|\left\langle r_2\right|$ is the two-body interaction between bare Rydberg states. The superoperator $\mathcal{L}[\hat{\rho}] = \sum_{\{\hat{L}\}} L\hat{\rho}L^\dagger - (L^\dagger L\hat{\rho} + \hat{\rho}L^\dagger L)/2$ describes spontaneous decay of the excited states, where $\{L\}$ is a set of decay operators. Focusing on the three-level ladder system (Fig 4.1(a)), in which each atom is composed of a long lived ground state $|g\rangle$ coupled to the Rydberg state $|r\rangle$ via a short lived intermediate state $|e\rangle$, then

$$\begin{aligned}\mathcal{H}^{(j)} =& \frac{\Omega_e}{2}\left|g_j\right\rangle\left\langle e_j\right| + \frac{\Omega_r}{2}\left|e_j\right\rangle\left\langle r_j\right| \\ &- \frac{\Delta_e}{2}\left|e_j\right\rangle\left\langle e_j\right| - \frac{\Delta}{2}\left|r_j\right\rangle\left\langle r_j\right| + \text{h.c.}\end{aligned} \tag{4.1}$$

Here $\Omega_{e,r}$ denote the Rabi frequencies of the respective laser fields and Δ_e, Δ refer to the one photon and two photon detunings. Additionally, $L^{(j)} = \{\sqrt{\Gamma_e}\left|g_j\right\rangle\left\langle e_j\right|, \sqrt{\Gamma_r}\left|e_j\right\rangle\left\langle r_j\right|\}$ describes spontaneous decay from the intermediate state and the Rydberg state respectively with excited state decay rates $\Gamma_{e,r}$. The states $|g\rangle$ and $|r\rangle$ are not dipole coupled and thus direct decay can be neglected. We neglect possible couplings to other Rydberg states and the much weaker interactions between atoms in the $|g\rangle$ or $|e\rangle$ states. Typically $\Gamma_e \gg \Gamma_r$ and the internal degrees of freedom reach steady state on a timescale $\sim \Gamma_e^{-1}$ which we assume is much faster than typical motional timescales. Therefore it is sufficient to calculate the steady state values of the dressed potential and residual scattering rate for each value of V without explicitly considering the motion of the particles. However, care must be taken applying the same reasoning to the two-level case or to atoms with metastable intermediate states for which internal state dynamics can be much slower.

To calculate $U(V)$ we first solve the master equation for steady state ($\partial_t\hat{\rho} = 0$) and then compute the expectation value

$$U(V) = \mathrm{Tr}[\mathcal{H}\hat{\rho}] - \mathrm{Tr}[\mathcal{H}\hat{\rho}]_{V=0}, \tag{4.2}$$

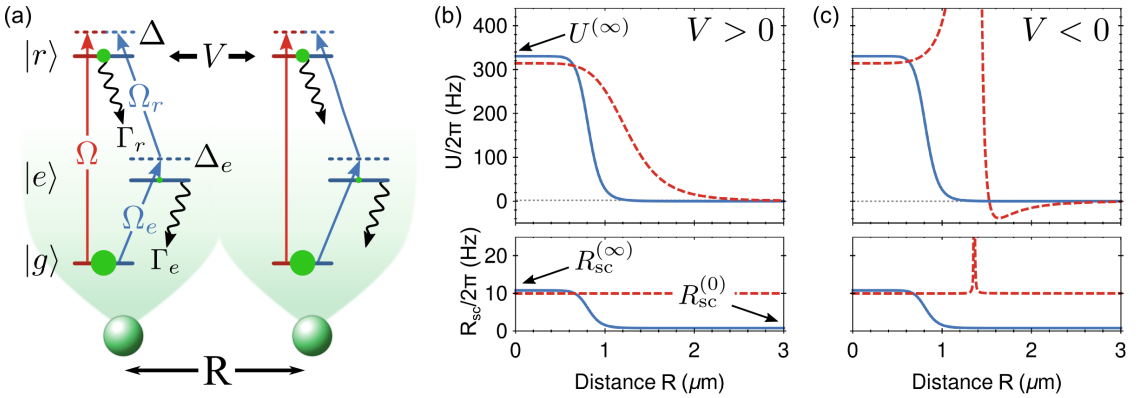

Figure 4.1: (a) Level scheme for two atoms with distance R dressed by one or two laser fields coloured red and blue respectively. (b) Comparison of the interaction strength $U(C_6/R^6)$ and scattering rate $R_{\rm sc}(C_6/R^6)$ for two-level (dashed red lines) and three-level systems (solid blue lines) assuming repulsive van der Waals interactions between Rydberg states. We show repulsive interaction potentials, requiring $\Delta = 0, \Delta_e > 0$ (three-level) and $\Delta < 0$ (two-level). (c) Same as in (b) but for attractive van der Waals interactions. The parameters used for the calculations are given in the text. Reproduced from [226].

where the last term subtracts the single particle light shifts. Similarly, the dressed-atom decay rate (per atom) responsible for heating and loss of dressed atoms is given by

$$R_{\rm sc} = \sum_{\{L\}} \mathrm{Tr}[L\hat{\rho}L^\dagger]/2. \tag{4.3}$$

We define the Rydberg fraction in the non-interacting limit as

$$\beta^2 = \frac{1}{2}\sum_j \mathrm{Tr}\left[|r_j\rangle\langle r_j|\,\hat{\rho}\right]_{V=0}. \tag{4.4}$$

In the next section we will give approximate expressions for Rydberg dressing in two and three level scenarios where the detuning is dominant.

4.2 Detuned two and three-level dressing

In the case of two-level dressing, approximate analytical expressions for the effective interaction potential and the decay rate can be found, which illustrate the Rydberg dressing concept. Example curves are given in Figure 4.1(b). Applying equation (4.2) in the limit of weak dissipation and large detunings as well as under the condition that no facilitation is possible ($\mathrm{sign}(V) \neq \mathrm{sign}(\Delta)$), the dressed interaction potential is, to leading order, given by the soft-core potential

$$U = \frac{\Omega^4}{4\Delta^3}\frac{V(\Delta - V)}{(V - 2\Delta)^2}. \tag{4.5}$$

The effective interaction potential follows the powerlaw dependence of the bare Rydberg-Rydberg interaction for large separations, while "softening" to a plateau of constant interaction energy $U^{(\infty)} = -2\Omega\beta^3$ for close atom pairs as a consequence of the Rydberg

blockade [184]. Outside the blockade distance the atoms are independent with an energy shift of $\beta^4 V$ per atom. Here we have identified $\beta^2 = \Omega^2/(2\Delta)^2$ as the two-level Rydberg fraction. Weak dressing is achieved in the far detuned limit $\Delta \gg \Omega$. The behaviour of the interaction potential reproduces the observed behaviour of the dressed Hamiltonian eigenvalues in sec. 3.3.3. Furthermore, the self-consistently calculated decay rate of dressed atoms is to leading order for all distances R given by

$$R_{\mathrm{sc}} = \Gamma_r \beta^2. \tag{4.6}$$

In adapting the two-level dressing approach to three levels special care must be taken for the very short lived intermediate state. While typical lifetimes of Rydberg states are 10 µs, low energy intermediate states have typical lifetimes three orders of magnitude smaller. The weak dressing approach introduced for two levels can be adapted to three levels by detuning far from the short lived intermediate state ($\Delta_e \gg \Omega_e,\ \Omega_r,\ \Gamma_e$) in addition to detuning far from the Rydberg state. Inspecting the three level quantum master equation of a single atom in this limit, we find that its state is governed by an effective Rabi frequency $\Omega_{\mathrm{eff}} = \Omega_e \Omega_r / |2\Delta_e|$, for which the Rydberg fraction again has the form $\beta^2 = {\Omega_{\mathrm{eff}}}^2/(2\Delta)^2$ as in the two-level case. The decay rate is, to leading order, given by

$$R_{\mathrm{sc}} = \Gamma_e \frac{{\Omega_e}^2}{4{\Delta_e}^2} + 2\Gamma_r \beta^2. \tag{4.7}$$

For large intermediate-state detunings an effective two-level regime is recovered [207].[1], with the two-level interaction potential eq. (4.5) holding approximately. Numerically analysing the three level dressed interaction potential for $\Delta_e \gg \Omega_e,\ \Omega_r,\ \Gamma_e$, we find that achieving strong interactions is challenging for experimentally achievable laser parameters (see also Fig. 4.2 and cf. [228]). The requirement of small decay rates ($\lesssim 10$ Hz) imposes strong limitations on the achievable dressed interaction potential strength to compensate for the fast decay of the intermediate state. Thus we will open our search for optimal dressing conditions to the full parameter space available for three level dressing, allowing for cooperative effects and multiphoton interference to engineer the desired properties.

4.3 Cooperatively enhanced three-level dressing

Generally, the inclusion of the intermediate state can have a dramatic influence on the shape and strength of the dressed interactions as well as the residual decay rate as a function of the interparticle separation d. Figures 4.1(b,c) show calculated two-body dressed state potential energy surfaces $U(C_6/R^6)$ and decay rates $R_{\mathrm{sc}}(C_6/R^6)$ for the two-level and three-level systems assuming van der Waals interactions with strength $C_6/2\pi = \pm 1.0$ GHz μm^6, which is typical for e.g. alkali atoms excited to principal quantum number $n \sim 40$. Furthermore, the following achievable experimental values were assumed: $\Gamma_e/2\pi = 6.0$ MHz, $\Gamma_r/2\pi = 10$ kHz, $\Omega_e/2\pi = 1.2$ MHz, $\Omega_r/2\pi = 200$ MHz, $\Delta_e/2\pi = 100$ MHz, $\Delta = 0$ (three-levels). For comparison with the two-level scheme we use $\Omega/2\pi = 5.0$ MHz and $\Delta/2\pi = -79$ MHz, where Ω is the one-photon Rabi frequency and Δ the respective laser detuning. These parameters were chosen such that both systems

[1] For $\Delta_e \gg \Omega_e,\ \Omega_r,\ \Gamma_e$ the population of the intermediate state is very small. Then the description of the system can for example be simplified by adiabatically eliminating the intermediate state [227].

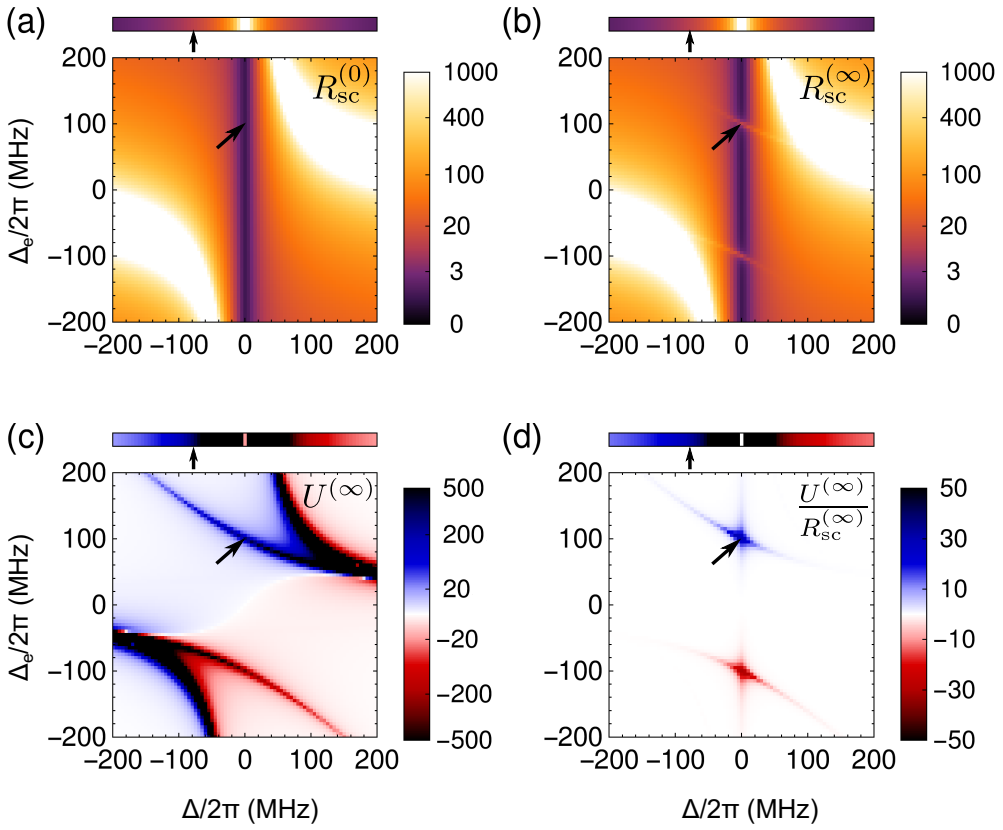

Figure 4.2: Dressed state decay rates and interaction strength as a function of the laser detunings. (a) Decay rate per atom $R_{sc}^{(0)}$ for $V \to 0$ corresponding to two independent particles. The bright stripes of maximum decay correspond to the Autler-Towns resonances. The dark stripe in between at two-photon resonance $\Delta = 0$ is the electromagnetically induced transparency (EIT) resonance of destructive interference. (b) Decay rate per atom $R_{sc}^{(\infty)}$ for $V \to \infty$ corresponding to the fully blockaded limit. The EIT-condition is broken at $\Delta_e \approx \pm\Omega_r/2$, indicating a cooperative enhancement of the Rydberg fraction. (c) Dressed state interaction strength $U^{(\infty)}$. Blue corresponds to repulsive and red to attractive interactions. Resonance lines appear as local extrema, corresponding to the Autler-Towns resonances and the cooperative resonances described in the main text. (d) Figure of merit $f = U^{(\infty)}/R_{sc}^{(\infty)}$. Extrema indicate good dressing conditions, with global extrema corresponding to the crossings between the EIT resonance and the cooperative resonances as described in the main text. The arrows indicate the detunings used in Figure 4.1. The three-level dressing regime of large detuning from all excited states appears in these plots for $|\Delta_e| \gg \Omega_r$ in the vicinity of the Autler-Towns resonances. The colourscales for figures (a-c) follow a powerlaw to emphasize small features whereas (d) is on a linear scale. The horizontal bars above each plot show the corresponding two-level parameters on the same colourscale as a function of the detuning Δ. Units of both $R_{sc}/2\pi$ and $U/2\pi$ are Hz in accordance with Figure 4.1. Figure reproduced from [226].

exhibit similarly small decay rates ($\lesssim 10$ Hz) and long-range effective interactions which "soften" to a constant value $U^{(\infty)}$ at short distances. We note however that the three-level dressed potential is considerably more box-like than for two-levels, and its range is shorter due to the larger excitation bandwidth resulting in a smaller blockade radius.

A distinguishing feature of three-level dressing is that the decay rate can be strongly spatially dependent, which is in contrast to the two-level case which only shows a small reduction of $R_{\rm sc}$ at short distances. We focus on two limits: $V = 0$ and $V \to \infty$. For large interparticle separations or dilute-gas experiments the residual decay rate $R_{\rm sc}^{(0)} = R_{\rm sc}(V = 0)$ is minimized due to destructive interference of the intermediate state population due to electromagnetically induced transparency (EIT). For short distances or in dense gases on the other hand the Rydberg blockade effect breaks the EIT condition leading to increased decay rates which plateau at a value $R_{\rm sc}^{(\infty)} = R_{\rm sc}(V \to \infty)$. This enhanced distance dependent decay may find applications in quantum state engineering via dissipation [229] or novel cooling techniques [169, 230, 231]. Another important difference between the three-level and two-level cases concerns the dependence on the sign of the bare-state interactions. In the two-level case the sign of V and Δ must be opposite to avoid level crossings which deform the potential and give rise to strongly enhanced decay (Fig. 4.1(c)). In contrast, the shape and sign of the potential in the three-level case can be made independent of the sign of V and can be manipulated by Δ_e.

While the two-level case has relatively few tuning parameters (Ω and Δ), the three-level case presents additional possibilities through independently tuning $\Omega_e, \Omega_r, \Delta_e$ and Δ. Therefore we search for optimal parameters which maximize $U^{(\infty)}$ while keeping $R_{\rm sc}$ small. To ensure a small Rydberg state population we exploit Autler-Townes splitting, focusing on the parameter regime $\Omega_r \gg \Gamma_e \gg \Gamma_r$ and $\Omega_r \gg \Omega_e$.[2] The qualitative features of $R_{\rm sc}$ and $U^{(\infty)}$ in this parameter regime are mostly independent of the Rabi frequencies which predominantly influence the overall energy and time scales. Figures 4.2(a,b) show the characteristic decay rates $R_{\rm sc}^{(0)}$, $R_{\rm sc}^{(\infty)}$ for the three-level system as a function of the intermediate- and two-photon detunings Δ_e and Δ respectively. The Autler-Townes doublet is clearly seen as bright bands for $\Delta_e = \Omega_r^2/(4\Delta)$ and the distinct minimum for $\Delta = 0$ is due to destructive interference of the intermediate state amplitude. In the interaction dominated regime we observe two additional features in $R_{\rm sc}^{(\infty)}$ for $\Delta_e = -(\Delta \pm \sqrt{\Delta^2 + \Omega_r^2})/2$ (Fig. 4.2(b)). These features correspond to cooperative resonances between the two-atom ground state and the $|e_1\rangle|e_2\rangle$, $|e_1\rangle|r_2\rangle$ and $|r_1\rangle|e_2\rangle$ states. This is a cooperative effect since the multiphoton multiatom excitations enhance the Rydberg fraction beyond the corresponding non-interacting single-atom value [225]. Approximate analytical relations for $U(V)$ and $R_{sc}(V)$ valid in this regime can be found in [228].

Figure 4.2(c) shows the interaction strength $U^{(\infty)}$ which is split into two domains of repulsive (blue) and attractive (red) interactions. Maximum interaction strengths are found on the Autler-Townes resonances (coinciding with maximal decay rates) and on the cooperative resonances (with small decay rates). This cooperative enhancement of the dressed-state interactions does not appear in an effective two-level description. A similar type of enhancement exploiting molecular resonances for specific pair distances and Rydberg states has recently been proposed [232], however the cooperative enhancement reported here works for any Rydberg state and preserves the soft-core nature of the dressed potential. We also expect it to persist for more than two atoms [225], therefore it may also prove beneficial for the implementation of collective many-body interactions in Rydberg dressing [138].

[2] The two Autler-Townes resoannces have a Lorentzian distribution with a small overlap at the two-photon EIT resonance condition $\Delta = 0$ for destructive interference.

	2-level	**optimized 3-level**
β^2	$\Omega^2/(2\Delta)^2$	Ω_e^2/Ω_r^2
$R_{\mathrm{sc}}^{(0)}$	$\Gamma_r\beta^2$	$2\Gamma_r\beta^2$
$R_{\mathrm{sc}}^{(\infty)}$	$-2\Gamma_r\beta^4 + R_{\mathrm{sc}}^{(0)}$	$\beta^4\Omega_r^2/\Gamma_e + R_{\mathrm{sc}}^{(0)}$
$U^{(\infty)}$	$-2\beta^3\Omega$	$\mathrm{sign}(\Delta_e)\beta^4\Omega_r^3/{\Gamma_e}^2$
$\lvert f\rvert$	$\frac{2\Omega}{\Gamma_r}\left[\beta^{-1} - 2\beta\right]^{-1}$	$\frac{\Omega_r}{\Gamma_e}\left[1 + \frac{2\Gamma_r\Gamma_e}{\beta^2\Omega_r^2}\right]^{-1}$

Table 4.1: Key parameters and approximate scaling relations characterising the dressed-state potential in the weak dressing regime: Rydberg fraction β^2, residual decay rates $R_{\mathrm{sc}}^{(\infty)}$ and $R_{\mathrm{sc}}^{(0)}$, interaction potential $U^{(\infty)}$ and the figure of merit $f = U^{(\infty)}/R_{\mathrm{sc}}^{(\infty)}$. We restrict our analysis to $\beta \ll 1$ and $\mathrm{sign}(V) \neq \mathrm{sign}(\Delta)$ (two-level case) and $\Delta = 0$ and $\Delta_e = \pm\Omega_r/2$ (optimized three-level case). Ω refers to the Rabi frequency of the direct one-photon transition.

4.4 Figure of merit for optimal Rydberg dressing

We search for dressing conditions characterised by large interaction strengths $U^{(\infty)}$ and small scattering rates. We combine these requirements into the figure of merit for Rydberg dressing

$$f = U^{(\infty)}/R_{\mathrm{sc}}^{(\infty)}. \tag{4.8}$$

Figure 4.2(d) shows our figure-of-merit as a function of the two detunings. The optimal detunings are clearly revealed as dark crosses at the intersection of the two-photon resonance line and the cooperative resonances at $(\Delta, \Delta_e) = (0, \pm\Omega_r/2)$ which coincides with the parameters chosen for Figure 4.1(b,c). Here, $U^{(\infty)}/2\pi \approx 0.3\,\mathrm{kHz}$ and $R_{\mathrm{sc}}^{(\infty)}/2\pi \approx 10\,\mathrm{Hz}$, leading to $f \approx 30$ for three-level dressing. This large figure of merit indicates that interactions are more pronounced than decay, allowing for strong dressed interactions at long excitation times.

We now discuss the scalings with system parameters of the interaction strength, decay rate and the figure of merit for three-level dressing with detunings corresponding to the two-photon resonance as well as the cooperative resonance. A summary of these relations is presented in Table 4.1. In the non-interacting limit the Rydberg fraction on two-photon resonance is $\beta^2 \approx \Omega_e^2/\Omega_r^2$ as expected for the EIT dark state [182]. Remarkably, the decay rate is independent of Γ_e and is given by $R_{\mathrm{sc}}^{(0)} \approx 2\Gamma_r\beta^2$. Both the interaction strength and the decay rate are maximal at the cooperative resonance with $\left|U_{\mathrm{opt}}^{(\infty)}\right| \approx \beta^4\Omega_r^3/\Gamma_e^2$ and $R_{\mathrm{sc}}^{(\infty)} \approx \beta^4\Omega_r^2/\Gamma_e + R_{\mathrm{sc}}^{(0)}$, which for small Γ_r is dominated by the first term. Comparing these two yields a figure of merit $|f| \approx \Omega_r/\Gamma_e$. This shows that the optimal condition for three-level dressing requires small intermediate-state decay rates and large couplings on the upper transition, but is independent of the Rydberg state admixture and the dressed state lifetime, which is free to be chosen through the ratio Ω_e^2/Ω_r^2. Corresponding expressions for the two-level system are provided in Table 4.1. By comparing the scalings of two- and three-level dressing for equal decay rates we conclude that the figure of merit for three-level

dressing may outperform two-level dressing if

$$f_{\text{opt 3lvl}} = \frac{\Omega_r}{\Gamma_e} > \frac{2\Omega}{\Gamma_r}\left(\frac{R_{\text{sc}}}{\Gamma_r}\right)^{\frac{1}{2}} = f_{\text{2lvl}}. \tag{4.9}$$

Conclusion

In conclusion, we have analyzed effective two-body interaction potentials and decay rates for Rydberg-dressed atoms coupled by multiple laser fields using a master-equation treatment. Although we primarily focused on two-level and three-level dressing schemes, this approach is also applicable to systems with more levels and more than two coupling fields. While two-level dressing (i.e. employing a single laser field coupling ground and Rydberg states) completely eliminates the population of short-lived states, which may be important for achieving long dressed-state lifetimes, we also find favorable conditions in the three-level system by making use of EIT interference on two-photon resonance. Recent experiments [119] and corresponding theorertical modeling [228] have investigated a similar idea for Rydberg dressing of strontium. Additionally, we have identified optimum laser parameters corresponding to a cooperative enhancement of the dressed state potential which is not present for the effective two-level descriptions considered previously. The achievable interaction strength shown in Figure 4.1(b) corresponds to an energy of $\approx k_B \times 15$ nK. This energy scale is within reach in ultracold quantum gases which should make it possible to observe the effects of long-range Rydberg dressed interactions in Bose-Einstein condensates and degenerate Fermi gases. The figure of merit for three-level dressing under these conditions scales with Ω_r/Γ_e, indicating that large coupling strengths between intermediate and Rydberg states and long lifetimes of the intermediate state are desirable. This highlights the importance of high power lasers and large matrix elements for the upper transition, combined with long intermediate state lifetimes, such as is possible using the $|ns\rangle \rightarrow |(n+1)p\rangle \rightarrow |r\rangle$ excitation scheme (with $|ns\rangle$ corresponding to the electronic ground state) in the alkali atoms [161]. However, the experimental challenge will be to isolate a three-level system without spuriously populating additional intermediate or Rydberg states. Other Rydberg states can potentially be populated by blackbody-driven transitions [98, 119] or via resonant two-atom excitation of Rydberg pair states at small distances $R < 1$ μm [112]. Interestingly, the sign of the three-level dressed state potential is independent of the sign of the bare Rydberg-Rydberg interactions, opening the possibility to study purely repulsive anisotropic interactions, thereby minimizing losses or dipolar relaxation [233]. Another interesting feature of three-level dressing is the possibility to introduce and control density dependent dissipation, which could be advantageous for studying, for example, non-equilibrium superfluidity in coupled quantum fluids of matter and light with strong and tuneable interactions [85].

Unravelling the phase structure of driven-dissipative Rydberg spin systems

5

This chapter is based on the following manuscript, from which parts of the text are reproduced verbatim with permission by the American Physical Society:

Uncovering the non-equilibrium phase structure of an open quantum spin system
S. Helmrich, A. Arias and S. Whitlock
submitted to Physical Review X

Statistical mechanics provides a powerful framework for understanding and classifying states of matter close to thermal equilibrium - a seminal example being the transition between paramagnetic and ferromagnetic phases of Ising magnets and the liquid-gas transition in fluids [54]. Close to their respective transition points, critical fluctuations with diverging correlations dominate, giving rise to remarkably simple scaling laws for macroscopic observables [200]. As it happens, in the case of the Ising transition and the liquid-gas transition, these scaling laws involve just a few common exponents, indicating that both systems infact belong to the same universality class.

Comparatively little is known about many-body systems in out-of-equilibrium scenarios [55], especially open quantum systems, governed by a competition between quantum coherent evolution and dissipation. This is becoming especially relevant with the emergence of a new generation of experiments that are genuinely non-equilibrium in nature. A selection of relevant experimental platforms and phenomena was presented in section 1.3. An important feature of these systems is the interplay between coherent driving, dissipation (e.g., due to spontaneous decay) and interactions between the particles, that can give rise to fundamentally new states and dynamical behaviour that are quite distinct from equilibrium matter. A selection of relevant non-equilibrium phenomena was introduced in section 1.2. Classifying these new states of matter poses a significant challenge to state-of-the-art many-body theory and experiments, in part because theoretical methods capable of dealing with open many-body systems are less developed and because it is difficult to devise observables capable of distinguishing the vastly different types of behaviour they can exhibit.

Here we experimentally investigate the long-time dynamics of a widely tunable open quantum spin system (Fig. 5.1) with well known microscopic processes governing the evolution of each spin. We show that the overall rate of population loss due to the decay of excited states provides a convenient macroscopic observable for the many-body state which can be measured with a dynamic range covering several orders of magnitude. We discover

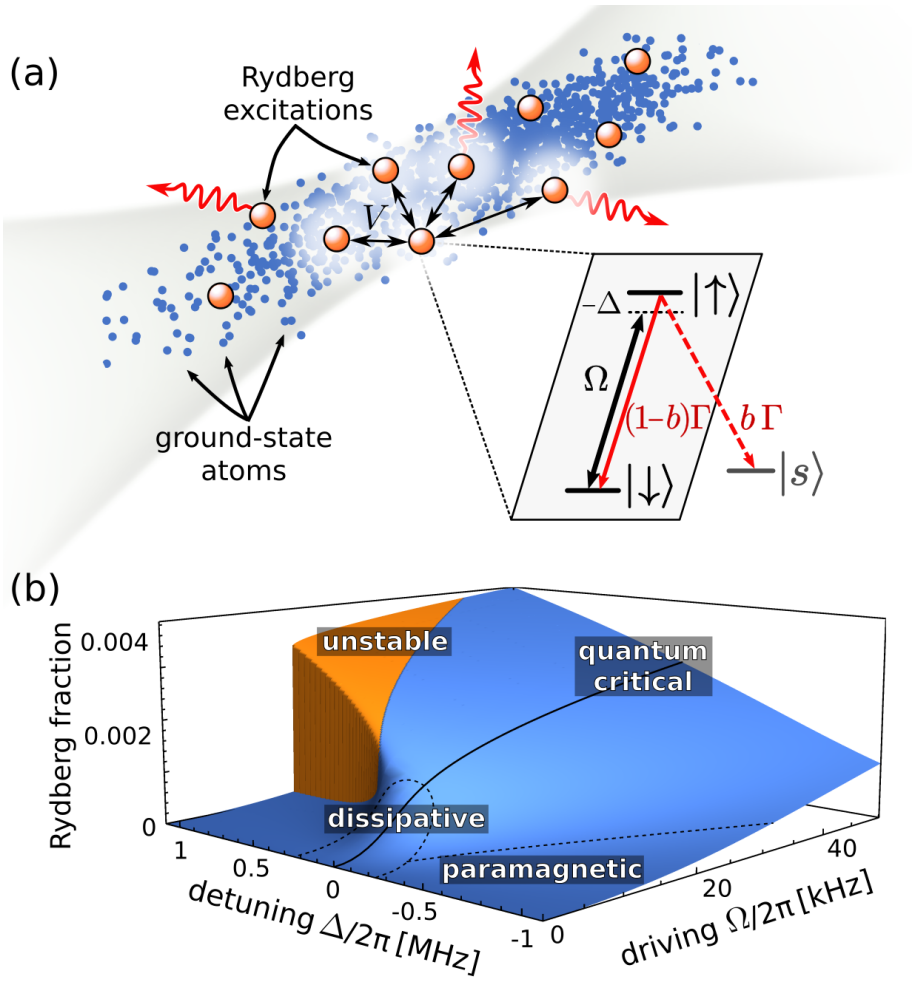

Figure 5.1: Prototypical open quantum spin system based on laser driven Rydberg atoms in an optical trap. (a) Geometry of the atomic gas (blue dots) with Rydberg excited atoms depicted as orange spheres. The ground and Rydberg states of each atom form a pseudo-spin 1/2, where the laser coupling (Ω) and detuning (Δ) play the role of transverse and longitudinal fields. Ising-like interactions arise from the repulsive van der Waals interactions between Rydberg states, while dissipation arises via decay of the excited state, which returns population either to the $|\downarrow\rangle$ state or with branching factor b out of the system to auxilliary shelving states represented by $|s\rangle$. (b) Non-equilibrium phase diagram obtained from mean-field theory showing the steady state fraction of Rydberg excitations m (assuming $b = 0$ and otherwise similar parameters to the experiment). The competition between driving, dissipation and interactions gives rise to a rich phase structure, including paramagnetic, dissipation dominated, critical and unstable regimes. Reproduced from [234].

that this observable exhibits approximate powerlaw scaling over a wide parameter range, with exponents that we associate to qualitatively different regimes. Our observations are in good agreement with theoretical modelling of the open-system dynamics based on coupled rate-equation simulations that include the effects of strong and long-range interactions between Rydberg excited atoms. Combining theory and experiment, we map out the non-equilibrium phase diagram of this system which exhibits four distinct regimes including dissipation-dominated and paramagnetic regimes as well as two distinct many-body regimes

which arise through the competition between interactions and driving.

5.1 Quantum description of the open spin system

Our system consists of a gas of ultracold atoms driven by a laser field to create a small fraction of short-lived Rydberg excitations (Fig. 5.1(a)). We again use the quantum master equation in Lindblad form for the many-body density matrix $\hat{\rho}$ to describe our system, which was introduced in section 3.1. It is given by ($\hbar = 1$)

$$\partial_t \hat{\rho} = -i[\mathcal{H}, \hat{\rho}] + \mathcal{L} + \mathcal{L}^{\mathrm{de}}. \tag{5.1}$$

In this equation, the Hamiltonian $\mathcal{H}$ accounts for the coherent part of the dynamics, while the Lindblad operators account for dissipative processes. In the following we assume that the excitation laser couples the ground and Rydberg states, which are identified as the spin-down and spin-up states of a pseudo-spin 1/2, respectively. Then the Hamiltonian reads

$$\mathcal{H} = \frac{\Omega}{2} \sum_j \sigma_x^{(j)} - \frac{\Delta}{2} \sum_j \sigma_z^{(j)} + \frac{1}{2} \sum_{j,k \neq j} V_{jk} n^{(j)} n^{(k)}, \tag{5.2}$$

where $\sigma_x^{(j)}$, $\sigma_z^{(j)}$ are Pauli spin matrices and $n^{(j)} = (\sigma_z^{(j)} + 1)/2$ projects onto Rydberg states.

In our experiment antiferromagnetic spin-spin interactions originate from the repulsive van der Waals interactions between Rydberg excitations. These interactions fall off as a powerlaw $V_{jk} = C_6/|\vec{r}_j - \vec{r}_k|^6$ but due to the extremely large C_6 coefficients of Rydberg states they can extend far beyond nearest-neighbors. This has the consequence that a single excitation can suppress the subsequent excitation of hundreds of nearby spins within a characteristic volume called the Rydberg blockade volume (cf. sec. 3.3.1). A convenient parameter which characterises the van der Waals interactions between neighbouring Rydberg states is $J = C_6 {n_0}^2$ where n_0 is the peak atomic density. The atom-light coupling strength Ω and the detuning from the atomic transition Δ correspond to transverse and longitudinal fields respectively, which can be tuned over a wide range via the Rydberg excitation laser.

Dissipation processes in our system originate from decay of excited states and single-spin dephasing (cf. sec. 3.2.4). We represent decay with rate Γ by the local Lindblad operator

$$\mathcal{L}(\hat{\rho}) = \sum_j \left[(1-b) L_j \hat{\rho} L_j^\dagger - \frac{L_j^\dagger L_j \hat{\rho} + \hat{\rho} L_j^\dagger L_j}{2} \right] \qquad \text{with jump operator } L_j = \sqrt{\Gamma}\, |{\downarrow_j}\rangle \langle{\uparrow_j}| \tag{5.3}$$

and single spin dephasing, e.g. to account for laser phase noise, by

$$\mathcal{L}^{\mathrm{de}}(\hat{\rho}) = \sum_j \left[L_j^{\mathrm{de}} \hat{\rho} L_j^{\mathrm{de}\dagger} - \frac{L_j^{\mathrm{de}\dagger} L_j^{\mathrm{de}} \hat{\rho} + \hat{\rho} L_j^{\mathrm{de}\dagger} L_j^{\mathrm{de}}}{2} \right] \qquad \text{with } L_j^{\mathrm{de}} = \sqrt{\gamma_{\mathrm{de}}}\, |{\uparrow_j}\rangle \langle{\uparrow_j}|\,. \tag{5.4}$$

In the Lindblad operator for decay we have explicitly taken particle dissipation with rate $b\Gamma$ into account, which arises from decay to shelving states $|s\rangle$ external to the laser coupling.

Neglecting dissipation for a moment, this system closely resembles the quantum Ising model in transverse and longitudinal fields [197, 199, 190] as discussed in section 3.3.2. The

equilibrium quantum phase diagram is characterised by the Rydberg fraction $m = \langle n^{(j)} \rangle$ of the many-body system, which plays the role of the magnetisation.[1] Thus, in the limit $\Omega \to 0$ the resulting equilibrium quantum ground state phase diagram includes a paramagnetic phase (for $\Delta < 0$) and a hierarchy of crystalline phases (for $\Delta > 0$) with varying excitation densities [199]. Increasing the coherent laser coupling $\Omega > 0$ introduces quantum fluctuations which lead to the appearance of an experimentally accessible quantum critical region [235, 201]. However, the inclusion of spontaneous decay of the Rydberg states breaks the detailed-balance condition of equilibrium physics, which can have dramatic effects on the many-body state characterised by the Rydberg fraction and on the corresponding phase structure.

To help navigate the non-equilibrium phase structure, we present mean-field results for the non-equilibrium Rydberg fraction m in steady state and without particle loss ($b = 0$) in Figure 5.1(b). Mean-field theory provides a relatively simple way to qualitatively understand the different phases of the driven-dissipative system by providing analytic expressions for the magnetisation and corresponding scaling laws. We introduced our mean field model of the driven-dissipative system in section 3.4.1, where we assumed a product state ansatz and a homogeneous system, but explicitly included a hardcore constraint for the two-point correlations which captures the Rydberg blockade effect. We found (eq. (3.22)) that the mean field Rydberg fraction is described by

$$\Omega^2 \approx \left(4\big(\Delta - Jc\, m^{p/d}\big)^2 + (\Gamma + \gamma_{\mathrm{de}})^2\right) \frac{m\Gamma}{\Gamma + \gamma_{\mathrm{de}}}, \tag{5.5}$$

for which we show a numerical solution in Figure 5.1(b). Except for the orange region in this figure, the system has a unique steady state corresponding to a small and smoothly varying fraction of Rydberg excitations. From further inspection of the mean-field solution we can identify four different regimes depending on the dominant energy scales:

Paramagnetic regime ($|\Delta| \gg Jc\, m^{p/d},\ \Gamma + \gamma_{\mathrm{de}}$): For detunings far above or below resonance and for weak interactions and dissipation, each spin aligns with the external field according to the relative strength of Ω and Δ. For large detunings the Ising interaction term can be considered a small perturbation yielding a paramagnetic state with magnetisation

$$m = \left(\frac{\Omega}{2\Delta}\right)^2 \frac{\Gamma + \gamma_{\mathrm{de}}}{\Gamma}. \tag{5.6}$$

This is equivalent to each atom being in the weakly-dressed state $|\psi\rangle \approx |{\downarrow}\rangle + \beta\,|{\uparrow}\rangle$ with $\beta = \Omega/(2\Delta) \ll 1$.

Dissipation-dominated regime ($\Delta \approx 0;\ \Gamma + \gamma_{\mathrm{de}} \gg Jc\, m^{p/d}$): Driving the system close to resonance, if the single-spin spontaneous decay (or dephasing) rate is large compared to the driving strength Ω, then this results in a continuous projective measurement of each spin in the σ_z basis. Consequently, the system will evolve to a classical spin configuration comprised of a small but fluctuating number of spin-up excitations. In this limit the steady state Rydberg fraction scales as

$$m = \frac{\Omega^2}{\Gamma(\Gamma + \gamma_{\mathrm{de}})}. \tag{5.7}$$

[1] Here, the expectation value includes averaging over individual atoms.

Critical regime ($\Delta \approx 0$; $Jc\, m^{p/d} \gg \Gamma + \gamma_{\mathrm{de}}$): Also close to resonance, as the driving field strength is increased, the system undergoes a crossover from the dissipation-dominated regime to a high-density liquid-like state. This coincides with a change in the Ω dependence of the magnetisation that originates from the critical regime associated to the quantum critical point of the equilibrium Ising-like model at $\Delta = \Omega = 0$.[2]

$$m = \left(\frac{\Omega}{2Jc} \sqrt{\frac{\Gamma + \gamma_{\mathrm{de}}}{\Gamma}} \right)^{1/\delta} \quad \text{with} \quad \delta = \frac{p}{d} + \frac{1}{2}. \tag{5.8}$$

Thus the mean-field magnetisation scales as $\Omega^{1/\delta}$ in the critical regime. For our system $p = 6$ and $d = 3$, resulting in a mean field scaling exponent of $2/5$, which is one of the universal critical exponents of the model [197].

Unstable regime ($|\Delta - Jc\, m^{p/d}| \gg \Gamma + \gamma_{\mathrm{de}}$): The competition between dissipation, driving and interactions is perhaps most striking for intermediate detunings above resonance (i.e. the orange region of Fig. 5.1(b) for $\Delta > 0$), the magnetisation takes on multiple solutions with low and high Rydberg fraction, according to

$$\Omega = 2\sqrt{m} \left| \Delta - Jc\, m^{p/d} \right| \sqrt{\frac{\Gamma}{\Gamma + \gamma_{\mathrm{de}}}}. \tag{5.9}$$

It is debated whether such bistabilities due to Rydberg-Rydberg interactions can be observed in experiments [125, 128, 129, 126], while theoretical studies of similar models taking into account beyond-mean-field corrections suggest that the bistable phase may be replaced by a first order transition and a tricritical point [236, 237].

Transition from critical to dissipation dominated regimes: From the above formulas, expressions for the boundaries between the regimes can also be derived. As an example, we will discuss the threshold between driving and dissipation dominated regimes found by equating eq. (5.7) and eq. (5.8):

$$\Omega_{\mathrm{th}} = \sqrt{\Gamma(\Gamma + \gamma_{\mathrm{de}})} \left(\frac{\Gamma + \gamma_{\mathrm{de}}}{2Jc} \right)^{d/2p} \tag{5.10}$$

The last factor in the equation above can be expressed in terms of the d-dimensional blockade volume $\mathcal{V}_{\mathrm{bl}} = \mathcal{V}_d (\frac{2C_p}{\Gamma + \gamma_{\mathrm{de}}})^{d/p}$ containing $N = n_0 \mathcal{V}_{\mathrm{bl}}$ atoms [96]. Thus we find for the crossover position:

$$\sqrt{N}\Omega_{\mathrm{th}} = \sqrt{\frac{\Gamma(\Gamma + \gamma_{\mathrm{de}})}{(p/d - 1)^{d/p}}} \tag{5.11}$$

5.2 Experimental platform with two-photon excitation

In the following we will experimentally explore this rich non-equilibrium phase structure. For a detailed description of the setup and the preparation of the ultracold atom cloud we refer to chapter 2. Here we will only summarise the specific parameters relevant for the experiments discussed in this chapter. We perform experiments on a gas of $7.5 \cdot 10^4$ ^{39}K atoms initially

[2] We introduced the notion of a critical point in section 1.2.1 and the equilibrium phase diagram of the Rydberg spin system in section 3.3.2.

prepared in the $|\downarrow\rangle = |4s_{1/2}, F = 2, m_F = 2\rangle$ state and randomly distributed in a cigar shaped optical dipole trap. The peak atomic density and temperature are $n_0 = 5 \cdot 10^{11}\,\mathrm{cm}^{-3}$ and $T = 19.4\,\mu\mathrm{K}$ respectively. All atoms in the sample are then driven from $|\downarrow\rangle$ to $|\uparrow\rangle = |66s\rangle$ by a two-photon laser excitation with large detuning from the intermediate state such that it can be mostly neglected. As described in detail in section 2.3, this excitation scheme utilises a weak 'probe' laser at 767 nm wavelength for the lower $|\downarrow\rangle \leftrightarrow |e\rangle = |4p_{3/2}\rangle$ transition and a strong 'coupling' laser at 456 nm wavelength for the upper $|e\rangle \leftrightarrow |\uparrow\rangle$ transition. The atomic cloud has $e^{-1/2}$ radii $\{\sigma_r, \sigma_z\} = \{7\,\mu\mathrm{m}, 220\,\mu\mathrm{m}\}$ assuming a normal distribution. The probe laser is aligned perpendicularly to the long axis with a waist of $\approx 10\,\mathrm{mm}$. It homogeneously illuminates the cloud with tunable driving strength $\Omega_p/2\pi \lesssim 1.2\,\mathrm{MHz}$ and detunings from the $|e\rangle$ state in the range $\Delta_p/2\pi = (80 \pm 20)\,\mathrm{MHz}$. The coupling laser is derived from a frequency doubled Ti:Sa laser with a total power of 1.15 W focused to a waist of approximately 30 µm and is aligned collinearly with the long axis of the atom cloud for maximum homogeneity. In our measurements we keep the driving strength and detuning of the coupling laser fixed to the values $\Omega_c/2\pi \approx 20\,\mathrm{MHz}$, $\Delta_c/2\pi = -77\,\mathrm{MHz}$ and tune Ω_p and Δ_p. The combined linewidth of both lasers is $\lesssim 200\,\mathrm{kHz}$.

The three-level system can be reduced to an effective two-level system (with driving parameters Ω, Δ) in the limit that the population in $|e\rangle$ is negligibly small, e.g. in the limit $|\Delta_p| \approx |\Delta_c| \gg \Omega_c \gg \Omega_p,\ \Gamma_e$. For $\Delta_p \approx -\Delta_c$ we can describe the coupling from $|\downarrow\rangle \leftrightarrow |\uparrow\rangle$ by an effective two-photon driving strength $\Omega \approx \varepsilon\Omega_p$, where $\varepsilon = \Omega_c/(2|\Delta_c|) \ll 1$, and an effective detuning $\Delta = \Delta_p + \Delta_c + \Delta_{\mathrm{ODT}}$, where $\Delta_{\mathrm{ODT}}/2\pi = 4\,\mathrm{MHz}$ accounts for the additional light shifts from the 1064 nm optical dipole trap laser. The position of maximum loss is additionally shifted by 0.5 MHz due to the light shift produced by the coupling laser and averaging over the inhomogeneous optical dipole potential. The effective excited state decay rate $\Gamma/2\pi \approx (\Gamma_r + \varepsilon^2\Gamma_e)/2\pi \approx 100\,\mathrm{kHz}$ is a combination of the bare Rydberg state decay $\Gamma_r/2\pi \approx 1.2\,\mathrm{kHz}$ (including blackbody transitions) [181] and the residual intermediate state admixture which spontaneously decays with rate $\Gamma_e/2\pi = 6.03\,\mathrm{MHz}$. Additional loss processes for ns-Rydberg states, e.g., photoionisation or penning ionisation are estimated to be below 1 kHz [166, 167] and can be neglected.

Our measurements are performed by varying the probe laser intensity over the range from $30\,\mathrm{nW/cm^2}$ to $30\,\mu\mathrm{W/cm^2}$, which corresponds to $\Omega/2\pi$ from 3 kHz to 100 kHz. The corresponding atom-light interaction time τ is set by pulsing an acousto-optical modulator for the probe laser while the coupling laser is kept on continuously. The strength of the nearest neighbour van der Waals interactions of Rydberg pair states is $J/2\pi = 65.4\,\mathrm{GHz}$ (for a calculated van der Waals interaction strength $C_6/2\pi = 270\,\mathrm{GHz}\,\mu\mathrm{m}^6$ [174]), greatly exceeding all other energy scales such as those associated to single particle driving and decoherence, leading to strong blockade effects. The total effective decay rate of the excited states, including spontaneous emission and black body decay from the Rydberg and short-lived intermediate states, is $\Gamma/2\pi \approx 100\,\mathrm{kHz}$. This brings the atom either back to the original ground state $|\downarrow\rangle$ or to auxiliary shelving states $|s\rangle$ external to the spin-1/2 description, such as the $|4s_{1/2}, F = 1\rangle$ state, with an estimated probability $b = 0.18$ (cf. sec. 5.5). This ultimately leads to all the population accumulating in $|s\rangle$. However, interesting quasi-steady states can be reached for significant periods of time even when $b \neq 0$.

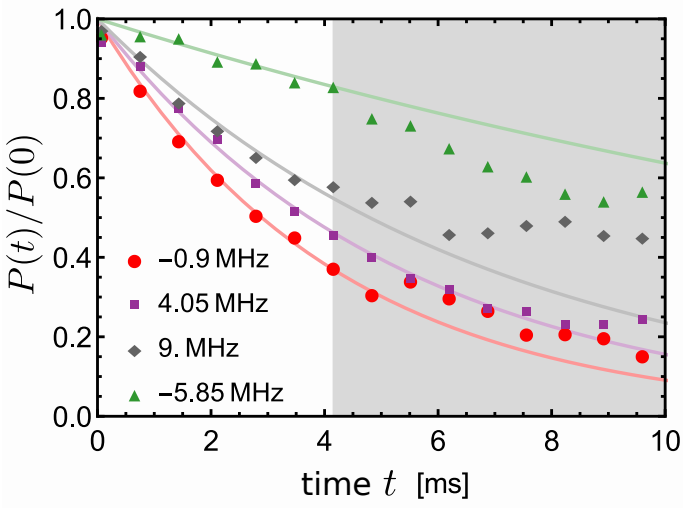

Figure 5.2: Time resolved measurements of the fraction of atoms remaining in the ground state after an excitation pulse of varying duration. Data for a fixed driving strength of $\Omega/2\pi = 22\,\mathrm{kHz}$ and four different detunings are shown. The boundary between white and grey backgrounds marks the waiting time $\tau = 4.1\,\mathrm{ms}$ used in all experiments for this value of Ω. Reproduced from [234]

5.3 Probing the open system dynamics

To probe the open system dynamics we take advantage of the slow loss of population out of the spin-1/2 subspace and measure the remaining fraction of atoms $P(\tau)$ after an evolution time τ. Starting with all atoms initially prepared in the ground state, i.e. the fully magnetised state with $m = 0$, we suddenly switch on the driving field with fixed values of Ω and Δ corresponding to different regions of the non-equilibrium phase diagram (Fig. 5.1(b)). Following this quench, the system evolves towards excited many-body states on a timescale set by the inverse dissipation rate $(\Gamma + \gamma_{\mathrm{de}})^{-1}$. To probe the non-equilibrium behaviour of the system we let the system evolve for a time τ that is orders of magnitude longer. We then switch off the driving field and use absorption imaging to measure the remaining number of ground state atoms $P(\tau)/P(0)$.

Measuring the population decay in the experiment, we find that the temporal evolution of the remaining fraction of atoms is well described by a pure exponential decay if the resonant loss fraction of atoms satisfies $P(\tau)/P(0) \lesssim 0.5$. In Figure 5.2 we present time resolved data of the population loss for $\Omega/2\pi = 22\,\mathrm{kHz}$ and four different detunings spanning the different regimes of behaviour observed in the following. According to our measurement protocol, the waiting time τ used to extract R for this value of Ω was set to 4.1 ms (boundary between white and grey shaded regions). The data in the region $t < \tau$ is very well described by exponential decay curves, confirming that the formula $R = -\tau^{-1} \ln[P(\tau)/P(0)]$ can be used as a good estimator for the loss rate.[3] For different values of Ω (not shown here) we find similar exponential behaviour. This observation is consistent with the quasi-steady state magnetisation being constant and particle loss being a small correction to the internal state dynamics during the exponential decay. Then the loss rate is given by $R \approx b\Gamma m$.

[3] The deviations from pure exponential decay observed for later times will be discussed in the following chapter.

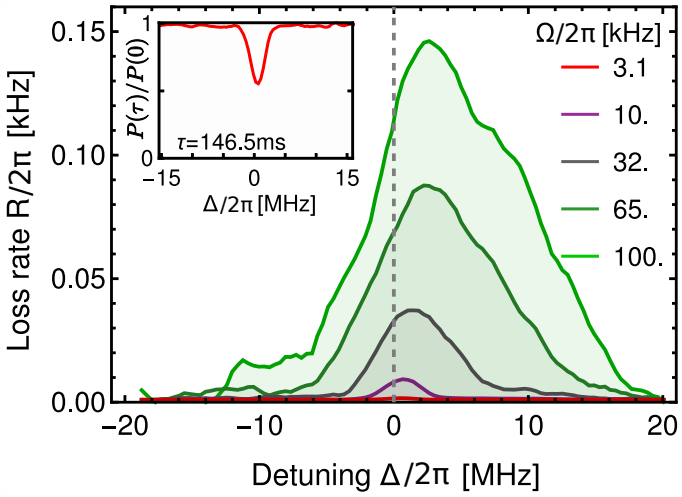

Figure 5.3: Measured loss rates as a function of detuning Δ for various driving field strengths Ω. As Ω is increased the spectra become asymmetric and broaden due to strong and repulsive Rydberg-Rydberg interactions. Inset: Fraction of atoms $P(\tau)/P(0)$ remaining in $|\downarrow\rangle$ for the smallest driving field strength $\Omega/2\pi = 3.1\,\mathrm{kHz}$. Reproduced from [234].

This implies that the internal dynamics establishes a quasi steady state on timescales much faster than the population loss, with the effect of particle loss on the quasi steady state magnetisation m being small.

In the following we will turn the slow particle loss into a tool to investigate the many-body state of our system as a function of driving strength Ω and detuning Δ. For each value of Ω we measure the remaining number of ground state atoms $P(\tau)$ and adapt the evolution time τ to limit the maximum lost fraction to $\lesssim 0.5$ on resonance. The choice of 50% loss on resonance maximises the signal to noise ration of our measurements. This is then converted to a rate by assuming exponential decay $R = -\tau^{-1}\ln[P(\tau)/P(0)]$ as observed previously. Depending on Ω, we cover evolution times between 1.4 ms and 146.5 ms, making it possible to measure R with a dynamic range of over four orders of magnitude in our experiments.

To verify that the loss rate is indeed sensitive to the state of the system, we measure its dependence on the driving strength and detuning (Fig. 5.3). For the smallest Ω we observe an approximately symmetric Gaussian lineshape with a full width half maximum of 3 MHz (Fig. 5.3(inset)). This is an order of magnitude broader than the estimated dephasing rate, but is consistent with single-atom master equation calculations including the inhomogeneous light shifts produced by the dipole trap laser (see sec. 5.5). This agreement is expected, as for small driving amplitudes the density of Rydberg excitations remains small enough that the gas is effectively non-interacting. As Ω is increased however, the width of the loss resonance grows and becomes noticeably asymmetric towards positive detunings, which is a clear consequence of the strong repulsive interparticle interactions between Rydberg ns states. This is compatible with previous experiments which directly measured the Rydberg excitation fraction and observed asymmetric broadening for short excitation pulses [121, 117]. Our maximal observed particle loss rate of 0.15 kHz is well below the non-interacting saturated limit $(\Gamma/2\pi)b/2 = 9\,\mathrm{kHz}$ which is another indication that interactions strongly influence the loss dynamics.

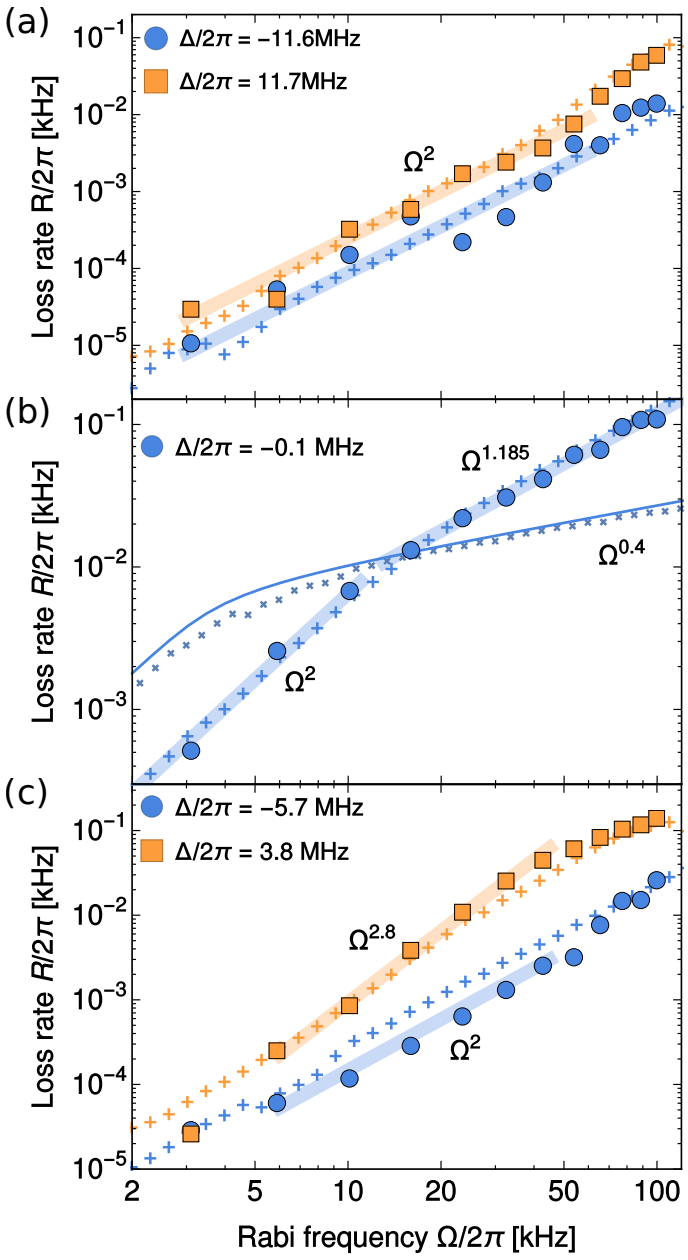

Figure 5.4: Powerlaw scaling of the loss rate R as a function of driving strength with different exponents that depend on the different regimes of the driven system. The thick shaded lines show the powerlaw scaling with exponents used to distinguish the different regimes discussed in the text. Rate equation simulation results are shown with + symbols. In panel (b) we additionally show homogeneous results for the rate equation simulations (crosses) and for mean-field theory (thin solid line). (a) Far from resonance the loss rate exhibits paramagnetic scaling with $\alpha = 2$. (b) Close to resonance the loss rate exhibits two different scaling regimes with $\alpha = 2$ (dissipation-dominated) and $\alpha = 1.185$ (critical). (c) For intermediate detunings we observe $\alpha > 2$ attributed to facilitated excitation that tends to drive the system into the critical regime with $\alpha < 2$ for large Ω. Reproduced from [234].

5.4 Non-equilibrium scaling laws

To exploit the high dynamic range of the loss measurements we now analyse the data for fixed detunings as a function of Ω as shown in Figure 5.4. Generally, the data can be empirically described by multiple powerlaws $R \propto \Omega^{\alpha}$, each spanning one or more orders of magnitude in R and Ω (shaded lines). The exponents change depending on the detuning and the range of driving field strengths. In the remainder of this chapter we show that these powerlaws and the boundaries in-between can be used to experimentally distinguish qualitatively different regimes of the driven-dissipative system anticipated from Figure 5.1(b).

For detunings far above or below resonance and for weak driving, the data exhibits powerlaw scaling with $\alpha \approx 2$ over most of the measurement range (Fig. 5.4(a)). This is consistent with paramagnetic behaviour expected from mean-field theory.

Driving the system close to resonance (Fig. 5.4(b), when going from small to large Ω we observe a transition from $\alpha \approx 2$ to a weaker exponent ($\alpha < 2$). The best fit exponent for large Ω has a mean of $\alpha = 1.185$ and standard deviation of 0.025 for detunings in the range $\pm 1\,\mathrm{MHz}$. The threshold between these two scaling behaviours, determined from a piecewise powerlaw fit, occurs around $\Omega_{\mathrm{th}}/2\pi \approx 12\,\mathrm{kHz}$. While the precise value of the scaling exponent differs from the mean-field expectation for the critical regime $\alpha_{\mathrm{MF}} = 2/5$, the change in scaling behaviour is similar to the crossover from the dissipation dominated to the critical regime associated to the quantum critical point at $\Delta = \Omega = 0$.

For intermediate detunings above resonance (Fig. 5.4), we observe a continuous increase of the loss rate with driving strength which appears to obey a powerlaw with stronger scaling ($\alpha > 2$) compared to all other regimes (Fig. 5.4(c)). This is highly suggestive of the effect of an instability driven by fluctuations (in the sense of a continuous phase transition) as opposed to the bistable phase predicted by mean-field theory. To test if the data is indeed well described by a powerlaw scaling we compare fits to both powerlaw and exponential growth models. For the data shown in Figure 5.4(c) we obtain $\alpha = 2.81(9)$ with a reduced $\chi^2 = 0.63$ for the powerlaw model which is favored over the exponential model with $\chi^2 = 11.3$. Power-law scaling with exponents $\alpha = 2.8 \pm 0.4$ is observed over a wide range of detunings above resonance ($\Delta/2\pi \approx (7 \pm 3)\,\mathrm{MHz}$) as well as a smaller range below resonance ($\Delta/2\pi \approx (-3.5 \pm 1.5)\,\mathrm{MHz}$).

A microscopic mechanism that can explain the stronger scaling above resonance is facilitated excitation (cf. sec. 3.3.1) [121, 117, 123, 118, 93]. In our data this is very pronounced above resonance, but is also seen slightly below resonance, most likely due to the inhomogeneous light shifts of the optical dipole trap or slight anisotropies of the interaction potential at short interatomic distances. This effect corresponds to broadening of the spectrum below resonance, for which similar features were for example discussed in [98, 238, 239]. was also observed Earlier experimental studies under similar experimental conditions have observed these facilitated excitation processes through super-Poissonian number fluctuations and temporal dynamics [121, 117, 118]. Powerlaw scaling is a newly observed feature of this dynamics.

For the largest driving strengths reached $\Omega/2\pi \gtrsim 50\,\mathrm{kHz}$ we observe another crossover to weaker scaling ($\alpha < 2$) which is connected to the same critical regime observed on resonance (as can be more clearly seen in Figure 5.5(b). This crossover appears for driving fields and detunings outside the window associated to the critical regime in Fig. 5.1(b), indicating that runaway facilitation processes tend to drive the system to criticality over

a wider parameter range than predicted by mean-field theory (seen by the dotted line in Figure 5.5(b)).

5.5 Coupled rate-equation modelling

To quantitatively describe the experiment and further elucidate the origin of the different scaling behaviours we go beyond mean-field theory, turning to numerical rate equation (RE) simulations. The basic idea of the RE approach is to describe the excitation dynamics in terms of stochastic jumps between classical spin configurations approximated by single-spin transition probabilities. RE models enable efficient simulation of the steady-state and dynamics of large systems comparable to those realized in experiment and have proven very successful in reproducing the behaviour of driven-dissipative Rydberg systems in the presence of dephasing [213, 132, 121, 240, 93].

Although atomic motion cannot be fully neglected in our experiments, for simplicity we start with a quasi-static model where each atom is treated with a fixed position and consists of the ground and Rydberg states only. As was shown in section 5.3, our experiments probe time scales where the internal state dynamics has reached a non-equilibrium quasi steady state approximately unperturbed by particle loss. For our simulations we focus on this quasi steady state and set $b = 0$. We also include single atom dephasing with rate $\gamma_{\mathrm{de}}/2\pi \approx 300\,\mathrm{kHz}$, compatible with the combined effects of laser linewidth and residual Doppler broadening in our experiment. By eliminating off-diagonal elements (coherences) of the quantum master equation (5.1) [94] as discussed in section 3.4, we obtain the single spin jump rates $\Gamma_{\uparrow,\downarrow}$ that have the form

$$\Gamma_{\uparrow}^{j} = \frac{\Omega^2(\Gamma + \gamma_{\mathrm{de}})}{(\Gamma + \gamma_{\mathrm{de}})^2 + 4(\Delta - V_j)^2}, \quad \Gamma_{\downarrow}^{j} = \Gamma_{\uparrow}^{j} + \Gamma, \tag{5.12}$$

where $V_j = \sum_k V_{jk}\rho_{\uparrow\uparrow}^{(k)}$ accounts for van der Waals interactions on atom j depending on the instantaneous configuration of all other spins. We approximate the slow loss out of the two-level subspace by evolving the classical rate equations from the fully magnetised state until the average fraction of Rydberg excitations has converged to its asymptotic value. This is then multiplied by the experimentally found $b\Gamma$ to recover the loss rate R.

Before performing RE simulations for the full many-body system we calibrate the model against the low intensity loss rate data shown in Figure 5.3(inset). For this we take the analytic solution for the single-atom steady state Rydberg population multiplied by a factor $b\Gamma$. However, the experimental spectrum is significantly broadened because of inhomogeneous level shifts mainly originating from the optical dipole trap laser. Therefore, we convolve the simulated spectra by the energy distribution of atoms in the trap, parameterized by the ratio of the cloud radius to the waist of the optical dipole trap σ/w. We fix the dephasing rate (accounting for the combined effect of laser linewidth and motional dephasing) to $\gamma_{\mathrm{de}}/2\pi = 300\,\mathrm{kHz}$ and adjust the unknown parameters $b = 0.18$, $\Delta_{\mathrm{ODT}}/2\pi = 4.0\,\mathrm{MHz}$ and $\sigma/w = 0.30$ to obtain best agreement with the data within the known experimental constraints. Careful inspection of the experimental loss rate data additionally reveals an unexpected broad pedestal centred around $\Delta/2\pi \approx 2.1\,\mathrm{MHz}$ with a standard deviation of $8.7\,\mathrm{MHz}$ but with an amplitude one order of magnitude smaller than the peak loss rate. We include this pedestal into the RE model as an additional single atom excitation process.

To quantitatively describe the data shown in Figures 5.3,5.4, we found it necessary to modify the static RE model to include the effect of thermal atomic motion, which enhances the excitation probability for $\Delta > 0$ due to the possibility for Landau-Zener transitions. This can be incorporated in the RE model by adding a second term to $\Gamma_\uparrow$ in equation (5.12) accounting for the velocity dependent Landau-Zener transition probability and the Maxwell-Boltzmann velocity distribution as well as the finite lifetime of the Rydberg state (see Appendix A). Without this term, the RE simulations were unable to reproduce stronger scaling observed above resonance within the experimentally accessible range of driving strengths. Finally, we account for the optical trap by averaging the simulated loss rates over the distribution of local detunings and atomic densities assuming Gaussian profiles for the trap laser and atomic cloud (see sec. 5.2).

Results of the RE simulations are presented alongside the experimental data in Figure 5.4. The RE model reproduces the key features of the experimental data over essentially the full range of parameters explored. For example, close to resonance (Figure 5.4(b)) the RE model clearly shows the change in scaling around Ω_{th}, transitioning from $\alpha = 2$ to a weaker scaling close to the experimental value of $\alpha = 1.185$. The RE model however does not appear to exhibit quite as sharp a transition as in the experiment. To investigate further, we also present mean-field and RE simulation results for a homogeneous system focusing on a region close to the centre of the trap where effects due to averaging over the inhomogeneous distribution of local atom density and trap lightshifts can be neglected (dotted line and crosses in Figure 5.4(b) respectively). Here the powerlaw scaling is even more pronounced with an exponent $\alpha = 0.4$, in agreement with the mean-field quantum critical exponent in three dimensions. Thus we can attribute the deviation compared to the experimentally measured scaling exponent to averaging over the inhomogeneous trap volume. It may be surprising at first that the RE model, which neglects quantum coherences, can reproduce this scaling behaviour. We attribute this to the fact that we concentrate on a relatively simple observable (the global magnetisation) in the long time limit after which any observable effects of coherent dynamics are effectively washed out. Based on this agreement between mean-field theory and the RE simulations as well as between the RE simulations and the experiment, we confirm that the change in scaling occuring around Ω_{th} is a consequence of the transition from dissipative to critical behaviour linked to the equilibrium critical point of the Ising-like model.

Interestingly, the crossover found in experiment and theory occurs for driving strengths significantly below the dissipation rate, which in mean-field theory is set by $\sqrt{\Gamma(\Gamma + \gamma_{\mathrm{de}})}$. This can be understood as a collective effect arising from the Rydberg blockade, similar to the crossover from weak-coupling to collective strong-coupling regimes of cavity quantum electrodynamics [241, 90]. Assuming the crossover occurs at the point where the collectively enhanced driving strength exceeds the total dissipation rate $\sqrt{N}\Omega_{\mathrm{th}} \approx \sqrt{\Gamma(\Gamma + \gamma_{\mathrm{de}})}$ we estimate the number of participating atoms to be around $N \approx 300$. This is quite small compared to an independent estimate of the peak number of atoms per Rydberg blockade volume $N \approx (4\pi/3)[2J/(\Gamma + \gamma_{\mathrm{de}})]^{1/2} = 2400$ based on the three-dimensional blockade volume [96]. This indicates that the relatively low density wings of the atomic cloud play a dominant role in determining the loss rate. It also shows the importance of the $\sqrt{N}$ enhancement of the atom-light coupling, previously observed for nearly isolated Rydberg superatoms [242, 189], on the non-equilibrium phase structure of the driven-dissipative system.

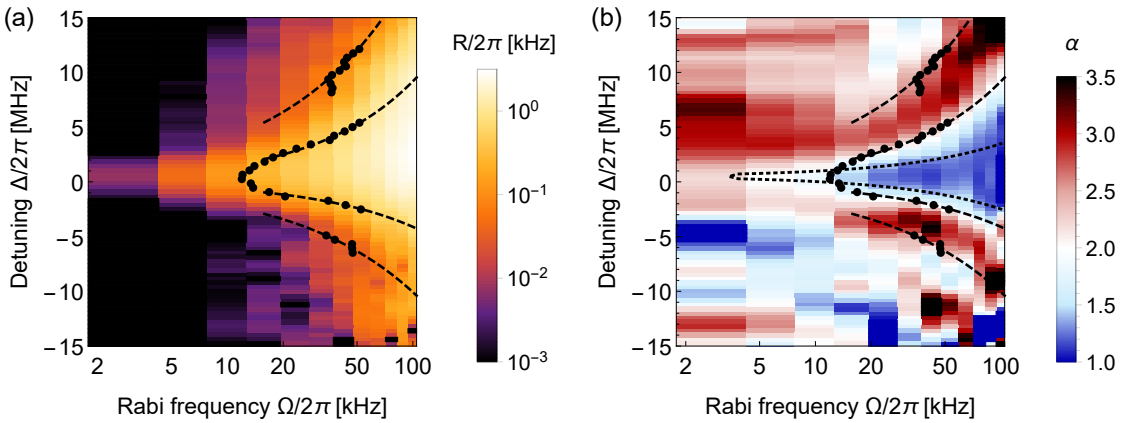

Figure 5.5: Experimentally measured non-equilibrium phase diagram. (a) As a function of the driving parameters (Δ, Ω) the loss rate R is fairly smooth with few distinguishing features. (b) In contrast, the locally determined scaling exponent α shows clearly distinguished regimes. The critical regime is identified as the blue region ($\alpha \approx 1.2$), while the unstable regime is red ($\alpha > 2$). The black points and dashed lines show the estimated boundary positions, the dotted line indicates the boundary to the critical regime predicted from mean-field theory corresponding to the highest density region of the cloud (trap center). Reproduced from [234].

The RE model also qualitatively reproduces the stronger scaling ($\alpha > 2$) of the loss rate found above resonance as a consequence of the instability (further enhanced by atomic motion). This is seen in the RE simulations in Figure 5.4(c)) as an upwards trend around $\Omega/2\pi \gtrsim 5\,\mathrm{kHz}$ for positive detunings. Fitting the RE simulations over a similar range of Ω and Δ as for the experimental data yields an exponent of $\alpha = 2.40 \pm 0.1$, while neglecting trap averaging $\alpha = 3.2 \pm 0.2$, which spans the range of values found experimentally. The RE model also reproduces the crossover to weaker scaling for large Ω connected to the critical regime (Fig. 5.4(c)).

5.6 Full non-equilibrium phase diagram in the particle number conserving limit

We have demonstrated that the rate of population loss and associated scaling laws provide a convenient and robust way to identify vastly different regimes of strongly-interacting open quantum systems. Using the experimentally observed scaling we can even map out the non-equilibrium phase diagram as a function of the control parameters Ω and Δ, as illustrated in Figure 5.5. To produce this phase diagram, the scaling exponents are obtained from the slopes of linear fits to $R(\Omega)$ in a moving window on a log-log scale. To locate the boundaries between the regimes we fit connected piecewise linear functions to the log-log-scaled loss rates for each detuning. In contrast to the loss rate R, which has relatively few distinguishing features (Fig. 5.5(a)), the scaling exponents show distinct regimes corresponding to the critical (blue) and unstable (red) scaling regimes (Fig. 5.5(b)). The dissipation dominated regime appears as a mostly white region within the detuning interval $|\Delta|/2\pi < 2\,\mathrm{MHz}$ and for $\Omega/2\pi \lesssim 12\,\mathrm{kHz}$. Looking at larger positive-to-negative detunings we note a slight trend from red-to-blue is apparent, which might be evidence of a weak interaction effect on the paramagnetic state.

Conclusion

To conclude, scaling laws found in the rate of population decay have made it possible to uncover the non-equilibrium phases of an Ising-like open quantum spin system governed by the competition between driving, dissipation and interactions. We show that the phase structure is extremely rich, exhibiting features which can be attributed to the equilibrium quantum Ising model, i.e. critical scaling in the regime where driving and interactions dominate, but also genuinely new non-equilibrium features, e.g. the collectively enhanced crossover from the dissipation-dominated to the critical regime and an instability towards strongly-correlated states for positive detunings. While the former appears to be captured by mean-field theory which approximates two-point correlations, the latter could only be adequately described using rate equation simulations including many-body correlations. The observed scaling laws also appear to be quite robust, as we find qualitatively similar behaviour for a wide range of Rydberg states including ns and nd states which posses different interaction strengths and anisotropies. Thus, we expect they will serve as a powerful tool for identifying universal and non-universal aspects of non-equilibrium quantum systems and as a benchmark for future many-body theories.

Future experiments aiming to learn more about the microscopic origins of this scaling behaviour could reveal the build up of spatial correlations between the spins (e.g. using high resolution imaging techniques for Rydberg atoms [191, 130]) or look for possible self similar dynamics in the transient evolution [243]. For these studies the unstable regime is of special interest since it has no counterpart in the equilibrium phase structure. One immediate possibility for experimental studies is to investigate the full temporal evolution beyond the time scale $(b\Gamma)^{-1}$ probed here, which we will attempt in the next chapter.

Exploring the non-conserving dynamics of Rydberg facilitation

6

Observing a many-body quantum system evolve is the essence of studying its behaviour, and even of the quantum simulator envisioned by Richard Feynman [244]. Rydberg spin systems are an ideal platform for following this idea [74, 112], because this system is accessible to both experiments and theory. The known microscopic details allow one to engineer system properties, and to bridge the gap between microscopic processes and macroscopic behaviour. Furthermore, these many-body systems are inherently open quantum systems governed by an intricate interplay between coherent driving, dissipation, and van der Waals interactions. In the preceding chapter we unravelled the phase structure resulting from this setting for particle-number conserving dynamics, which we found to comprise dissipation-dominated, paramagnetic and a critical regime, as well as an instability. The observed instability, which appears to separate paramagnetic and critical regimes for large positive detunings, was identified as a genuinely non-equilibrium feature without any counterpart in the equilibrium quantum phase structure of Rydberg spin systems.[1] A comparison to rate equation simulations suggested facilitated excitation driving the system to high excitation densities as a mechanism leading to this instability, however the details of this mechanism were not understood well. In this chapter we investigate this intriguing feature further by observing the many-body dynamics originating from the instability at timescales where particle loss has a strong effect on the system dynamics. We discover that the facilitation dynamics and non-conservation of particle number establish a new type of non-equilibrium many-body behaviour, which we identify as self-organisation to criticality.

The experiments reported in chapter 5 were subject to strong decay from the weakly coupled intermediate state. To attempt to reduce the dissipation rate by approximately one order of magnitude and to potentially extend the domain where many-body effects can be observed, we decided to implement a completely different laser excitation scheme in our apparatus. The experiments discussed in this chapter are based on single-photon excitation, completely eliminating intermediate state laser coupling and reducing the total decay rate to $\Gamma/2\pi \sim 10\,\mathrm{kHz}$.[2]

At the onset of this chapter we show experimentally that we are able to access strongly interacting many-body regimes with the new single-photon excitation. As a result we could verify that the observed phase structure is remarkably robust concerning different excitation schemes as well as the strength and anisotropy of the van der Walls interaction. From there we embark on investigating the full temporal many-body dynamics associated to the instability, observing it as a function of driving strength and initial atom density. We discover that for strong laser driving associated to the critical regime the system reaches

[1] The equilibrium phase structure of the non-dissipative Rydberg quantum spin system was outlined in section 3.3.2.

[2] The details of this new experimental setup were presented in section 2.3.

a steady-state characterised by an atom density independent of the initial density and obeying powerlaw scaling with the laser driving strength. These surprising observations, combined with a clear separation of timescales between facilitated excitation and particle loss on the microscopic level, allow us to identify self-organised criticality as the mechanism governing the many-body behaviour of the system in this regime.

6.1 Rydberg spin systems with single-photon driving

To improve our control over the Rydberg excitation and completely eliminate the strong dissipation from laser-coupled intermediate states observed with two-photon excitation (cf. sec. 5.2), we implemented a new excitation scheme based on single-photon excitation. Here, the ground and Rydberg states, i.e. our two spin states, are coupled directly. It comprises a frequency doubled dye laser generating ultraviolet light with a wavelength around 288 nm and a maximum output power of 80 mW, which we use to drive transitions from the initial state $|\downarrow\rangle = |4s_{1/2}, F = 1\rangle$ to the $|\uparrow\rangle = |39p_{3/2}\rangle$ Rydberg state. Utilizing this new laser system, the relevant Rydberg-Rydberg and atom-light interactions have different parameters compared to the previous chapter. The driving strength of the excitation laser was calibrated by measuring the lightshift induced on ground state atoms with Ramsey interferometry (see app. B). By additionally measuring the power of the excitation laser for every repetition of the experiment, we can log the driving strength for every data point. We estimate that the relative statistical error of the driving strength due to e.g. shot-to-shot power fluctuations is 0.2 %. We achieve driving strengths $\Omega/2\pi$ between 20 kHz (limited by the sensitivity of the used photo diode for power measurement) and 200 kHz (limited by laser power). We estimate the dephasing rate to be $\gamma_{\mathrm{de}}/2\pi = 360\,\mathrm{kHz}$, based on independent laser linewidth measurements. The van der Waals interaction between Rydberg excitations is anisotropic [167], with maximum strength $C_6/2\pi = 600\,\mathrm{MHz}\,\mu\mathrm{m}^6$ [174]. The excited state decay rate is a combination of the bare Rydberg state decay including blackbody transitions $\Gamma/2\pi = 3\,\mathrm{kHz}$ [181] and photoionisation due to the dipole trap laser, which we estimate to be between $\Gamma_{\mathrm{PI}}/2\pi = 1\,\mathrm{kHz}$ and 10 kHz [166, 167]. We estimate that any charged particles produced in this way are lost from the trap on a timescale $< 1\,\mathrm{ms}$, and therefore have no great effect on the dynamics of the system, apart from an overall atom loss.

The setup for cooling and trapping of ultracold atoms, as well as the cloud geometry remained essentially unchanged compared to the previous chapter (cf. chap. 2 and sec. 5.2). We trap up to 10^5 ^{39}K atoms with maximum peak atom density $n_0 = 2.6 \cdot 10^{11}\,\mathrm{cm}^{-3}$, estimated from absorption images of the atom cloud, and 40 µK temperature in a cigar shaped optical dipole trap. We vary the atom density independent of the dipole trap potential depth by changing the loading time of the 3D-MOT between 30 ms and 1 s, allowing us to prepare atom clouds with initial peak densities as low as $5 \cdot 10^{10}\,\mathrm{cm}^{-3}$. The atomic cloud has maximum $e^{-1/2}$ radii $\{\sigma_r, \sigma_z\} \approx \{10\,\mu\mathrm{m}, 200\,\mu\mathrm{m}\}$, determined from absorption images. The driving laser was aligned collinearly to the long cloud axis to combine homogeneity with maximal intensity of the excitation laser across the atom cloud.

Since the interaction and decay properties as well as the driving mechanism are different in this new setup compared to chapter 5, we will first test whether the resonant strong driving regime can be reached, before embarking on studying the temporal dynamics of Rydberg facilitation in section 6.2.

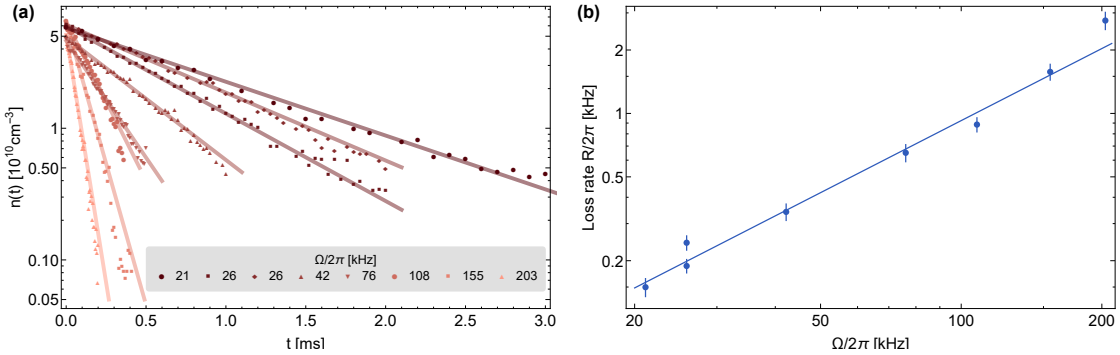

Figure 6.1: Powerlaw scaling of measured population loss rates R for different driving strengths of resonant single-photon driving. (a) Time resolved measurement of the remaining atom density n after an excitation period of varying duration for driving strengths Ω spanning a full order of magnitude. The decay is well approximated by exponential loss with population loss rates R for all probed driving strengths. (b) Scaling of the loss rate as a function of driving strength. The loss rate exhibits power law scaling Ω^α with fitted scaling exponent $\alpha = 1.14(6)$, indicating behaviour of the critical regime. This shows that strong driving underlies the observed many-body dynamics.

6.1.1 Verifying strong driving to critical behaviour

We start by verifying that key features of the non-equilibrium phase structure observed in chapter 5 persist, given the very different parameters realized using the single-photon excitation scheme. In the previous chapter we found that the initial loss dynamics follows an exponential decay with a measured population loss rate R, which exhibits powerlaw scaling as a function of the driving strength (Ω^α) with a scaling exponent α characteristic of the non-equilibrium regimes of behaviour. On resonance and for strong driving we observed a scaling exponent $\alpha \approx 1.185$, which was linked to the critical regime of the non-dissipative equilibrium Rydberg spin system with the scaling exponent $\alpha = 2/5$ modified by trap averaging effects.

Using single photon excitation, we measured the evolution of the peak atom density $n(t)$ on resonance for driving strengths covering a full order of magnitude from $\Omega/2\pi = 20\,\mathrm{kHz}$ up to $200\,\mathrm{kHz}$, which we show in Figure 6.1. We observe that the initial evolution of the remaining atom density after an excitation time t is well described by the expected exponential decay for all probed driving strengths. Here we plot the atom density, contrary to the fraction of remaining atoms given in chapter 5, since we will also investigate the dynamical evolution for different initial densities in this chapter. We estimate the standard deviation of the density in this dataset to be $1 \cdot 10^9\,\mathrm{cm}^{-3}$. The resonance position was determined spectroscopically at low densities and driving strengths. The observed change of the loss rate relative to the driving strength follows a power law with least-squares fitted scaling exponent $\alpha = 1.14$ and standard deviation 0.06. This value is in very good agreement with the scaling exponent of the critical regime observed in the last chapter. A crossover to the dissipative regime at weak laser driving was not observed in this measurement, showing that we are able to access the strongly interacting many-body regime across the full available range of driving strengths on resonance.[3] These measurements verify that the scaling laws discovered in chapter 5 are a robust feature of the many-body dynamics

[3] To access smaller driving strength, a more sensitive photodiode measuring the excitation laser power would be required, which can be implemented without difficulty in future experiments.

that are not strongly influenced by the anisotropy and strength of the interactions or the nature of dominant dissipative processes.

6.2 Investigating the dynamics of facilitation and particle loss

The central objective of the experiments presented in this chapter is to explore the many-body evolution of driven-dissipative Rydberg spin systems at far-detuned regimes governed by facilitation and particle loss. Facilitation is a cooperative process arising in Rydberg spin systems, which becomes dominant for large detunings $|\Delta| \gg \Omega,\ \Gamma + \gamma_{\mathrm{de}}$, such that the detuning of the driving field can compensate the long-range van der Waals interactions between Rydberg excitations. Then the interaction potential originating from a seed excitation shifts other nearby atoms into resonance, leading to facilitated (de)excitation (cf. sec. 3.3.1). In the experiments discussed in this chapter we are interested in evolution times long compared to both single-body decay and dephasing, such that the microscopic rates of these processes can be obtained from the effective classical rate equation model introduced in section 3.4.2. With the experiments in chapter 5 we established that this model describes the behaviour of our system well. Then the dynamics of our system can be thought off as being governed by a set of microscopic processes comprising facilitated (de)excitation (rate Γ_f), seed excitation (Γ_s), decay of excited atoms (Γ) and loss of atoms in the excited state (Γ_{loss}), which are given by

$$\Gamma_f = \frac{\Omega^2}{\Gamma + \gamma_{\mathrm{de}}}, \qquad \Gamma_s = (\Gamma + \gamma_{\mathrm{de}})\frac{\Omega^2}{4\Delta^2}, \qquad \Gamma_{\mathrm{loss}} = b\Gamma. \tag{6.1}$$

The branching ratio for the decay out of the system is denoted by b. Since facilitation is near-resonant, this process can be much faster than off-resonant (de)excitation of isolated seeds in our experiments, depending on the atom density. At a macroscopic level, the microscopic loss rate Γ_{loss} leads to an overall loss of particle density as the system evolves. The (macroscopic) population loss rate $R_t = R(t)$ at any evolution time t is related to the instantaneous Rydberg excitation density ρ_t of the system via $R_t = \partial_t n_t = \Gamma_{\mathrm{loss}}\rho_t$.[4] Thus, measuring n_t will allow us to gain insight into the internal dynamics of our system on all timescales of interest.

In the previous chapter we studied the phase structure of our system for early evolution times where we found that the population loss rate is constant, which we denote as the initial population loss rate R. On timescales early compared to the inverse population loss rate R^{-1}, the internal dynamics of the Rydberg spin system is only weakly perturbed by the particle loss, which we refer to as particle-number conserving dynamics. The phase structure governing the early time behaviour consists of an instability separating a paramagnetic and a critical regime. The paramagnetic regime is characterised by a small Rydberg excitation fraction, corresponding to slow particle loss and single-body behaviour with powerlaw ($R \propto \Omega^\alpha$) scaling exponent $\alpha = 2$. In the critical regime, the excitation fraction is sufficiently large to lead to interactions competing with driving, such that Rydberg blockade suppresses the growth of excitation density with driving strength ($\alpha < 2$). At the instability, the excitation fraction increases rapidly over a small range of

[4] This equation arises from the statistical average over atoms j of the classical master equation (3.23), where $n_t = \langle n_t^{(j)} \rangle$ and $\rho_t = \langle \rho_t^{(j)} \rangle$.

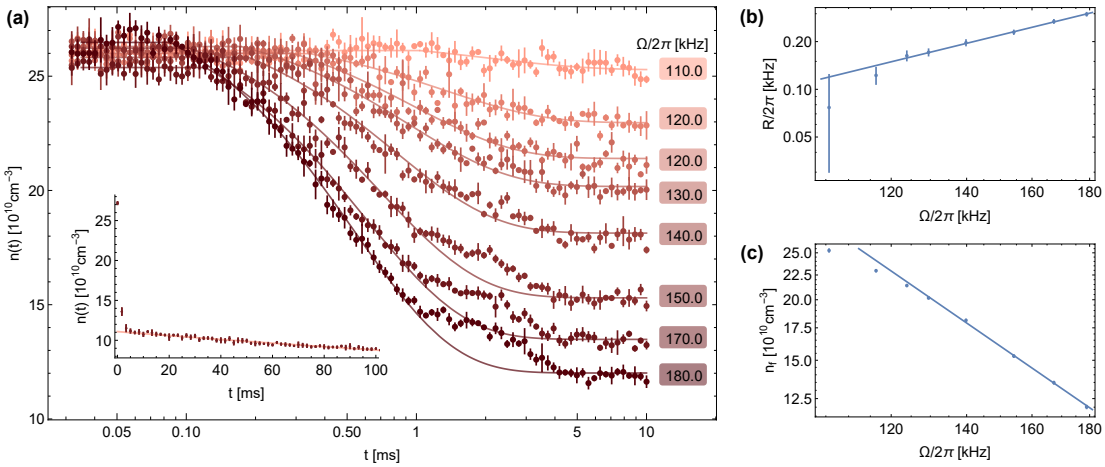

Figure 6.2: Many-body dynamical evolution under Rydberg facilitation conditions for fixed initial density. These measurements were performed for $\Delta/2\pi = 30\,\mathrm{MHz}$. (a) The evolution of the final atom density $n(t)$ after evolution time t for driving strengths $\Omega/2\pi > 100\,\mathrm{kHz}$ shows an initial plateau of constant density followed by fast population decay saturating at a finite steady state density. The observed temporal behaviour is well reproduced by fits of delayed exponential curves $n_0 \exp[-R(t-t_0)] + n_f$ (solid lines), except for a short time window of reduced loss rate before the steady-state density is reached. The error bars give the standard error calculated from three independent repetitions. The inset shows the slow decay of the steady state density on very long timescales, here up to 100 ms for $\Omega/2\pi = 180\,\mathrm{kHz}$. A pure exponentially decaying fit produced a loss rate of $R = 0.37(1)\,\mathrm{Hz}$ represented by the solid line. (b) The population loss rate R of the early exponential decay follows a powerlaw Ω^α with measured scaling exponent $\alpha = 1.7(1)$ (solid line). For the smallest two driving strengths investigated here, we observe loss rates below this line, indicating the onset of the instability. (c) The steady-state densities n_f follow a powerlaw behaviour for the same range of driving strengths as R, with measured powerlaw scaling $\Omega^{-\beta}$ and a measured $\beta = 1.60(2)$. In this plot, the error bars are smaller than the point size.

driving strengths to connect from small to large excitation fractions (and the corresponding slow to fast loss) leading to $\alpha > 2$.

In the following, we will investigate the many-body dynamics of far-detuned regimes in the vicinity of the instability, extending the covered evolution times beyond the initial loss investigated previously.[5] We expect that the interplay between the internal dynamics of the Rydberg spin system and the particle loss will lead to new non-equilibrium behaviour, since the resulting behaviour now depends on the excitation history of the system, i.e. the temporal dynamics is non-Markovian (cf. sec. 3.2.4). We begin by observing the evolution of the atom density for a large initial density as a function of driving strength, allowing us to verify the particle-number conserving phase structure including the existence of the instability, and to observe first features of the non-conserving behaviour. We then repeat this experiment keeping the driving strength constant and varying the initial atom density. This will establish the initial density as a new system parameter of the non-equilibrium dynamics.

[5] We saw already in Figure 5.2 that the initial exponential decay breaks off at later times leading to new features of the many-body dynamics.

Figure 6.2 shows the dynamical evolution for a fixed initial density ($n_0 \approx 2.6 \cdot 10^{11}\,\mathrm{cm}^{-3}$, $\Delta/2\pi = 30\,\mathrm{MHz}$) as a function of driving strength over three orders of magnitude in time ($t = 30\,\mu\mathrm{s}$ to $10\,\mathrm{ms}$). We observe two strikingly distinct regimes of dynamical evolution. For sufficiently large driving strengths (Fig. 6.2), the atom density evolves according to a distinctive pattern of a short initial plateau of constant density, followed by fast decay which saturates at a finite steady-state density n_f. The previous chapter focussed on the initial part of this evolution, which is well described by an exponential decay time dependence. For low driving strengths ($\Omega/2\pi \lesssim 100\,\mathrm{kHz}$), we find that the dynamics are effectively frozen on the same observation times $t \leq 10\,\mathrm{ms}$, such that $n_f \approx n_0$. Going to much longer excitation times ($t \leq 100\,\mathrm{ms}$) in both regimes, we observe a subsequent very slow decay with much smaller loss rates $R_\infty/2\pi \lesssim 1\,\mathrm{Hz}$ (inset Fig. 6.2(a)). Since the slow loss is present for all driving strengths, it can be associated to excitation of isolated seeds with rate Γ_s. Hence, we conclude that the observed weak driving regime is governed by small excitation fractions characteristic of paramagnetic behaviour on all investigated timescales. In the opposite strong driving regime the fast initial loss and the subsequent slow loss act on very different time scales, such that n_f characterises the steady state of the non-equilibrium dynamics.

To parametrise the observed pattern of dynamical evolution in the strongly driven regime in Figure 6.2(a), we fit the data with delayed exponential functions $n_0 \exp[-R(t-t_0)] + n_f$, where R is the initial atom loss rate and t_0 a delay time, which accounts for the onset time of facilitated dynamics depending on the slow seed excitation rate. We do not investigate the delay time in the following, but investigate focus on the dynamics at later times. This phenomenological function reproduces the observed behaviour well (solid lines), except for a short time window between exponential decay and saturation where the particle loss slows down noticeably. To determine the origin of this feature remains the objective of future experiments. Focussing on the loss and saturation dynamics, we find that the initial loss rate R follows a power law for sufficiently large driving strengths (Fig. 6.2(b)) with scaling exponent $\alpha = 1.7(1)$. Similar scaling behaviour with $\alpha < 2$ at far detuned and strong driving conditions was observed in the previous chapter and associated to facilitation driving the system to states with high excitation density similar to the critical regime (cf. Fig. 5.5). For driving strengths between 100 kHz and 120 kHz, i.e. just above the paramagnetic regime, the observed loss rates deviate to smaller values below this scaling relation, suggesting scaling behaviour of the instability at the crossover to the paramagnetic regime. Turning to the steady-state density characterising late evolution times, we find very similar behaviour (Fig. 6.2(c)). For strong driving n_f follows a powerlaw $\Omega^{-\beta}$ with measured scaling exponent $\beta = 1.60(2)$. We will explore this scaling relation further in the following. The steady-state density also shows a crossover in behaviour between 100 kHz and 120 kHz driving strength in analogy to the loss rate R, where n_f starts to plateau at the level of the initial density. This suggests that the position of the instability marks a common phase boundary between different regimes of behaviour across all timescales and irrespective of particle loss.

In the next step, we further characterise the dynamical evolution of the system as a function of the initial atom density n_0 and at maximal driving strength (with the laser parameters $\Omega/2\pi \approx 190\,\mathrm{kHz}$ and $\Delta/2\pi = 30\,\mathrm{MHz}$). In the experiment, we change the initial atom density and keep the depth of the optical dipole trap fixed, by changing the loading time of the 3D-MOT (for details see sec. 2.2). The resulting temporal dynamics given in Figure 6.3(a) shows the same striking two regimes of dynamical evolution, and the

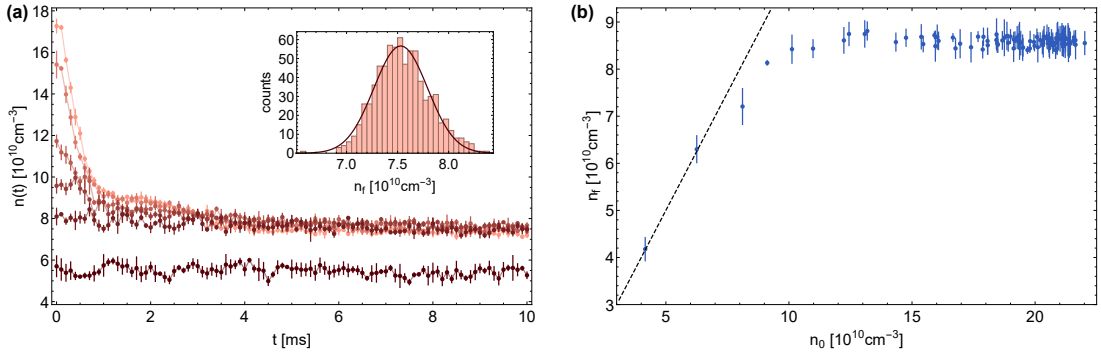

Figure 6.3: Steady-state density for fixed driving strength. (a) Temporal evolution of the atom density. For high initial density we see a fast initial decay to a finite steady-state density which is independent of the initial density. For lower initial densities no evolution is measured. We used linear sampling here to highlight the steady-state plateau at late times. (b) Steady-state density versus initial density. A sharp crossover between the regime of frozen dynamics (the dashed black line indicates $n_f = n_0$) and the regime of loss to a steady state plateau independent of the initial state. The datasets in (a) and (b) were both taken for $\Omega/2\pi \approx 190\,\mathrm{kHz}$ and $\Delta/2\pi = 30\,\mathrm{MHz}$, but on different days. We attribute the small change in steady-state density to slow drifts in the overlap between the atom cloud and the excitation laser. In both panels the error bars give the standard error calculated from three independent repetitions.

same saturation dynamics in the high initial density regime as seen before for strong driving. Even more so, we discover that the steady-state density is independent of the initial density n_0 for sufficiently high n_0. To highlight this behaviour further, we show in Figure 6.3(b) the steady-state density after 10 ms driving as a function of initial density. Here, the regime of nearly frozen dynamics is revealed by a slope of unity indicated by the black dashed line, which shows a sharp crossover into the regime of constant steady-state density for large initial densities. The behaviour in the high density regime is characteristic of an attractor of the dynamics, which brings the system to the same steady state independent of the initial conditions. The inset in Figure 6.3(a) shows the distribution of steady-state densities for data points between 5 and 10 ms, for which we find that the distribution is Gaussian. The standard deviation of this distribution is compatible with the shot-to-shot fluctuations given by the noise in our absorption imaging. This indicates that the system evolution stops at a unique steady-state density that is independent of the initial state within the measurement resolution.

The previous two experiments revealed that the particle loss has a dramatic influence on the behaviour of the system. As key signature of this evolution we have identified the steady-state density n_f, which is an attractor of the evolution of the particle density for strong driving and high initial density. These observations suggest that the non-conservation of particle number at late times leads to a new regime of many-body behaviour, which can not be related to equilibrium critical properties, but arises from the purely non-equilibrium interplay between facilitation and particle loss. In the following we will employ the steady-state density as an observable to further characterise the non-equilibrium phase structure without number conservation.

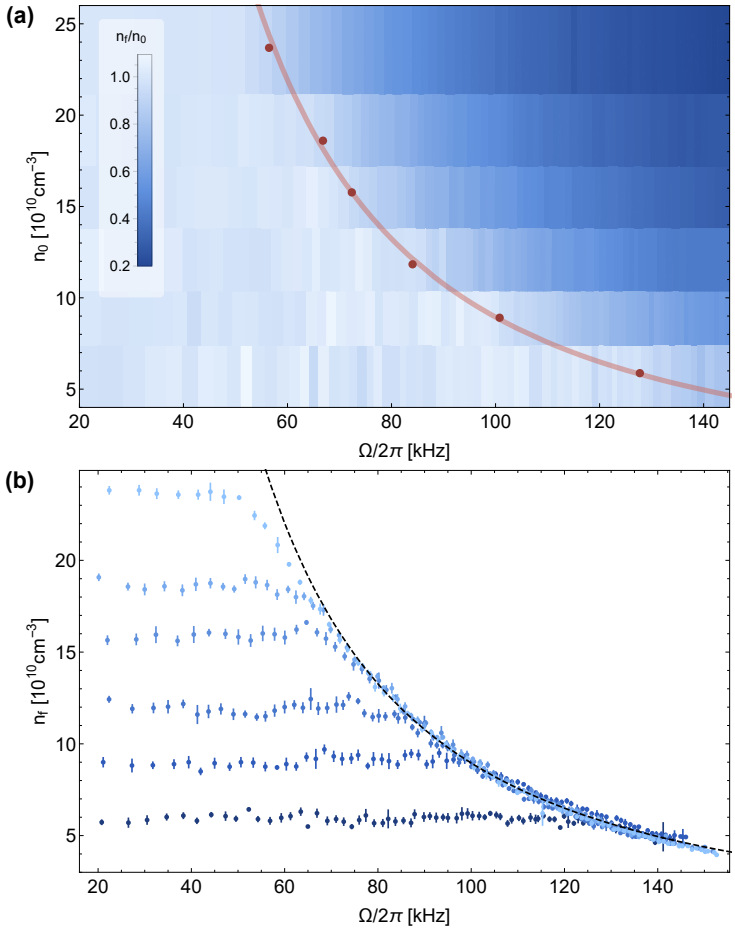

Figure 6.4: Non-equilibrium phase diagram of the non-conserving system corresponding to the late-time steady-state with density n_f. These measurements were performed for $\Delta/2\pi = 18\,\mathrm{MHz}$. (a) The phase diagram shows two regimes of behaviour, characterised by $n_f/n_0 \approx 1$ (light blue) and $n_f/n_0 < 1$ (dark blue). The red points and line indicate the transition between the two (see main text), which follow a powerlaw $\Omega^{-\beta}$ with $\beta = 1.74(1)$. (b) The same data plotted on top of each other, with lighter hues of blue corresponding to higher initial densities. The initial density n_0 can be readily read off in the weak driving regime to the left. In the strong driving regime, all points collapse onto a single curve, which is independent of initial conditions and follows the fitted powerlaw $\Omega^{-\beta}$ with $\beta = 1.76(2)$ (black dashed curve).

6.2.1 Phase diagram with particle loss

To unveil the non-equilibrium phase diagram of the two observed regimes of behaviour at late times, we performed a new set of experiments measuring the steady-state density n_f. To this end we measure the atom density at $t = 10\,\mathrm{ms}$ against almost an order of magnitude in both initial density n_0 and driving strength Ω (for this measurement, $\Delta/2\pi = 18\,\mathrm{MHz}$).[6]

[6] This measurement was taken with five repetitions for each datapoint and 100 laser excitation powers. For every dataset with fixed initial density, the logged optical powers of the excitation laser were binned linearly with 80 bins and the mean and standard error determined for every bin individually, giving on average 6 measurement points per bin. The optical power associated to each bin was then converted to a driving strength.

Figure 6.4(a) shows the late time non-equilibrium phase diagram, which comprises two separate regimes of non-equilibrium behaviour: For low initial density and driving strength, $n_f/n_0 = 1$ is observed (light blue), i.e. the system is in the paramagnetic regime. In the opposite regime we find $n_f/n_0 < 1$ (dark blue).[7]

To inspect the behaviour in the strong driving and high initial density regime, as well as the transition to the opposite regime, it is instructive to plot the $n_f(\Omega)$ curves for the different n_0 on top of each other, as is shown in Figure 6.4(b). Here it becomes apparent that all curves in the high density, strong driving regime collapse onto a single curve, which is independent of the initial state. We observe that this curve follows a powerlaw $n_f \propto \Omega^{-\beta}$, for which we measure the scaling exponent $\beta = 1.76(2)$. This value is close to the previous estimate of $\beta = 1.60(2)$ in Figure 6.2(c), which was measured for a fixed initial density. We also observe that the two regimes of behaviour are separated by a sharp crossover. The red points in Figure 6.4(a) are estimates of the transition driving strengths based on fits of a piecewise function (constant for low driving strength and powerlaw decay otherwise) to datasets with fixed initial densities. The red line is the previously determined powerlaw curve $n_f \propto \Omega^{-\beta}$, which the estimated crossover points follow closely.

In the presented experiments we were able to show that the non-Markovian dynamics of our Rydberg spin system exhibits an attractor state characterised by a steady-state density which is independent of the initial state and follows a powerlaw as a function of the driving strength. In the following we speculate on the microscopic mechanisms leading to this behaviour.

6.3 Self-organisation driving the system to criticality

The observations that the system tends to evolve to a unique steady state independent of initial conditions, and that the steady state density follows a powerlaw are suggestive of self-organised criticality (SOC). This is an organising mechanism which is conjectured to occur in non-equilibrium many-body systems, where the dynamics includes particle exchange with an external reservoir bringing the system to the critical state of an absorbing-state phase transition [14, 59, 245, 61, 246, 60, 247]. An absorbing state phase transition is associated to the competition between decay and non-linear spreading processes. [8] SOC typically is associated with the emergence of characteristic spatio-temporal correlations on all scales of the system in the thermodynamic limit (i.e. if it is infinitely large), and without the need to fine tune system parameters to reach the critical state of the absorbing phase transition. Instead, this critical state is an attractor of the dynamics, assuming that particle addition Γ_{load} and particle loss Γ_{loss} act on timescales infinitely longer than the internal system dynamics, and that particle addition is infinitely slower than particle loss [248, 245, 71], i.e.

$$\Gamma_{\text{load}},\ \Gamma_{\text{loss}} \to 0 \qquad \text{and} \qquad \frac{\Gamma_{\text{load}}}{\Gamma_{\text{loss}}} \to 0. \tag{6.2}$$

These conditions imply that SOC arises in a slow-driving limit, where all internal dynamics of the system is faster than the external particle exchange. In a physical experiment, these

[7] In the previous measurements we investigated cross sections through this phase diagram for fixed driving strength and fixed initial density.

[8] We introduced absorbing state phase transitions in section 1.2.2.

conditions can only be realised in an approximate sense, requiring instead

$$\Gamma_{\text{internal}} \gg \Gamma_{\text{loss}} \gg \Gamma_{\text{load}}. \tag{6.3}$$

In the temporal evolution, the addition of particles will increase the total particle density $n(t)$ in the inactive phase ($\partial_t n > 0$) until the critical density is reached and the system becomes active, while the particle loss decreases the overall particle density ($\partial_t n < 0$) in the active phase till the system becomes subcritical. Therefore the particle density in the non-equilibrium steady-state becomes independent of the initial state of the system, and fluctuates around the characteristic critical steady-state value n_f which was reached by the self-organisation process. The dynamics of the system at criticality is characterised by redistribution avalanches within the internal state space following a powerlaw distribution [59].

We have identified four requirements of SOC [248, 71, 59], which we will verify in the following in the context of our experimental results.

- Competing microscopic processes leading to an absorbing state phase transition. In the limit if no so seed excitation $\Gamma_s \to 0$ and for particle number conservation, facilitated excitation can be identified as branching and facilitated deexcitation as coalescence, which both compete with decay as is illustrated in Figure 6.5(a). In this analogy the ground state of the atoms is identified as the inactive state and the Rydberg state as the active state. The combination of facilitation and decay processes gives rise to an absorbing state phase transition with the excitation density ρ as the order parameter, which has been conjectured to be part of the directed percolation universality class [49]. This non-equilibrium phase transition comprises an inactive (absorbing) phase with vanishing excitation density ($\rho = 0$) below a critical facilitation rate, and a corresponding active (fluctuating) phase where a finite excitation density prevails for all times (Fig. 6.5(b)). The observed transition from a state with vanishingly small excitation density (previously referred to as paramagnetic behaviour) and high excitation density is characteristic of this absorbing-state phase transition. Signatures of this absorbing state phase transition have also been observed in [48].

- Non-conservation of particle number. In general, this is associated to the external addition and loss of particles. In our experiments only particle loss is present, such that an organising process can only be observed in the active phase. In our system the facilitation rate depends on the laser driving strength of the laser coupling, giving rise to the observed two regimes of behaviour e.g. in Figure 6.4, where the system is inactive for small driving strengths and active/self-organising for strong driving. We will refer to these two regimes as inactive and active, respectively, in the following.

- Separation of timescales between facilitation dynamics and particle loss. This condition is satisfied on the basis of the microscopic parameters in equation (6.1). Looking at the measured macroscopic rate of population loss R (e.g. Figure 6.2(b)), we find that it is slower than any timescale associated with the internal state dynamics, except for the seed excitation rate. Therefore the observed temporal evolution of the particle density corresponds to slow self-organising avalanches towards the critical state (Fig. 6.5(c)).

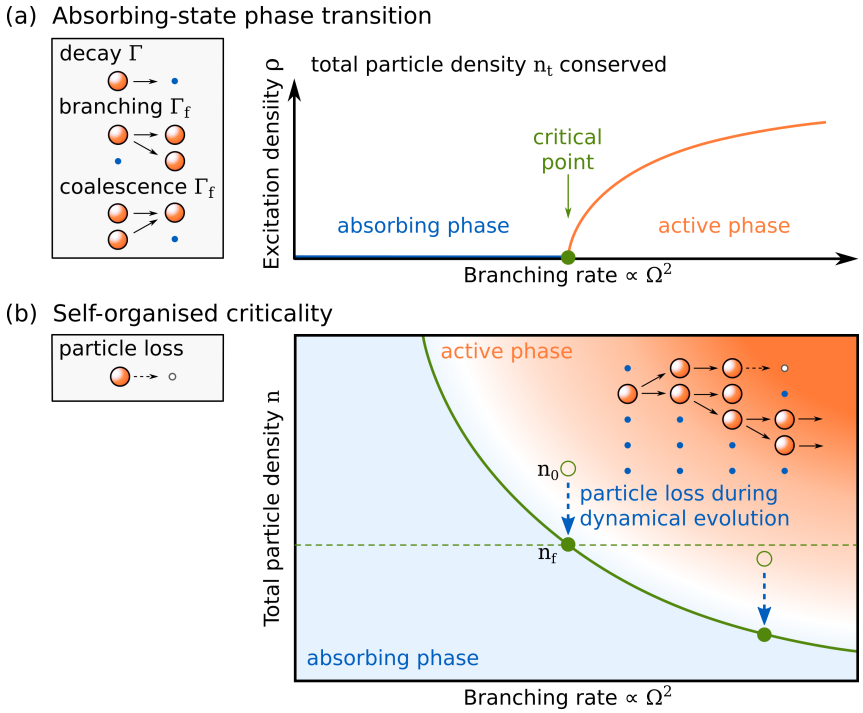

Figure 6.5: Self-organised criticality arising from an absorbing state phase transition augmented by slow particle exchange with an external reservoir. (a) Illustration of the absorbing state phase transition realised by Rydberg spin systems in the absence of independent seed excitation and particle exchange. Microscopically, externally driven facilitation realises branching and coalescence processes, in addition to decay of excitations. We illustrate the excited Rydberg state (the active state) by large orange spheres, and the ground state (inactive) as small blue circles. The density of excitations ρ is the order parameter of the phase transition between an inactive (absorbing) phase and an active (fluctuating) phase. The critical point characterising this second order phase transition occurs at a specific value of the branching rate, which can be controlled externally by the driving strength in our experiments. (b) In our experiments loss of particles in the excited state is an additional process governing the system. Then the total particle density is an additional system parameter, which is self-organised in the active phase (starting from the initial density n_0) by the system dynamics till the critical state (with density n_f) is reached. The mechanism of the self-organisation dynamics is independent of the branching rate.

- Vanishingly small seed excitation rate. Independent seed excitation acts as a conjugate field of the absorbing state phase transition generating excitation density independent of the system dynamics. Thereby additional fluctuations are added to the state of the system, introducing a gap to the critical point of the phase transition and perturbing the inactive phase. The microscopic processes in equation (6.1) satisfy the condition that the seeding rate is the smallest rate in the system for all probed driving strengths. This condition is corroborated by the observed clear separation between fast and slow loss regimes in Figure 6.2(a). Thus the gap introduced by the seeding process is very small in our experiments.

In the following we will summarise the expected consequences of SOC in the context of our experiments. We have observed a unique steady state which is independent of the initial conditions. Furthermore, we observe the same qualitative saturation behaviour independent of the driving strength, which suggests that the underlying self-organising

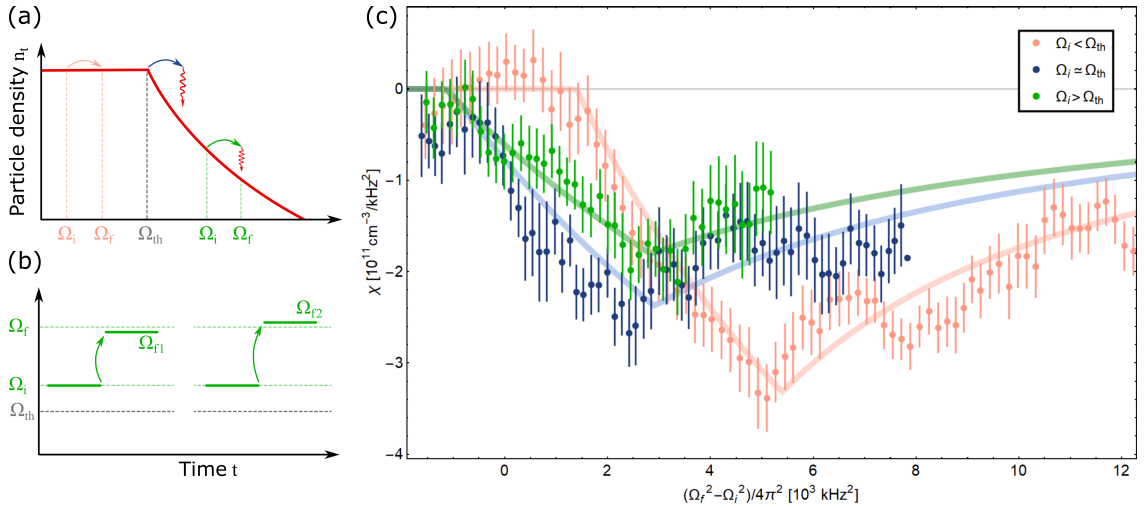

Figure 6.6: Measurement of the response of the many-body state of the system to a perturbation in the driving strength. (a) We probe the system response by preparing the system in the steady-state for a driving strength Ω_i and subsequently switching to a different driving strength Ω_f for which we observe the resulting steady-state density. We investigate three different scenarios, starting from an initial driving strength Ω_i below (light red), at (dark blue) or above (green) the crossover (Ω_{th}) between the inactive and the SOC regimes. The thick red line represents the observed shape of the steady state density, which is flat in the inactive regime and follows a powerlaw in the SOC regime. (b) We parametrise the system response by comparing resulting steady state densities of two final driving strengths $\Omega_{f1} < \Omega_f$ and $\Omega_{f2} > \Omega_f$ measured in subsequent experimental cycles ($\mathrm{d}n = n(\Omega_{f1}) - n(\Omega_{f2})$) with a constant difference in final driving strengths $\mathrm{d}\Omega_f^2 = \Omega_{f1}^2 - \Omega_{f2}^2$. (c) The measured susceptibility $\chi = \mathrm{d}n/\mathrm{d}\Omega_f^2$ for the three different initial driving strengths.

mechanism requires no fine tuning of system parameters, in agreement with the SOC mechanism. Critical properties of the self-organised state typically are associated to powerlaw distributions of spatial and temporal properties of reordering avalanches [59, 61, 67, 70]. We have observed the properties of the steady state in a different observable, which is the dependence of the steady state density on the microscopic facilitation rate. The observed powerlaw scaling is highly suggestive of critical properties of the steady state. The relevant mass scale for determining universal scaling properties is Ω^2, since the facilitation rate is proportional to the square of the driving strength. The thus measured scaling exponent of the steady-state density as a function of the facilitation rate ($n_f \propto (\Omega^2)^{-\beta}$) is $\beta = 0.88(2)$. It is interesting that this value is close to the universal scaling exponent of the directed percolation absorbing-state phase transition ($\beta = 0.813(9)$ [14]), which was also conjectured based on the microscopic processes [49]. However, further experiments reducing systematic effects and careful quantitative comparison to microscopic theory, including for example potential effects due to inhomogeneous distributions associated to the dipole trap, need to be undertaken to elucidate the nature of the critical state.

To further test the conjecture of SOC giving rise to the observed behaviour, we performed one more experiment investigating the sensitivity of the steady-state density to perturbations. After having demonstrated that the strong driving, high initial density regime is fully governed by the attractor which exhibits power law scaling, we now investigate whether this state persists after a perturbation. If indeed the steady state corresponds to a self-organised critical state in the active phase, it should exhibit a strong sensitivity

to external perturbations which trigger excitation avalanches returning the system to the critical state. To this end we first prepare the system in an initial state with driving strength Ω_i and allow the system to evolve to the steady state density $n(\Omega_i)$ for an exposure time $t = 10\,\mathrm{ms}$ (Fig. 6.6(a)). Then the driving strength is changed abruptly to a new value Ω_f, for which we measure the new steady-state density $n(\Omega_f)$ after further 10 ms evolution. We probe the system response by comparing two final states with $\mathrm{d}n = n(\Omega_{f1}) - n(\Omega_{f2})$, separated by a constant driving strength difference $\mathrm{d}\Omega_f^2 = \Omega_{f1}^2 - \Omega_{f2}^2$ (Fig. 6.6(b)). We here use Ω^2 to parametrise the atom-light coupling strength, since this is the relevant mass scale of the microscopic processes. The system response can be parametrised via the susceptibility $\chi = \mathrm{d}n/\mathrm{d}\Omega_f^2$ measured as a function of the distance between initial and finial driving strengths $\mathrm{d}\Omega^2 = \Omega_f^2 - \Omega_i^2$. This susceptibility observable compares two density measurements obtained with the same exposure protocol but different final driving strengths Ω_{f1}, Ω_{f2} to subtract and thereby reduce potential systematic effects.

In the following we present in Figure 6.6(c) three different experiments showing the susceptibility for Ω_i values below, close to, and above the threshold value Ω_{th} for the absorbing state phase transition (measured for $\Delta/2\pi = 24\,\mathrm{MHz}$). All three curves qualitatively follow the same qualitative shape. The susceptibility is very close to zero for small distances to the initial driving strength $\mathrm{d}\Omega^2 = \Omega_f^2 - \Omega_i^2$, which is characteristic of no system response in the inactive phase. For stronger $\mathrm{d}\Omega^2$ values a pronounced minimum of strong susceptibility to the perturbation develops, signifying that the system strongly adapts to the perturbation and thereby losing atom density by the self-organising process in the active phase. The distance between the onset of increased susceptibility and the strongest susceptibility should be identical in an ideal experiment where $\mathrm{d}\Omega_f^2 \to 0$, resulting in a discontinuity. The transition is smoothed here due to the finite $\mathrm{d}\Omega_f^2/4\pi^2 \approx 10^3\,\mathrm{kHz}^2$ and an applied moving average to reduce statistical noise of $\mathrm{d}n$. For $\Omega_i < \Omega_{th}$ (light red points), the onset of strong susceptibility occurs at positive $\mathrm{d}\Omega^2$, showing that the active phase is reached only above a threshold value. The measured susceptibility curve for $\Omega_i \simeq \Omega_{th}$ (dark blue points) shows an onset of strong susceptibility close to $\mathrm{d}\Omega^2 = 0$, which is perturbed slightly by the moving average, showing that in this measurement the system was prepared in a highly susceptible initial state. If the system is prepared within the active phase for $\Omega_i > \Omega_{th}$ (green points), the onset of the susceptibility curve again lies close to zero, indicating that the system is characterised by a strong system response within the active phase irrespective of the value of the driving strength. These measurements suggest that the steady-state of the system indeed returns to the critical state, in agreement with self-organised criticality. Based on this observation we have overlaid the data points with calculated curves of the susceptibility, which are based on the measured $n_f(\Omega_f)$ values (including the measured $\mathrm{d}\Omega_f^2$) and the assumption that the state of the system always falls back onto the same curve $n(\Omega_f)$ after the perturbation for $\Omega_f > \Omega_i, \Omega_{th}$ and else remains unchanged at the level of $n(\Omega_i)$. These curves qualitatively agree well with the measured susceptibilities, verifying our interpretation. In combination, these measurements indicate that the active phase is very susceptible to perturbations in system parameters, returning the state of the system to a critical state by particle loss, in agreement with the SOC mechanism.

Conclusion

In this chapter we probed the driven-dissipative dynamics of Rydberg spin systems with competing facilitation and dissipation, uncovering a regime of self-organised criticality for strongly driven facilitation. Our system exhibits all building blocks of SOC, including microscopic processes braking detailed balance and leading to an absorbing state phase transition in the absence of particle exchange with an external reservoir, and a separation of timescales between the fast internal dynamics of the Rydberg spin system and slow seed excitation as well as particle loss. Our experimental platform does not include particle addition, such that the SOC regime only emerges for sufficiently strong driving and high initial densities corresponding to the active phase of the absorbing state phase transition. Slow external driving by particle addition during the system evolution could be implemented in future experiments. Our driven-dissipative system also does not obey energy conservation, whose importance for SOC is controversially debated [248, 71], but violated in many important model systems with conjectured SOC, like forest fire models [249] and earth quake models [250, 63], or the reported observation of SOC in the response of neuronal networks to external stimulation [70, 72]. Rydberg spin systems are, unlike many natural systems for which SOC has been conjectured, governed by well-known microscopic details and are accessible to investigation and manipulation in both laboratory experiments and theoretical modelling. This will allow us to quantitatively compare our experimental observations to microscopic models like the classical master equation (cf. sec. 3.4.2) in the future. This will also help us establish the universality class of the SOC process in our system. Due to the long-range van der Waals interactions between Rydberg excitations it is promising to introduce a coarse-grained description of our system, enabling one to compare our system to similar models for which SOC has been conjectured, like forest fire models or earth quakes on an equal basis. Thus Rydberg spin systems have the potential of shedding light on conjectured critical properties of complex natural systems and whether these can be understood in terms of the discussed rather simple SOC mechanism. Naturally, more work needs to be done to explore the different aspects of SOC in Rydberg spin systems. Future experiments will also be dedicated to elucidating the dynamics of the approach to the critical state, for which we observed a peculiar slowdown in loss rate, and to observe the spatio-temporal correlations of the critical avalanche dynamics. Furthermore, it would be interesting to verify in more detail that the instability marks the common phase boundary of the early and late time dynamics and to explore possible connections between the scaling behaviour of the particle loss rate R in the number conserving limit and the behaviour of the steady state density n_f. Our work establishes ultracold Rydberg atoms as a platform for simulating absorbing state and SOC phenomena in classical settings, with the potential to extend this concept to quantum coherent evolution [50, 51, 135].

Conclusions and Outlook

7

In this thesis, we have explored both in experiment and theory the non-equilibrium dynamics and phase structure of driven-dissipative Rydberg spin systems. At the onset of our explorations we posed two guiding questions:

> How can the dynamics and phase structure of a non-equilibrium system be measured and characterised?
>
> How do the dynamics and phase structure emerge from the microscopic processes of the many-body system?

In the following, we will first summarise our experimental approach and its theoretical underpinnings for addressing these questions and then recapitulate our findings.

The studies presented in this thesis were made possible by a completely new experimental apparatus based on ultracold trapped ^{39}K atoms laser-coupled to highly-excited Rydberg states. This setup, introduced in chapter 2, was designed to reach versatile Rydberg excitation, covering ns, np and nd Rydberg states as well as a broad range of principle quantum numbers n, with both single-photon and two-photon coupling. Furthermore, the setup allows for strong many-body interactions, widely tunable experimental parameters like driving strength, laser detuning and atom density, and long excitation times compatible with timescales of many-body dynamics of the internal states and atomic motion. These capabilities provide us with the means to control the population of the addressed Rydberg state in each experiment, as well as the resulting interaction and dissipation properties of the system. A further strength of our approach lies in our control of couplings to the environment. The ultrahigh vacuum system shields the atom cloud from coupling to the room-temperature environment except for thermal blackbody radiation, creating a largely thermally isolated quantum system. As we describe in chapter 3, each atom can be conveniently described as a pseudo-spin 1/2 quantum system comprising the atomic ground state and a specific Rydberg state, which is isolated by the excitation laser within the manifold of states of each atom. Therefore our experimental platform emulates a quantum spin system which is driven by the external laser driving, is dissipative due to the finite lifetime of Rydberg states, and possesses strong interparticle interactions due to the long-range van der Waals interaction of Rydberg states. This places the system firmly in a setting of competing interactions, driving and dissipation, which we showed in our experiments gives rise to a rich non-equilibrium phase structure. The microscopic properties of our system can all be captured by a quantum master equation, from which we derived approximate models to describe the many-body behaviour: a dissipative mean field model with Rydberg blockade correlations which can be solved analytically, and a classical master equation which allowed us to efficiently simulate many-body systems including system details like atom trapping and atomic motion. This combination of experiment and theory allowed us in the following to draw qualitative and quantitative connections between macroscopic experimental observations and the underlying microscopic processes.

To identify good conditions for experiments, characterised by strong interactions, long coherence times and weak dissipation, and to access the effects of spontaneous decay of short lived intermediate states populated in two-photon excitation, we first theoretically investigated the interaction and dissipation properties for the minimal system of two atoms in chapter 4. Since both the effective dissipation and interaction strengths arise from the population of the Rydberg state, weak Rydberg dressing has been proposed as a means to enhance the coherence times of the system to timescales of atomic motion. In this scheme, a small and tunable population of excited states is created by far off-resonant laser driving ($|\Delta| \gg \Omega,\ \Gamma$). Additionally, the resulting effective interaction potential shows an unusual soft-core behaviour. [202, 207, 138] However, an open question at the time was whether it is possible to achieve long coherence times and strong interactions at the same time for three level (i.e. two photon) excitation, because the coupling to short lived intermediate states leads to unavoidable decay and decoherence [138]. Through careful analysis of solutions of the quantum master equation for such systems, we were able to establish that the desired conditions can be achieved by exploiting multiphoton coherences, namely electromagnetically induced transparency and a cooperative multiphoton resonance. For sufficiently strong coherent driving on the upper transition ($\Omega_r \gg \Gamma_e$) this optimised three-level dressing scheme allows for the creation of sufficiently strong soft-core interaction potentials on par with what can be achieved via two-level dressing. Additionally, we found that the effective dissipation rate becomes distance-dependent, exhibiting a soft-core shape similar to the interaction potential. To reach regimes where interaction strengths become comparable with motion with the optimised three-level dressing scheme requires driving strengths on the upper transition which are unavailable in our experimental setup, due to the limited achievable laser power. However, for so called "inverted" three-level dressing via higher intermediate states [161] sufficiently strong laser sources for the upper transition are available, which will make optimised three-level dressing with strong interactions and small decoherence rates available in the future.

We then turned to experimentally investigating many-body effects in atomic Rydberg gases in chapters 5 and 6. Employing our ability to reliably create, manipulate and probe atomic gases coupled to Rydberg states, we explored the non-equilibrium dynamics and phase structure of driven-dissipative quantum spin systems. We discovered that the particle loss inherent to our system (e.g. by hyperfine ground states decoupled from the Rydberg excitation or by photoionisation) provides a powerful tool for observing the state and evolution of our system across many orders of magnitude in excitation time and Rydberg excitation density. This became the main experimental tool for the observations of many-body spin dynamics reported in this thesis, covering excitation times ranging in total from $t = 30\,\mu s$ to $150\,ms$, which goes far beyond typical natural lifetimes of Rydberg states $\sim 100\,\mu s$, as well as four orders of magnitude in Rydberg fraction. Investigating the particle loss dynamics, we found that for times short compared to the inverse particle loss rate R^{-1}, particle loss is well described by an exponential decay governed by R, but which otherwise constitutes a small perturbation to the state and dynamics internal to the coupled spin-1/2 system. We refer to this limit of the temporal evolution of the spin system as the particle-number conserving limit, and to longer times, where particle loss influences the evolution of the spin system, as not particle number conserving. In chapter 5 we used the particle loss rate as a measurement tool to determine the different regimes of non-equilibrium behaviour of driven-dissipative Rydberg spin systems in the particle-number conserving limit and to map out the non-equilibrium phase diagram of

these regimes. Thereafter we observed the particle loss dynamics on even longer timescales in chapter 6, where we found that the interplay between internal state dynamics and particle loss to external states leads to a new regime of non-equilibrium behaviour which we identified as self-organised criticality.

In chapter 5 we were able to unravel the non-equilibrium phase structure of the driven-dissipative Rydberg spin system and to identify its different regimes of dynamical behaviour. Investigating the particle loss rate R we found, to our surprise, that it exhibits powerlaw scaling as a function of the driving strength (Ω^α), with exponents that depend on the strength and detuning of the external driving laser field. In conjunction with theoretical modelling we could then show that these exponents are characteristic of the different regimes of behaviour of the system. Close to resonance, the established phase structure comprises a dissipation dominated regime for weak driving characterised by $\alpha \approx 2$, and a critical regime for sufficiently strong driving with a measured scaling exponent $\alpha = 1.185(25)$. Far from resonance we observed paramagnetic regimes for positive and negative detunings and weak driving characterised by small Rydberg fractions and scaling exponents $\alpha \approx 2$, while for strong driving we observed a crossover to the critical regime even for large detunings. For large detunings and strong facilitation (at positive detunings for the repulsive interactions realised in our system) we additionally found an instability separating paramagnetic and critical regimes with an amplified scaling exponent $\alpha > 2$. A complete coverage of all of the different regimes of behaviour and their classification had not been achieved before, neither experimentally nor theoretically.

To understand the origin of the observed regimes and their characteristic scaling behaviour we employed the theoretical microscopic models developed in chapter 3. The mean field model can be solved analytically and therefore allowed us in a first step to associate the different regimes to the respective dominant energy scale, and to elucidate the nature and characteristic scaling exponents of the different regimes. The mean field model does not reproduce the observed instability, instead suggesting bistable behaviour. To go beyond the mean field approximation and to include additional experimental details we employed classical rate equation simulations, which are surprisingly well suited for describing our experiments because the excitation times are long compared to the timescale of dephasing (e.g. due to laser phase noise). These simulations confirmed the mean field scaling behaviour in homogeneous systems, reproduced the observed instability, and allowed us to include atomic motion as well as inhomogeneous density and light shift distributions due to the dipole trap potential. With this approach we were able to quantitatively reproduce the measured scaling exponents as well as the positions of the regimes within the non-equilibrium phase diagram.

Through the combination of experiment and theory we could shed light on the different mechanisms leading to the observed phase structure and to distinguish single-body regimes from regimes with emerging many-body behaviour. For example, we determined that the dissipation dominated regime and the paramagnetic regime share the same exponent $\alpha = 2$, since the driving strength can be considered small compared to the dissipation rate or the detuning, resulting in small Rydberg excitation densities and single-body behaviour. In contrast, for strong driving in the critical regime collective Rydberg blockade due to the long-range Rydberg-Rydberg interactions leads to a collective enhancement of the driving strength ($\sqrt{N}\Omega$). The characteristic scaling exponent of the critical regime is $\alpha = 2/5$ [201], which averaging over the inhomogeneous atom cloud in the dipole trap increases to the scaling exponent $\alpha \approx 1.2$ in our simulations, confirming our experimental

measurements.The measured critical scaling reveals that in this regime the behaviour of the system is governed by the critical properties of an underlying equilibrium phase transition at $\Omega,\ \Delta = 0$, despite the dissipation inherent to our system. Surprisingly, te observed crossover from dissipation dominated to the critical regime occurs for driving strengths much lower than the effective dissipation rate, due to the collectively enhanced driving strength ($\sqrt{N}\Omega_{\mathrm{th}} \approx \sqrt{\Gamma(\Gamma + \gamma_{\mathrm{de}})}$), which is a direct consequence of the long-range character of the Rydberg-Rydberg interactions. In our system, the dissipative regime, and the paramagnetic regime above resonance, as well as the associated instability towards larger driving strengths, are features without counterparts in the equilibrium phase structure, which highlights the importance of dissipation competing with driving and interactions for the non-equilibrium (ground state) phase structure of the corresponding quantum Ising model. Additionally, we showed in chapter 6 that the observed phases and dynamical behaviour are quite robust and insensitive towards microscopic details. For example, we have performed experiments using both one-photon and two-photon excitation schemes, ns and np Rydberg states that exhibit very different interaction properties, and different principal quantum numbers, but observed the same regimes of behaviour. As a result, we are confident that scaling laws will serve as a valuable tool for identifying and classifying new regimes of other driven-dissipative quantum systems.

Some of the features observed in the non-equilibrium phase structure can also be recognised in other works. The powerlaw scaling on resonance and off-resonance might also be present in [116], but was not discussed there. For driving above resonance, the instability caused by facilitated excitation processes was identified as a regime of large fluctuations (bimodal counting statistics) in [117] separating a regime of low and one of high Rydberg excitation density. However, powerlaw scaling reported in this thesis is a newly observed feature of these dynamics. We would like to further point out that also in their work a transition from low to high excitation density was observed on resonance as a function of driving strength.

In chapter 6 we extended our explorations to the full time dynamics beyond the particle-number conserving limit arising from the interplay between particle loss and the internal dynamics of the spin system. Here we focussed on laser driving conditions with large detuning, where we observed unstable behaviour in the particle-number conserving limit. We found that the system exhibits strikingly nonlinear dynamical evolution comprising two regimes of behaviour. For small driving strengths or small initial densities we found the dynamics consists of a slow exponential loss for all times that is linked to the paramagnetic state, while at large driving strengths the temporal dynamics consists of a relatively fast initial loss of atoms breaking off at a steady state with an effectively constant and non-zero particle density, despite the non-negligible particle loss. We showed that the steady-state density is independent of the initial density and follows a powerlaw as a function of the driving strength $n_f \propto \Omega^{-\beta}$ with scaling exponent $\beta = 1.76(2)$. Our observation that the system drives itself to the same final density independent of the initial density, combined with the powerlaw dependence with the driving strength, leads us to conclude that self-organised criticality is the underlying mechanism governing this peculiar dynamics. This remarkable conclusion is consistent with the "ingredients" conjectured to lead to SOC, which are microscopic processes leading to an absorbing-state phase transition, and slow external driving and slow particle loss driving the system to the critical state of this phase transition [248, 71]. Further studies are needed to corroborate this discovery and to clarify the nature of the absorbing state phase transition, for which directed percolation is a

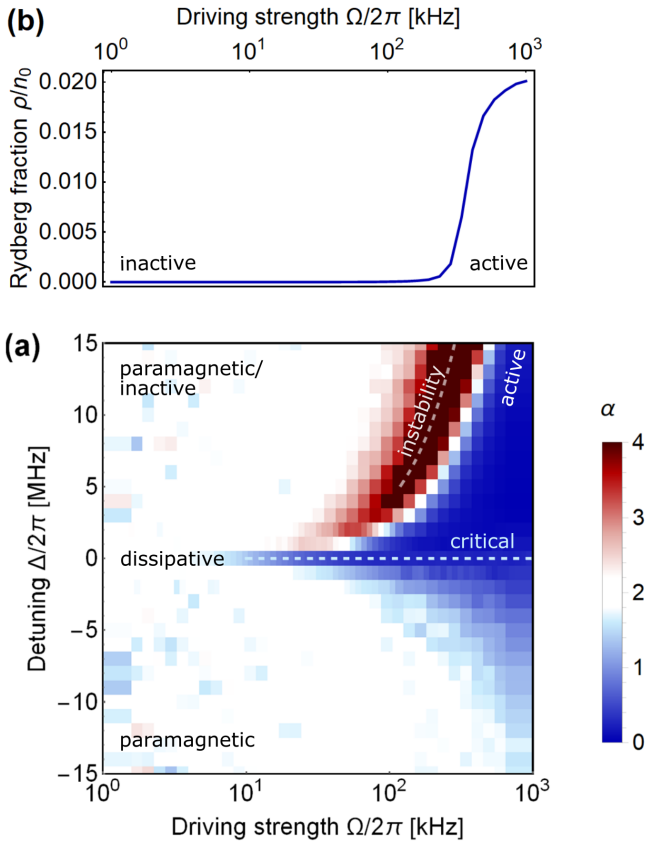

Figure 7.1: Identified features associated to critical many-body states in driven-dissipative Rydberg spin systems. The given phase diagram was obtained by classical rate equation simulations assuming a static, disordered and homogeneous distribution of atoms in a box with periodic boundary conditions, particle number conservation and system parameters close to chapter 5. (a) We show the calculated scaling exponents α as a function of driving strength (Ω^α). White indicates $\alpha = 2$ scaling which is characteristic of weakly excited single-body regimes, which are dissipation dominated on resonance and paramagnetic off-resonance. On resonance we observe critical scaling $\alpha < 2$ associated to an equilibrium quantum phase transition (light blue dashed line). For large positive detunings the facilitation condition is met, giving rise to the instability ($\alpha > 2$, light red dashed line), which in the far detuned limit denotes the phase boundary between an inactive and an active phase. We show the transition between these two phases in panel (b) for the Rydberg fraction, which is the normalised Rydberg excitation density. Including particle loss, the system in the active phase self-organises to the critical point of the absorbing state phase transition.

likely candidate [14, 248, 49, 48]. First signatures of an absorbing-state phase transition in driven-dissipative Rydberg spin systems with a large particle reservoir were reported in experiments by [51]. They were also unable to clearly identify the universality class of the phase transition, although their results are consistent with directed percolation in one spatial dimensions. The surprising identification of SOC highlights driven-dissipative Rydberg spin systems as a laboratory analogue for experimentally exploring complex non-equilibrium phenomena, which is accessible to both experiments and theory.

Combining the results of chapters 5 and 6, we have extensively addressed our guiding questions and explored the non-equilibrium phase structure and dynamics of driven-dissipative Rydberg spin systems by identifying suitable experimental observables to characterise the various regimes of behaviour, and by relating the macroscopic behaviour to microscopic models. In Figure 7.1 we illustrate everything we have learned about the non-equilibrium phase structure as a function of the driving strength and detuning, using a phase diagram for an idealised static and homogeneous system obtained by a classical rate equation simulation. We assumed particle number conservation and system parameters close to the experiments in chapter 5. Analogously to our experiments we plot the scaling exponent α as a function of the driving strength. Figure 7.1 nicely illustrates the presence of two types of criticality at work in one system, that arise from very different mechanisms. The associated regimes arise for strong laser driving, with the system parameter distinguishing between the two being the laser detuning. The critical regime close to resonance (light blue dashed line) is governed by an equilibrium quantum critical point at $\Omega,\ \Delta = 0$, despite the dissipation inherent to our system. Far above-resonance, where facilitated excitation and decay govern the system dynamics, an absorbing state phase transition between inactive and active phases arise in the absence of particle loss (Fig. 7.1(b)). The non-equilibrium critical point of this phase transition is given by the instability observed in our experiments (light red dashed line). For late times of the system dynamics, SOC emerges as a mechanism driving the system to the critical point of this absorbing-state phase transition. Our results show that in driven-dissipative systems a variety of critical phenomena associated to different mechanisms can arise.

The work presented in this thesis opens up a variety of research avenues, concerning the properties and nature of the SOC dynamics, the interplay between quantum coherent and dissipative dynamics, as well as potential novel phases of synthetic non-equilibrium quantum systems with engineered microscopic details. Future experiments on SOC in Rydberg spin systems could focus on observing other properties of the critical dynamics, for example the distribution of critical avalanche sizes, which is expected to follow a powerlaw distribution. Furthermore, experiments could try to access spatial and temporal correlations using direct high-resolution imaging of the Rydberg excitations in an optical lattice [148, 149]. A further detection technique complementary to our absorption imaging and suitable to observing avalanches of Rydberg excitations is counting of the ions created by photoionisation [116, 51, 121]. Both high-resolution imaging (using the implemented in-vacuum high-resolution objective lens) and ion detection (using the in-vacuum electrode structure and microchannel plates) are possible with our apparatus as discussed in chapter 2. Additionally, systematic effects of the inhomogeneous density and lightshift distributions associated to our optical dipole trap, which we found to influence measured scaling exponents, can be reduced by atom trapping in box-like trapping geometries [251], or pulsed excitation where the trapping potential only is on between excitation pulses. We expect that following this route, Rydberg spin systems will allow one to shed light on the surprising abundance of phenomena with powerlaw distributed observables in nature, for which SOC has been conjectured as an organising mechanism [59, 71, 246, 70]. Beyond the simulation of effectively classical phenomena, our experiments also have the potential of opening up the path to studying the crossover from classical many-body dynamics to dynamics dominated by quantum fluctuations. Upon further reducing the laser linewidths and effects of the atomic motion (e.g. by pinning the atoms in an optical lattice), this would allow one to study for example largely unexplored first order absorbing state phase

transitions predicted in [50, 51, 135]. If it becomes possible to extend coherence times to timescales comparable to atomic motion and equilibration, one can explore novel types of quantum fluids enhanced by Rydberg-dressed interactions. The resulting soft-core interaction potential opens the possibility of creating novel non-equilibrium phases of matter [85, 104]. Our extensions to Rydberg dressing concepts to include dissipation self-consistently in chapter 4 uncovered distance-dependent dissipation for two-photon Rydberg dressing, which may find additional applications in quantum state engineering via dissipation [229] or novel cooling techniques [169, 230, 231].

Finally, the work reported in this thesis more generally reflects an explosion of interest in the last years in quantum systems far from equilibrium, spanning a variety of physical platforms. The momentum in this field is to a large part based on the ability to control and engineer a large, ever increasing range of properties of synthetic quantum systems, and the possibility to comprehensively describe these systems microscopically. We expect that the findings reported in this thesis, especially powerlaw scaling and the identification of genuine non-equilibrium critical behaviour, will transcend far beyond Rydberg spin systems and are applicable in diverse non-equilibrium scenarios. Non-equilibrium settings lead to a diverse host of complex many-body phenomena - we have just begun to open the door to understanding and exploiting all the richness non-equilibrium has to offer, with a room full with new surprises ahead!

Acknowledgements

As is so often the case in life, my research and this thesis were made possible and shaped by many different people. I would like to dedicate the next lines to thank all the people who have contributed in a multitude of ways to this work.

First and foremost, I would like to express my sincerest gratitude to my supervisor, Shannon Whitlock. Not only has he provided me with the opportunity of diving deep into the world of research, but he was always available with invaluable ideas, experience and guidance. Oftentimes he was the cornerstone I and the group could rely on in times of trouble. And he even shared all his secret tricks in the lab and with Mathematica with us.

I also would like to thank Thomas Gasenzer for kindly agreeing to review this thesis.

It has been my great pleasure to work in a fantastic team with various members over the years. We have, together, built an experimental apparatus from scratch and spent uncountable days in the lab constructing and honing *our* machine. This was in many ways an unforgettable experience. I honestly believe that without them, I would not have succeeded in my PhD. So thank you Alda Arias, Graham Lochead, Tobias Wintermantel, Henrik Hirzler, Nils Pehoviak, Philipp Fabritus, Guilia Faraoni, Silva Mežinska, Christoph Hofmann, the Sayer brothers, Christoph Schweiger, and all the other guys! They were a fabulous company during many days spent in the office and the lab and added to our experiment and our research in innumerable ways.

First of all I would like to single out and thank Alda Arias, my fellow PhD candidate in our team for many years. Only when she joined we became a team in full, including group breakfasts, Reggaeton music playing in the lab and many lively discussion about physics and life. Even beyond that, she bested LabView and the Rydberg excitation lasers!

I would also like to give special thanks to Graham Stuart Lawrence "Percival" Lochead, whom I valued highly for bringing good old English humour into our group, English tea, and most importantly a wealth of knowledge and experience. I deeply enjoyed our many discussions, and I am very grateful for your input and caring support in conducting our research and in preparing this thesis.

The work presented here would not have been possible without additional collaborators, of whom I am probably most indebted to the other ultracold atoms groups at the Physics institute. These are the groups of Selim Jochim, Jian-Wei Pan, and the mixtures, Rydbergs and ions groups of Matthias Weidemüller, who lend many spare components of their experiments to us, which greatly accelerated the assembly of our own machine. Especially I would like to thank the Rydberg team from the beginning of my PhD, who shared much of their experience and designs of central components of their experiment with us. Furthermore, I am much obliged to Michael Buchhold from Caltech. He has been able to provide many insights into the interpretation and understanding of our research on self-organisation and made connections we were unaware of. Even more so, he was almost always available for discussions, patiently providing explanations and building bridges between the mindsets of theorists and experimentalists. Furthermore, I would like to thank

Jürgen Berges and Asier Piñiero Orioli for insightful and inspiring discussions.

A big 'Thank You' also goes to the workshops of our institute. Their ample, high-quality support in building key mechanical and electronic components of our experiment was invaluable in the successful construction of our experiment. Without their work our research would have not been possible. Especially Ralf Ziegler, the head of the mechanical workshop, could find a solution to almost any problem we came up with. I additionally would like to thank our secretary Claudia Krämer, who is the secret backbone of our research division.

Personally, I would not have been able to conduct my PhD without the financial support awarded by the Carl Zeiss Foundation for a full three years and bridging funds from the Heidelberg Graduate School of Fundamental Phyiscs. Beyond financial matters, both organisations provided an insightful framework for my PhD with fun events along the way. I am most grateful to both organisations for their generous support.

Finally, I would like to thank those people who walked the path of this thesis with me in friendship and kindness. I would like to thank those truly life-giving people, whom I was allowed to lean on in dire or stressful times and with whom I shared many gorgeous experiences, like Ann-Kristin Oßa, Etienne Perrier, Dorle, Merlin and Ragnar Polivka, Frauke Martin, Simon Krummradt, Judit Beck and her family, Sebastian Isbaner, David Schönleber and his wife, Sebastian Heupts and his family, and *of course my beloved parents.*

Appendix: Motional enhancement of the facilitated excitation probability

A

The following appendix is based on the following manuscript, from which the text is reproduced verbatim with permission by the American Physical Society:

Uncovering the non-equilibrium phase structure of an open quantum spin system
S. Helmrich, A. Arias and S. Whitlock
submitted to Physical Review X

For the long times relevant for our experiments, atomic motion can play a significant role in the excitation dynamics, especially for $\Delta > 0$. The dominant effect is that, compared to the case of static disorder, motion enables a greater fraction of atoms to meet the resonance condition at the faciliation distance $r_{\mathrm{fac}} = (C_6/\Delta)^{1/6}$ and to undergo Landau-Zener transitions.

To account for this motion enhanced excitation probability in the RE simulations we derive an expression for the probability to excite an atom from its ground state while it moves with velocity v relative to a pre-excited Rydberg atom. Their separation r is treated as a classical parameter, while the excitation dynamics of the ground-state atom is described by the quantum master equation (eq. 5.1), which includes decay and dephasing terms and an effective position dependent detuning $\Delta - V(r)$. Figure A.1(a) shows examples of the time-dependent excited state probability assuming the two atoms start at the same initial position ($r = 0$) and move apart as a function of time, for parameters similar to the experiment and for three different detunings. After the atom crosses the facilitation distance (indicated by gray vertical lines in Figure A.1(a) for each detuning), the excitation probability peaks and undergoes oscillatory dynamics which are damped due to spontaneous decay and dephasing. The peak excitation probability is much larger than the off-resonant (static) probability and, depending on the relative velocity of the atoms, can be a sizable fraction of the maximum on-resonant probability (Fig. A.1(b)).

For the experimental parameters assumed, the typical crossing time is comparable to the dissipation rate making an analytic treatment difficult. However, by inspecting the numerical simulations we found that the peak excitation probability P_{LZ} is well described by a heuristic model which incorporates the usual Landau-Zener transition probability P^0_{LZ} with a cut-off given by the static resonant excitation probability f_R, according to:

$$P_{\mathrm{LZ}} = \left(\frac{1}{f_R} + \frac{1}{P^0_{\mathrm{LZ}}} \right)^{-1} \tag{A.1}$$

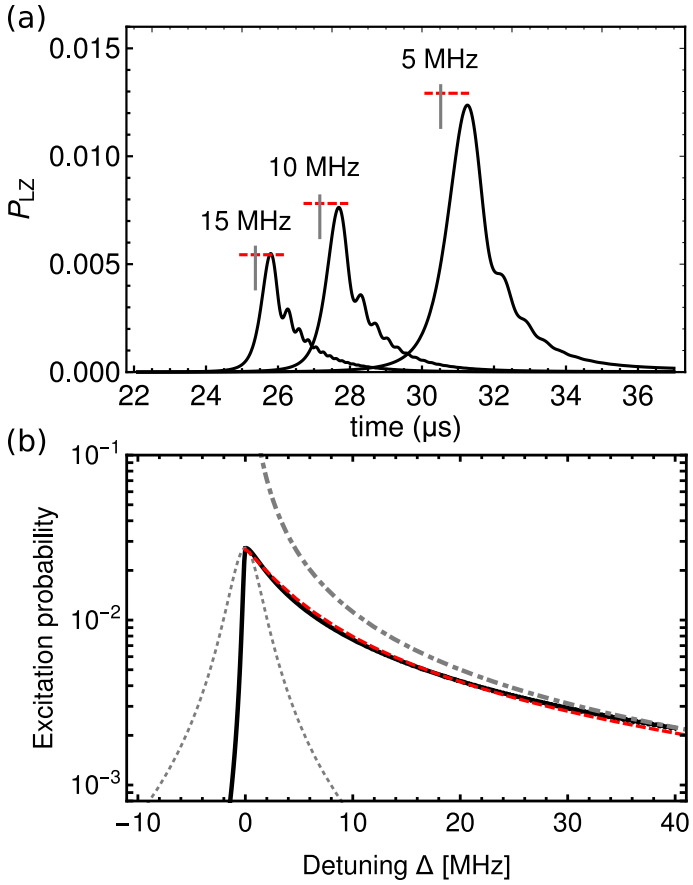

Figure A.1: Landau-Zener transition probability for an atom moving away from a Rydberg excitation with a velocity of 0.2 m/s. (a) transient excitation dynamics for three different detunings. The dashed red horizontal lines show the analytic approximation (see text) and the vertical gray lines mark the time at which the atom reaches the facilitation shell for each detuning. (b) Peak excitation probability as a function of detuning. The solid black line shows the full numerical simulations, the red dashed line is the modified Landau Zener theory including dissipation (Eq. (A.1)), the dash-dotted line is the usual Landau-Zener result neglecting dissipation and the dotted line is the steady state Rydberg fraction assuming static atoms.

where

$$P_{\mathrm{LZ}}^{0} = 1 - \mathrm{e}^{-2\pi(\Omega/2)^2/|\dot{\delta}|}, \quad f_R = \left.\frac{\Gamma_\uparrow}{\Gamma_\uparrow + \Gamma_\downarrow}\right|_{V=-\Delta} \tag{A.2}$$

and $\dot{\delta} = v(dV/dr) = -6v\Delta^{7/6}/C_6^{1/6}$ is the slew rate of the Landau-Zener energy level crossing evaluated at the facilitation distance (assuming van der Waals interactions). Fig. A.1(b) shows a comparison of the peak excitation probability for the modified Landau-Zener probability P_{LZ} (dashed red line) and the full numerical simulation of the time-dependent master equation (solid black line) alongside the bare excitation probability without motional enhancement (dotted gray line) and the usual Landau-Zener result without dissipation (dash-dotted gray line). For $\Delta/2\pi \gtrsim 5$ MHz the motion-enhanced excitation probability is more than an order of magnitude larger than the excitation probability without motion.

So far, this treatment does not include the probability that a given atom actually undergoes a Landau-Zener crossing, which depends on it's initial position and velocity as well as the lifetime of the Rydberg state. To account for this we assume a Maxwell-Boltzmann velocity distribution characterised by a thermal velocity $v_{\rm th} = (2k_BT/m)^{1/2}$. For the experimental parameters, the distance the atoms move during the excited state lifetime is small compared to the facilitation distance. Therefore it is sufficient to use a one-dimensional model in which the facilitation shell is treated as a planar boundary at $x = x_{\rm fac}$. After integration we find that the probability for a given atom with initial position x_j to cross the boundary within the time t is:

$$\mathcal{P}_{\rm cross} = \frac{1}{2}{\rm erfc}\left(\frac{|x_{\rm fac} - x_j|}{t\, v_{\rm th}}\right). \tag{A.3}$$

To account for the possibility that the Rydberg atom decays before the boundary is reached, we time-integrate the crossing probability weighted by an exponential decay

$$\begin{aligned} P_{\rm cross} &= \frac{\int_0^\infty \mathcal{P}_{\rm cross} {\rm e}^{-2\pi\Gamma t} dt}{\int_0^\infty {\rm e}^{-2\pi\Gamma t} dt} \\ &\approx \frac{1}{\sqrt{3}} \exp\left(-3\xi^{2/3}\right) \end{aligned} \tag{A.4}$$

where in the last step we use an approximation to the MeijerG special function for $\xi = \pi\Gamma|x_{\rm fac} - x_j|/v_{\rm th} > 0$ which is accurate within 14%.

To incorporate this model into the RE simulations we modify equation (5.12) according to $\Gamma_\uparrow \to \Gamma_\uparrow + \Gamma P_{\rm LZ} P_{\rm cross}$, substituting $x_{\rm fac} \approx (C_6/\Delta)^{1/6}$ and $x_j \approx (C_6/V_j)^{1/6}$. Generally, this prescription underestimates the effect of motion as it doesnt include forces between the atoms or the possibility that there are multiple Rydberg excitations in the viscinity of a given atom. For the results shown in Fig. 3, we find best agreement with the data assuming $P_{\rm cross}$ is four times larger than the expression given in equation (A.4).

Appendix: Calibration of the driving strength by Ramsey spectroscopy

B

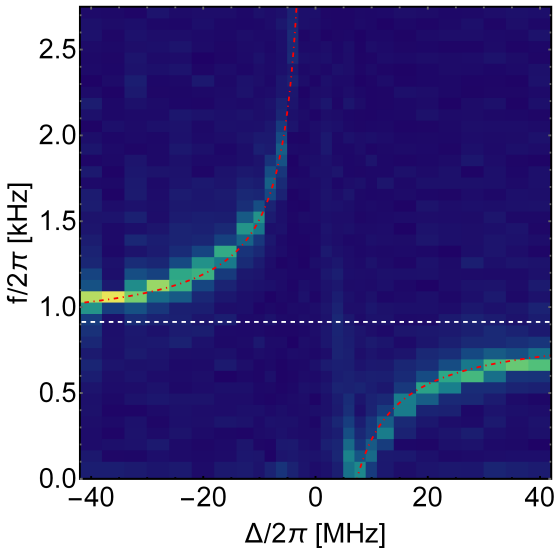

Figure B.1: Calibration of the driving strength of Rydberg excitation by Ramsey interferometry spectroscopy. Ramsey oscillations between two hyperfine ground states are measured in time, while they are coupled to the Rydberg state by a single laser field. The Fourier spectrum with frequency f is determined for a range of laser detunings, showing a peak at the frequency of the respective lightshift induced by the Rydberg laser. The spectrum is offset by 900 Hz here (white dashed line), which is the bare detuning of the Radio frequency field coupling the two hyperfine ground states. The laser driving strength obtained in this measurement is $\Omega/2\pi = 170\,\mathrm{kHz}$.

To calibrated the driving strength Ω of the single-photon Rydberg excitation, we measure the induced lightshift experienced by ground state atoms. To this end we implement Ramsey interferometry spectroscopy [252, 211] between the two hyperfine ground states $|4s_{1/2}, F = 1, m_F = 0\rangle$ and $|4s_{1/2}, F = 2, m_F = 0\rangle$. We drive the magnetic dipole transition between these two states with a radio-frequency (RF) antenna inside the vacuum chamber (see Fig. 2.1). This transition is insensitive to magnetic fields, and the differential light shift due to the dipole trap is negligibly small, making it suitable to measure lightsifts originating from the Rydberg excitation laser. The Ramsey sequence is based on a $\pi/2$ pulse creating an equal superposition between the two coupled hyperfine ground states, a subsequent free coherent evolution time t and a final $\pi/2$ rotation to close the interferometer. Then, the population in the $F = 2$ state is measured as a function of t, which we measure from

zero to 15 ms. The measured population oscillates in time with an oscillation frequency f given by the total difference frequency of the RF field relative to the addressed hyperfine transition. This difference frequency is a combination between the known RF detuning and the additional lightshift induced by the Rydberg excitation laser. Hence this lightshift is revealed as a peak in a Fourier spectrum of the measured oscillations, which we show in Figure B.1. The RF detuning was set to 900 Hz, indicated by the white dashed line. The lightshift of the Rydberg excitation laser was measured by coupling to the $F = 2$ ground state with laser detunings ranging from -40 to 40 MHz. This detuning range is much smaller than the ground state hyperfine splitting, such that the laser coupling to the $F = 1$ ground state can be neglected in the following. Furthermore, the RF driving strength is much smaller than the driving strength of the Rydberg excitation laser, such that lightshifts due to RF driving are negligible. Hence the lightshift induced on the $F = 2$ state is fully determined by the Rydberg excitation laser (parameters Ω and Δ), leading to the observed Autler-Townes spectrum of the form $(\Delta \pm \sqrt{\Delta^2 + \Omega^2})/2$ in Figure B.1. From this measurement we determine the Rydberg laser driving strength to be $\Omega/2\pi = 170$ kHz. To avoid interaction-induced lightshifts in this measurement we used low atom densities. The measured driving strength can be directly related to the applied optical power P of the Rydberg excitation laser to create a Rabi frequency calibration $\Omega/2\pi = a\sqrt{P}$. We measure P for every individual data point on a photodiode to account for potential drifts in the laser power on timescales much larger than the experimental cycle. With the driving strength calibrated by the effected light shift on an atomic transition, the biggest systematic uncertainty of the driving strength measurement is small drifts of the cloud position relative to the focus of the excitation laser on timescales of several hours. We estimate that such drifts are smaller than the Rayleigh range of the focus of the excitation laser and therefore lead to only small drifts in the resulting driving strength of the addressed atomic transition. Based on the shot-to-shot fluctuations of measured optical powers we estimate that the relative statistical error of the driving strength is 0.2 %.

Bibliography

[1] Victor Gurarie. Quantum Phase Transitions Go Dynamical. *APS Physics Viewpoint*, 10(Ii):22–25, aug 2017. URL: http://arxiv.org/abs/1609.08482, arXiv:1609.08482, doi:10.1103/Physics.10.95.

[2] P. W. Anderson. More is different. *Science*, 177(4047):393–396, 1972. URL: http://science.sciencemag.org/content/177/4047/393, arXiv:http://science.sciencemag.org/content/177/4047/393.full.pdf, doi:10.1126/science.177.4047.393.

[3] H. Haken. Synergetics - Are cooperative phenomena governed by universal principles? *Naturwissenschaften*, 67(3):121–128, 1980. URL: https://doi.org/10.1007/BF01073611, doi:10.1007/BF01073611.

[4] Elbio Dagotto. Complexity in Strongly Correlated Electronic Systems. *Science*, 309(5732):257 LP – 262, jul 2005. URL: http://science.sciencemag.org/content/309/5732/257.abstract.

[5] Michael Cross and Henry Greenside. *Pattern formation and dynamics in nonequilibrium systems*. Cambridge Univ. Press, Cambridge [u.a.], 2009. URL: http://dx.doi.org/10.1017/CBO9780511627200.

[6] Lawrence Wilets. Shape of the nucleus. *Science*, 129(3346):361–367, 1959. URL: http://science.sciencemag.org/content/129/3346/361, arXiv:http://science.sciencemag.org/content/129/3346/361.full.pdf, doi:10.1126/science.129.3346.361.

[7] Bogdan Povh, Klaus Rith, Christoph Scholz, and Frank Zetsche. *Geometric Shapes of Nuclei*, pages 53–71. Springer Berlin Heidelberg, Berlin, Heidelberg, 2004. URL: https://doi.org/10.1007/978-3-662-05432-1_5, doi:10.1007/978-3-662-05432-1_5.

[8] Wilson Poon, Tom McLeish, and Athene Donald. Soft condensed matter: where physics meets biology, 2018. URL: https://physicsworld.com/a/soft-condensed-matter-where-physics-meets-biology/.

[9] D. S. Riggs. *Quantum Optics*. Cambridge University Press, 1970.

[10] Mark Buchanan. Bead Chains Impersonate Polymer Molecules. *Physics*, 11:20, feb 2018. URL: https://link.aps.org/doi/10.1103/Physics.11.20, doi:10.1103/Physics.11.20.

[11] Simone Napolitano. *Non-equilibrium Phenomena in Confined Soft Matter*. Springer, Cham, Switzerland, 2015.

[12] M. McDonald, M. Bayliss, B. A. Benson, R. J. Foley, J. Ruel, P. Sullivan, S. Veilleux, K. A. Aird, M. L.N. Ashby, M. Bautz, G. Bazin, L. E. Bleem, M. Brodwin, J. E. Carlstrom, C. L. Chang, H. M. Cho, A. Clocchiatti, T. M. Crawford, A. T. Crites, T. De Haan, S. Desai, M. A. Dobbs, J. P. Dudley, E. Egami, W. R. Forman, G. P. Garmire, E. M. George, M. D. Gladders, A. H. Gonzalez, N. W. Halverson, N. L. Harrington, F. W. High, G. P. Holder, W. L. Holzapfel, S. Hoover, J. D. Hrubes, C. Jones, M. Joy, R. Keisler, L. Knox, A. T. Lee, E. M. Leitch, J. Liu, M. Lueker, D. Luong-Van, A. Mantz, D. P. Marrone, J. J. McMahon, J. Mehl, S. S. Meyer, E. D. Miller, L. Mocanu, J. J. Mohr, T. E. Montroy, S. S. Murray, T. Natoli, S. Padin, T. Plagge, C. Pryke, T. D. Rawle, C. L. Reichardt, A. Rest, M. Rex, J. E. Ruhl, B. R. Saliwanchik, A. Saro, J. T. Sayre, K. K. Schaffer, L. Shaw, E. Shirokoff, R. Simcoe, J. Song, H. G. Spieler, B. Stalder, Z. Staniszewski, A. A. Stark, K. Story, C. W. Stubbs, R. Šuhada, A. Van Engelen, K. Vanderlinde, J. D. Vieira, A. Vikhlinin, R. Williamson, O. Zahn, and A. Zenteno. A massive, cooling-flow-induced starburst in the core of a luminous cluster of galaxies. *Nature*, 488(7411):349–352, aug 2012. URL: http://dx.doi.org/10.1038/nature11379http://10.0.4.14/nature11379https://www.nature.com/articles/nature11379{#}supplementary-information, arXiv:1208.2962, doi:10.1038/nature11379.

[13] R. J. Foley, K. Andersson, G. Bazin, T. De Haan, J. Ruel, P. A.R. Ade, K. A. Aird, R. Armstrong, M. L.N. Ashby, M. Bautz, B. A. Benson, L. E. Bleem, M. Bonamente, M. Brodwin, J. E. Carlstrom, C. L. Chang, A. Clocchiatti, T. M. Crawford, A. T. Crites, S. Desai, M. A. Dobbs, J. P. Dudley, G. G. Fazio, W. R. Forman, G. Garmire, E. M. George, M. D. Gladders, A. H. Gonzalez, N. W. Halverson, F. W. High, G. P. Holder, W. L. Holzapfel, S. Hoover, J. D. Hrubes, C. Jones, M. Joy, R. Keisler, L. Knox, A. T. Lee, E. M. Leitch, M. Lueker, D. Luong-Van, D. P. Marrone, J. J. McMahon, J. Mehl, S. S. Meyer, J. J. Mohr, T. E. Montroy, S. S. Murray, S. Padin, T. Plagge, C. Pryke, C. L. Reichardt, A. Rest, J. E. Ruhl, B. R. Saliwanchik, A. Saro, K. K. Schaffer, L. Shaw, E. Shirokoff, J. Song, H. G. Spieler, B. Stalder, S. A. Stanford, Z. Staniszewski, A. A. Stark, K. Story, C. W. Stubbs, K. Vanderlinde, J. D. Vieira, A. Vikhlinin, R. Williamson, and A. Zenteno. Discovery and cosmological implications of SPT-CL J2106-5844, the most massive known cluster at z>1. *Astrophysical Journal*, 731(2):86, apr 2011. URL: http://stacks.iop.org/0004-637X/731/i=2/a=86?key=crossref.ed3161bd9c249b22c6b2433638263d05, arXiv:1101.1286, doi:10.1088/0004-637X/731/2/86.

[14] M Henkel, H Hinrichsen, and S Lübeck. *Non-quilibrium phase transitions Volume 1: Absorbing phase transitions*. Springer, 2008.

[15] David Chandler. *Introduction to modern statistical mechanics*. Oxford University Press, 1987.

[16] Giovanni Gallavotti. *Nonequilibrium and irreversibility*. Theoretical and mathematical physics. Springer, Cham ; Heidelberg [u.a.], 2014.

[17] Björn Hof, Casimir W. H. van Doorne, Jerry Westerweel, Frans T. M. Nieuwstadt, Holger Faisst, Bruno Eckhardt, Hakan Wedin, Richard R. Kerswell, and

Fabian Waleffe. Experimental observation of nonlinear traveling waves in turbulent pipe flow. *Science*, 305(5690):1594–1598, 2004. URL: http://science.sciencemag.org/content/305/5690/1594, arXiv:http://science.sciencemag.org/content/305/5690/1594.full.pdf, doi:10.1126/science.1100393.

[18] Dean Culver and Yaroslav Urzhumov. Forced underwater laminar flows with active magnetohydrodynamic metamaterials. *Phys. Rev. E*, 96:063107, Dec 2017. URL: https://link.aps.org/doi/10.1103/PhysRevE.96.063107, doi:10.1103/PhysRevE.96.063107.

[19] Malte Henkel. *Ageing and the glass transition*. Springer, Berlin, Heidelberg, 2007.

[20] M Henkel and M Pleimling. *Non-quilibrium phase transitions Volume 2: Ageing and dynamical scaling far from equilibrium*. Springer, 2010.

[21] L C E Struik. *Physical Aging In Amorphous Polymers and Other Materials*, volume 106. Elsevier, Amsterdam, 01 1978.

[22] Tilman Enss, Malte Henkel, Alan Picone, and Ulrich Schollwöck. Ageing phenomena without detailed balance: The contact process. *Journal of Physics A: Mathematical and General*, 37(44):10479–10495, nov 2004. URL: http://stacks.iop.org/0305-4470/37/i=44/a=002?key=crossref.621c2a854642c62317266cfdcf7f0d8b, arXiv:0406147v1, doi:10.1088/0305-4470/37/44/002.

[23] Tim Langen. *Non-equilibrium Dynamics of One-Dimensional Bose Gases*. Springer, Cham, Switzerland, 2015.

[24] Anatoli Polkovnikov, Krishnendu Sengupta, Alessandro Silva, and Mukund Vengalattore. Colloquium: Nonequilibrium dynamics of closed interacting quantum systems. *Rev. Mod. Phys.*, 83:863–883, Aug 2011. URL: https://link.aps.org/doi/10.1103/RevModPhys.83.863, doi:10.1103/RevModPhys.83.863.

[25] Tim Langen, Remi Geiger, and JÃ¶rg Schmiedmayer. Ultracold atoms out of equilibrium. *Annual Review of Condensed Matter Physics*, 6(1):201–217, 2015. URL: https://doi.org/10.1146/annurev-conmatphys-031214-014548, arXiv:https://doi.org/10.1146/annurev-conmatphys-031214-014548, doi:10.1146/annurev-conmatphys-031214-014548.

[26] M. Gring, M. Kuhnert, T. Langen, T. Kitagawa, B. Rauer, M. Schreitl, I. Mazets, D. Adu Smith, E. Demler, and J. Schmiedmayer. Relaxation and prethermalization in an isolated quantum system. *Science*, 337(6100):1318–1322, 2012. URL: http://science.sciencemag.org/content/337/6100/1318, arXiv:http://science.sciencemag.org/content/337/6100/1318.full.pdf, doi:10.1126/science.1224953.

[27] J. Berges, Sz. Borsányi, and C. Wetterich. Prethermalization. *Phys. Rev. Lett.*, 93:142002, Sep 2004. URL: https://link.aps.org/doi/10.1103/PhysRevLett.93.142002, doi:10.1103/PhysRevLett.93.142002.

[28] Boris Nowak, Jan Schole, and Thomas Gasenzer. Universal dynamics on the way to thermalization. *New Journal of Physics*, 16(9):093052,

sep 2014. URL: http://stacks.iop.org/1367-2630/16/i=9/a=093052?key=crossref.61e2b279ef48a5ca0a37d599937235d7, arXiv:1206.3181, doi:10.1088/1367-2630/16/9/093052.

[29] M. Heyl, A. Polkovnikov, and S. Kehrein. Dynamical quantum phase transitions in the transverse-field ising model. *Phys. Rev. Lett.*, 110:135704, Mar 2013. URL: https://link.aps.org/doi/10.1103/PhysRevLett.110.135704, doi:10.1103/PhysRevLett.110.135704.

[30] Bojan Žunkovič, Markus Heyl, Michael Knap, and Alessandro Silva. Dynamical quantum phase transitions in spin chains with long-range interactions: Merging different concepts of nonequilibrium criticality. *Phys. Rev. Lett.*, 120:130601, Mar 2018. URL: https://link.aps.org/doi/10.1103/PhysRevLett.120.130601, doi:10.1103/PhysRevLett.120.130601.

[31] P. Jurcevic, H. Shen, P. Hauke, C. Maier, T. Brydges, C. Hempel, B. P. Lanyon, M. Heyl, R. Blatt, and C. F. Roos. Direct Observation of Dynamical Quantum Phase Transitions in an Interacting Many-Body System. *Physical Review Letters*, 119(8):080501, aug 2017. URL: https://link.aps.org/doi/10.1103/PhysRevLett.119.080501, doi:10.1103/PhysRevLett.119.080501.

[32] J. Zhang, G. Pagano, P. W. Hess, A. Kyprianidis, P. Becker, H. Kaplan, A. V. Gorshkov, Z. X. Gong, and C. Monroe. Observation of a many-body dynamical phase transition with a 53-qubit quantum simulator. *Nature*, 551(7682):601–604, aug 2017. URL: http://arxiv.org/abs/1708.01044http://dx.doi.org/10.1038/nature24654, arXiv:1708.01044, doi:10.1038/nature24654.

[33] P. W. Anderson. Absence of diffusion in certain random lattices. *Phys. Rev.*, 109:1492–1505, Mar 1958. URL: https://link.aps.org/doi/10.1103/PhysRev.109.1492, doi:10.1103/PhysRev.109.1492.

[34] Diederik S Wiersma, Paolo Bartolini, Ad Lagendijk, and Roberto Righini. Localization of light in a disordered medium. *Nature*, 390:671, dec 1997. URL: http://dx.doi.org/10.1038/37757http://10.0.4.14/37757.

[35] Tal Schwartz, Guy Bartal, Shmuel Fishman, and Mordechai Segev. Transport and Anderson localization in disordered two-dimensional photonic lattices. *Nature*, 446:52, mar 2007. URL: http://dx.doi.org/10.1038/nature05623http://10.0.4.14/nature05623https://www.nature.com/articles/nature05623{#}supplementary-information.

[36] Juliette Billy, Vincent Josse, Zhanchun Zuo, Alain Bernard, Ben Hambrecht, Pierre Lugan, David Clément, Laurent Sanchez-Palencia, Philippe Bouyer, and Alain Aspect. Direct observation of Anderson localization of matter waves in a controlled disorder. *Nature*, 453:891, jun 2008. URL: http://dx.doi.org/10.1038/nature07000http://10.0.4.14/nature07000.

[37] Giacomo Roati, Chiara D'Errico, Leonardo Fallani, Marco Fattori, Chiara Fort, Matteo Zaccanti, Giovanni Modugno, Michele Modugno, and Massimo Inguscio. Anderson localization of a non-interacting Bose-Einstein condensate. *Na-*

ture, 453:895, jun 2008. URL: http://dx.doi.org/10.1038/nature07071http://10.0.4.14/nature07071.

[38] J Eisert, M Friesdorf, and C Gogolin. Quantum many-body systems out of equilibrium. *Nature Physics*, 11(February):124, 2015. URL: http://arxiv.org/abs/1408.5148, arXiv:1408.5148, doi:10.1038/NPHYS3215.

[39] Michael Schreiber, Sean S. Hodgman, Pranjal Bordia, Henrik P. Lüschen, Mark H. Fischer, Ronen Vosk, Ehud Altman, Ulrich Schneider, and Immanuel Bloch. Observation of many-body localization of interacting fermions in a quasirandom optical lattice. *Science*, 349(6250):842–845, 2015. URL: http://science.sciencemag.org/content/349/6250/842, arXiv:http://science.sciencemag.org/content/349/6250/842.full.pdf, doi:10.1126/science.aaa7432.

[40] J Smith, A Lee, P Richerme, B Neyenhuis, P W Hess, P Hauke, M Heyl, D A Huse, and C Monroe. Many-body localization in a quantum simulator with programmable random disorder. *Nature Physics*, 12:907, jun 2016. URL: http://dx.doi.org/10.1038/nphys3783http://10.0.4.14/nphys3783https://www.nature.com/articles/nphys3783{#}supplementary-information.

[41] N. Y. Yao, C. R. Laumann, S. Gopalakrishnan, M. Knap, M. Müller, E. A. Demler, and M. D. Lukin. Many-Body Localization in Dipolar Systems. *Phys. Rev. Lett.*, 113(24):243002, 2014. URL: http://link.aps.org/doi/10.1103/PhysRevLett.113.243002, doi:10.1103/PhysRevLett.113.

[42] S. Choi, J. Choi, R. Landig, G. Kucsko, H. Zhou, J. Isoya, F. Jelezko, H. Sumiya S. Onoda, V. Khemani, C. von Keyserlingk, N. Y. Yao, E. Demler, and M. D. Lukin. Observation of discrete time-crystalline order in a disordered dipolar many-body system. *Nature*, 543:221–225, 2017. doi:10.1038/nature21426.

[43] J Zhang, P W Hess, A Kyprianidis, P Becker, A Lee, J Smith, G Pagano, I.-D. Potirniche, A C Potter, A Vishwanath, N Y Yao, and C Monroe. Observation of a discrete time crystal. *Nature*, 543:217, mar 2017. URL: http://dx.doi.org/10.1038/nature21413http://10.0.4.14/nature21413.

[44] T H Maiman. Simulated optical radiation in ruby. *Nature*, 187:493–494, aug 1960. URL: http://dx.doi.org/10.1038/187493a0http://10.0.4.14/187493a0.

[45] Michael Scheibner, Thomas Schmidt, Lukas Worschech, Alfred Forchel, Gerd Bacher, Thorsten Passow, and Detlef Hommel. Superradiance of quantum dots. *Nature Physics*, 3:106, jan 2007. URL: http://dx.doi.org/10.1038/nphys494http://10.0.4.14/nphys494https://www.nature.com/articles/nphys494{#}supplementary-information.

[46] R. H. Dicke. Coherence in spontaneous radiation processes. *Phys. Rev.*, 93:99–110, Jan 1954. URL: https://link.aps.org/doi/10.1103/PhysRev.93.99, doi:10.1103/PhysRev.93.99.

[47] Justin G Bohnet, Zilong Chen, Joshua M Weiner, Dominic Meiser, Murray J Holland, and James K Thompson. A steady-state superradiant laser with

less than one intracavity photon. *Nature*, 484:78, apr 2012. URL: http://dx.doi.org/10.1038/nature10920http://10.0.4.14/nature10920https://www.nature.com/articles/nature10920{#}supplementary-information.

[48] Ricardo Gutiérrez, Cristiano Simonelli, Matteo Archimi, Francesco Castellucci, Ennio Arimondo, Donatella Ciampini, Matteo Marcuzzi, Igor Lesanovsky, and Oliver Morsch. Experimental signatures of an absorbing-state phase transition in an open driven many-body quantum system. *Phys. Rev. A*, 96(4):41602, oct 2017. URL: https://link.aps.org/doi/10.1103/PhysRevA.96.041602, doi:10.1103/PhysRevA.96.041602.

[49] M Marcuzzi, E Levi, W Li, J P Garrahan, B Olmos, and I Lesanovsky. Non-equilibrium universality in the dynamics of dissipative cold atomic gases. *New Journal of Physics*, 17(7):072003, jul 2015. URL: http://stacks.iop.org/1367-2630/17/i=7/a=072003?key=crossref.2276c0299ea5d3e67f6971bd3ec26dfc, arXiv:1411.7984, doi:10.1088/1367-2630/17/7/072003.

[50] Michael Buchhold, Benjamin Everest, Matteo Marcuzzi, Igor Lesanovsky, and Sebastian Diehl. Nonequilibrium effective field theory for absorbing state phase transitions in driven open quantum spin systems. *Phys. Rev. B*, 95:014308, Jan 2017. URL: https://link.aps.org/doi/10.1103/PhysRevB.95.014308, doi:10.1103/PhysRevB.95.014308.

[51] Matteo Marcuzzi, Michael Buchhold, Sebastian Diehl, and Igor Lesanovsky. Absorbing state phase transition with competing quantum and classical fluctuations. *Phys. Rev. Lett.*, 116:245701, Jun 2016. URL: http://link.aps.org/doi/10.1103/PhysRevLett.116.245701, doi:10.1103/PhysRevLett.116.245701.

[52] Yu-Ping Lin, Ying-Jer Kao, Pochung Chen, and Yu-Cheng Lin. Griffiths singularities in the random quantum ising antiferromagnet: A tree tensor network renormalization group study. *Phys. Rev. B*, 96:064427, Aug 2017. URL: https://link.aps.org/doi/10.1103/PhysRevB.96.064427, doi:10.1103/PhysRevB.96.064427.

[53] J. Fröhlich and T. Spencer. Some recent rigorous results in the theory of phase transitions and critical phenomena. *Les rencontres physiciens-mathématiciens de Strasbourg -RCP25*, pages 42–83, 1982. URL: http://www.numdam.org/item?id=RCP25_1982__30__42_0.

[54] T. D. Lee and C. N. Yang. Statistical theory of equations of state and phase transitions. ii. lattice gas and Ising model. *Phys. Rev.*, 87:410–419, Aug 1952. URL: http://link.aps.org/doi/10.1103/PhysRev.87.410, doi:10.1103/PhysRev.87.410.

[55] Haye Hinrichsen. Non-equilibrium critical phenomena and phase transitions into absorbing states. *Advances in Physics*, 49(7):815–958, 2000. URL: https://doi.org/10.1080/00018730050198152, arXiv:https://doi.org/10.1080/00018730050198152, doi:10.1080/00018730050198152.

[56] Kazumasa A Takeuchi, Masafumi Kuroda, Hugues Chaté, and Masaki Sano. Directed Percolation Criticality in Turbulent Liquid Crystals. *Phys. Rev. Lett.*, 99(23):234503, dec 2007. URL: https://link.aps.org/doi/10.1103/PhysRevLett.99.234503, doi:10.1103/PhysRevLett.99.234503.

[57] Grégoire Lemoult, Liang Shi, Kerstin Avila, Shreyas V. Jalikop, Marc Avila, and Björn Hof. Directed percolation phase transition to sustained turbulence in Couette flow. *Nature Physics*, 12(3):254–258, feb 2016. URL: http://dx.doi.org/10.1038/nphys3675http://10.0.4.14/nphys3675https://www.nature.com/articles/nphys3675{#}supplementary-information, arXiv:1510.07868, doi:10.1038/nphys3675.

[58] Masaki Sano and Keiichi Tamai. A universal transition to turbulence in channel flow turbulence. *Nature Physics*, 12:249–253, feb 2016. URL: http://dx.doi.org/10.1038/nphys3659http://10.0.4.14/nphys3659https://www.nature.com/articles/nphys3659{#}supplementary-information.

[59] Kim Christensen and Nicholas R. Moloney. *Complexity and criticality*. Number ARRAY(0x3301f28) in Imperial College Press advanced physics texts. Imperial College Press, London, 2005.

[60] Per Bak, Chao Tang, and Kurt Wiesenfeld. Self-organized criticality: An explanation of the 1/f noise. *Phys. Rev. Lett.*, 59:381–384, Jul 1987. URL: https://link.aps.org/doi/10.1103/PhysRevLett.59.381, doi:10.1103/PhysRevLett.59.381.

[61] Per Bak, Chao Tang, and Kurt Wiesenfeld. Self-organized criticality. *Phys. Rev. A*, 38:364–374, Jul 1988. URL: https://link.aps.org/doi/10.1103/PhysRevA.38.364, doi:10.1103/PhysRevA.38.364.

[62] Janina Hesse and Thilo Gross. Self-organized criticality as a fundamental property of neural systems. *Frontiers in Systems Neuroscience*, 8:166, 2014. doi:10.3389/fnsys.2014.00166.

[63] A. Sornette and D. Sornette. Self-organized criticality and earthquakes. *EPL (Europhysics Letters)*, 9(3):197, 1989. URL: http://stacks.iop.org/0295-5075/9/i=3/a=002.

[64] C J Rhodes and R M Anderson. Power laws governing epidemics in isolated populations. *Nature*, 381(7):600–602, 1996. doi:doi:10.1038/381600a0.

[65] Bruce D. Malamud, Gleb Morein, and Donald L. Turcotte. Forest fires: An example of self-organized critical behavior. *Science*, 281(5384):1840–1842, 1998. URL: http://science.sciencemag.org/content/281/5384/1840, arXiv:http://science.sciencemag.org/content/281/5384/1840.full.pdf, doi:10.1126/science.281.5384.1840.

[66] James P. Gleeson, Jonathan A. Ward, Kevin P. O'Sullivan, and William T. Lee. Competition-induced criticality in a model of meme popularity. *Phys. Rev. Lett.*, 112:048701, Jan 2014. URL: https://link.aps.org/doi/10.1103/PhysRevLett.112.048701, doi:10.1103/PhysRevLett.112.048701.

[67] Vidar Frette, Kim Christensen, Anders Malthe-Sørenssen, Jens Feder, Torstein Jøssang, and Paul Meakin. Avalanche dynamics in a pile of rice. *Nature*, 379:49, jan 1996. URL: http://dx.doi.org/10.1038/379049a0http://10.0.4.14/379049a0.

[68] E. Altshuler and T. H. Johansen. Colloquium: Experiments in vortex avalanches. *Reviews of Modern Physics*, 76(2):471–487, apr 2004. URL: https://link.aps.org/doi/10.1103/RevModPhys.76.471, arXiv:0402097, doi:10.1103/RevModPhys.76.471.

[69] D. E. Juanico and C. Monterola. Background activity drives criticality of neuronal avalanches. *Journal of Physics A: Mathematical and Theoretical*, 40(31):9297–9309, aug 2007. URL: http://stacks.iop.org/1751-8121/40/i=31/a=008?key=crossref.6a45ebcec497f205c126e9d279e267a1, doi:10.1088/1751-8113/40/31/008.

[70] Woodrow L Shew, Wesley P Clawson, Jeff Pobst, Yahya Karimipanah, Nathaniel C Wright, and Ralf Wessel. Adaptation to sensory input tunes visual cortex toÂ criticality. *Nature Physics*, 11:659, jun 2015. URL: http://dx.doi.org/10.1038/nphys3370http://10.0.4.14/nphys3370https://www.nature.com/articles/nphys3370{#}supplementary-information.

[71] Juan A Bonachela and Miguel A Muñoz. Self-organization without conservation: True or just apparent scale-invariance? *Journal of Statistical Mechanics: Theory and Experiment*, 2009(9):P09009, sep 2009. URL: http://stacks.iop.org/1742-5468/2009/i=09/a=P09009?key=crossref.9f365ed97a1fc93fc1506ff6b21dc753, arXiv:0905.1799, doi:10.1088/1742-5468/2009/09/P09009.

[72] Juan A Bonachela, Sebastiano de Franciscis, Joaquín J Torres, and Miguel A Muñoz. Self-organization without conservation: are neuronal avalanches generically critical? *Journal of Statistical Mechanics: Theory and Experiment*, 2010(02):P02015, feb 2010. URL: http://stacks.iop.org/1742-5468/2010/i=02/a=P02015?key=crossref.3e658ce5a625767868e6ee02cfff95bd, doi:10.1088/1742-5468/2010/02/P02015.

[73] Dranreb Earl Juanico, Christopher Monterola, and Caesar Saloma. Dissipative self-organized branching in a dynamic population. *Phys. Rev. E*, 75:045105, Apr 2007. URL: https://link.aps.org/doi/10.1103/PhysRevE.75.045105, doi:10.1103/PhysRevE.75.045105.

[74] M Müller, S Diehl, G Pupillo, and P Zoller. Engineered open systems and quantum simulations with atoms and ions. In Paul Berman, Ennio Arimondo, and Chun Lin, editors, *Advances in Atomic, Molecular, and Optical Physics*, volume 61 of *Advances In Atomic, Molecular, and Optical Physics*, pages 1 – 80. Academic Press, 2012. URL: http://www.sciencedirect.com/science/article/pii/B9780123964823000016, doi:https://doi.org/10.1016/B978-0-12-396482-3.00001-6.

[75] Immanuel Bloch, Jean Dalibard, and Wilhelm Zwerger. Many-body physics with ultracold gases. *Rev. Mod. Phys.*, 80:885–964, Jul 2008. URL: https://link.aps.org/doi/10.1103/RevModPhys.80.885, doi:10.1103/RevModPhys.80.885.

[76] Maciej Lewenstein, Anna Sanpera, Veronica Ahufinger, Bogdan Damski, Aditi Sen(De), and Ujjwal Sen. Ultracold atomic gases in optical lattices: mimicking condensed matter physics and beyond. *Advances in Physics*, 56(2):243–379,

mar 2007. URL: https://doi.org/10.1080/00018730701223200, doi:10.1080/00018730701223200.

[77] J. T. Barreiro, M. Müller, P. Schindler, D. Nigg, T. Monz, M. Chwalla, M. Hennrich, C. F. Roos, P. Zoller, and R. Blatt. An open-system quantum simulator with trapped ions. *Nature*, 470(7335):486–491, 2011. doi:10.1038/nature09801.

[78] P Schindler, M Müller, D Nigg, J T Barreiro, E A Martinez, M Hennrich, T Monz, S Diehl, P Zoller, and R Blatt. Quantum simulation of dynamical maps with trapped ions. *Nature Physics*, 9(6):361–367, 2013.

[79] J. G. Bohnet, B. C. Sawyer, J. W. Britton, M. L. Wall, A. M. Rey, M. Foss-feig, and J. J. Bollinger. Quantum spin dynamics and entanglement generation with hundreds of trapped ions. *Science*, 352(6291):1297–1302, 2016. doi:10.1126/science.aad9958.

[80] Joseph W. Britton, Brian C. Sawyer, Adam C. Keith, C.-C. Joseph Wang, James K. Freericks, Hermann Uys, Michael J. Biercuk, and John J. Bollinger. Engineered two-dimensional Ising interactions in a trapped-ion quantum simulator with hundreds of spins. *Nature*, 484(7395):489–492, apr 2012. URL: http://www.nature.com/doifinder/10.1038/nature10981, doi:10.1038/nature10981.

[81] A. A. Houck, H. E. Türeci, and J. Koch. On-chip quantum simulation with superconducting circuits. *Nature Physics*, 8:292–299, 2012. doi:10.1038/nphys2251.

[82] C. Eichler, J. Mlynek, J. Butscher, P. Kurpiers, K. Hammerer, T. J. Osborne, and A. Wallraff. Exploring interacting quantum many-body systems by experimentally creating continuous matrix product states in superconducting circuits. *Phys. Rev. X*, 5:041044, Dec 2015. URL: http://link.aps.org/doi/10.1103/PhysRevX.5.041044, doi:10.1103/PhysRevX.5.041044.

[83] Jens Koch, Andrew A. Houck, Karyn Le Hur, and S. M. Girvin. Time-reversal-symmetry breaking in circuit-qed-based photon lattices. *Phys. Rev. A*, 82:043811, Oct 2010. URL: https://link.aps.org/doi/10.1103/PhysRevA.82.043811, doi:10.1103/PhysRevA.82.043811.

[84] J. Kasprzak, M. Richard, S. Kundermann, A. Baas, P. Jeambrun, J. M. J. Keeling, F. M. Marchetti, M. H. Szymańska, R. Andre, J. L. Staehli, V. Savona, P. B. Littlewood, B. Deveaud, and L. S. Dang. Bose–Einstein condensation of exciton polaritons. *Nature*, 443(7110):409–414, 2006. doi:10.1038/nature05131.

[85] Iacopo Carusotto and Cristiano Ciuti. Quantum fluids of light. *Rev. Mod. Phys.*, 85:299–366, Feb 2013. URL: https://link.aps.org/doi/10.1103/RevModPhys.85.299, doi:10.1103/RevModPhys.85.299.

[86] L. M. Sieberer, S. D. Huber, E. Altman, and S. Diehl. Dynamical critical phenomena in driven-dissipative systems. *Phys. Rev. Lett.*, 110:195301, May 2013. URL: https://link.aps.org/doi/10.1103/PhysRevLett.110.195301, doi:10.1103/PhysRevLett.110.195301.

[87] Tim Byrnes, Na Young Kim, and Yoshihisa Yamamoto. Exciton-polariton condensates. *Nature Physics*, 10:803–815, 2014. URL: http://www.nature.com/nphys/journal/v10/n11/full/nphys3143.html, arXiv:arXiv:1411.6822v1.

[88] Jan Klaers, Julian Schmitt, Frank Vewinger, and Martin Weitz. Bose-Einstein condensation of photons in an optical microcavity. *Nature*, 468(7323):545–548, nov 2010. URL: http://dx.doi.org/10.1038/nature09567http://10.0.4.14/nature09567, arXiv:1007.4088, doi:10.1038/nature09567.

[89] David Dung, Christian Kurtscheid, Tobias Damm, Julian Schmitt, Frank Vewinger, Martin Weitz, and Jan Klaers. Variable potentials for thermalized light and coupled condensates. *Nature Photonics*, 11:565, aug 2017. URL: http://dx.doi.org/10.1038/nphoton.2017.139http://10.0.4.14/nphoton.2017.139https://www.nature.com/articles/nphoton.2017.139{#}supplementary-information.

[90] Y. Colombe, T. Steinmetz, G. Dubois, F. Linke, D. Hunger, and J. Reichel. Strong atom–field coupling for Bose–Einstein condensates in an optical cavity on a chip. *Nature*, 450(7167):272–276, 2007. doi:10.1038/nature06331.

[91] Kristian Baumann, Christine Guerlin, Ferdinand Brennecke, and Tilman Esslinger. Dicke quantum phase transition with a superfluid gas in an optical cavity. *Nature*, 464(7293):1301–1306, 2010. URL: http://dx.doi.org/10.1038/nature09009, arXiv:0912.3261, doi:10.1038/nature09009.

[92] Helmut Ritsch, Peter Domokos, Ferdinand Brennecke, and Tilman Esslinger. Cold atoms in cavity-generated dynamical optical potentials. *Rev. Mod. Phys.*, 85:553–601, Apr 2013. URL: https://link.aps.org/doi/10.1103/RevModPhys.85.553, doi:10.1103/RevModPhys.85.553.

[93] M. M. Valado, C. Simonelli, M. D. Hoogerland, I. Lesanovsky, J. P. Garrahan, E. Arimondo, D. Ciampini, and O. Morsch. Experimental observation of controllable kinetic constraints in a cold atomic gas. *Phys. Rev. A*, 93:040701, Apr 2016. doi:10.1103/PhysRevA.93.040701.

[94] M. Marcuzzi, J. Schick, .B Olmos, and I. Lesanovsky. Effective dynamics of strongly dissipative Rydberg gases. *Journal of Physics A: Mathematical and Theoretical*, 47(48):482001, 2014. URL: http://stacks.iop.org/1751-8121/47/i=48/a=482001.

[95] Christian Gross and Immanuel Bloch. Quantum simulations with ultracold atoms in optical lattices. *Science*, 357(6355):995–1001, 2017. URL: http://science.sciencemag.org/content/357/6355/995, arXiv:http://science.sciencemag.org/content/357/6355/995.full.pdf, doi:10.1126/science.aal3837.

[96] Robert Löw, Hendrik Weimer, Johannes Nipper, Jonathan B Balewski, Björn Butscher, Hans Peter BÃ$\frac{1}{4}$chler, and Tilman Pfau. An experimental and theoretical guide to strongly interacting rydberg gases. *Journal of Physics B: Atomic, Molecular and Optical Physics*, 45(11):113001, 2012. URL: http://stacks.iop.org/0953-4075/45/i=11/a=113001.

[97] Antoine Browaeys, Daniel Barredo, and Thierry Lahaye. Experimental investigations of dipole-dipole interactions between a few Rydberg atoms. *Journal of Physics B: Atomic, Molecular and Optical Physics*, 49(15):152001,

aug 2016. URL: http://stacks.iop.org/0953-4075/49/i=15/a=152001?key=crossref.e79f8f4b6c4aa989cefc0bd9e9e130a2, doi:10.1088/0953-4075/49/15/152001.

[98] E. A. Goldschmidt, T. Boulier, R. C. Brown, S. B. Koller, J. T. Young, A. V. Gorshkov, S. L. Rolston, and J. V. Porto. Anomalous broadening in driven dissipative Rydberg systems. *Phys. Rev. Lett.*, 116:113001, 2016. doi:10.1103/PhysRevLett.116.113001.

[99] I Mourachko, D Comparat, F de Tomasi, A Fioretti, P Nosbaum, V M Akulin, and P Pillet. Many-Body Effects in a Frozen Rydberg Gas. *Phys. Rev. Lett.*, 80(2):253–256, January 1998. URL: http://link.aps.org/doi/10.1103/PhysRevLett.80.253, doi:10.1103/PhysRevLett.80.253.

[100] W R Anderson, J R Veale, and T F Gallagher. Resonant Dipole-Dipole Energy Transfer in a Nearly Frozen Rydberg Gas. *Phys. Rev. Lett.*, 80(2):249–252, January 1998. URL: http://link.aps.org/doi/10.1103/PhysRevLett.80.249, doi:10.1103/PhysRevLett.80.249.

[101] K Singer, M Reetz-Lamour, T Amthor, L G Marcassa, and M Weidemüller. Spectral Broadening and Suppression of Excitation Induced by Ultralong-Range Interactions in a Cold Gas of Rydberg Atoms. *Phys. Rev. Lett.*, 93:163001, 2004. URL: http://link.aps.org/abstract/PRL/v93/e163001.

[102] D. Tong, S. M. Farooqi, J. Stanojevic, S. Krishnan, Y. P. Zhang, R. Côté, E. E. Eyler, and P. L. Gould. Local blockade of rydberg excitation in an ultracold gas. *Phys. Rev. Lett.*, 93:063001, Aug 2004. URL: https://link.aps.org/doi/10.1103/PhysRevLett.93.063001, doi:10.1103/PhysRevLett.93.063001.

[103] Daniel Comparat and Pierre Pillet. Dipole blockade in a cold Rydberg atomic sample. *JOSA B*, 27(6):A208—-A232, 2010.

[104] F Cinti, T Macrì, W Lechner, G Pupillo, and T Pohl. Defect-induced supersolidity with soft-core bosons. *Nature Communications*, 5:3235, feb 2014. URL: http://dx.doi.org/10.1038/ncomms4235http://10.0.4.14/ncomms4235.

[105] G. Pupillo, a. Micheli, M. Boninsegni, I. Lesanovsky, and P. Zoller. Strongly correlated gases of rydberg-dressed atoms: Quantum and classical dynamics. *Physical Review Letters*, 104(22):3–6, 2010. arXiv:1001.0519, doi:10.1103/PhysRevLett.104.223002.

[106] N. Henkel, F. Cinti, P. Jain, G. Pupillo, and T. Pohl. Supersolid vortex crystals in rydberg-dressed bose-einstein condensates. *Phys. Rev. Lett.*, 108:265301, Jun 2012. URL: http://link.aps.org/doi/10.1103/PhysRevLett.108.265301, doi:10.1103/PhysRevLett.108.265301.

[107] Liang He and Walter Hofstetter. Supersolid phase of cold fermionic polar molecules in two-dimensional optical lattices. *Phys. Rev. A*, 83:053629, May 2011. URL: https://link.aps.org/doi/10.1103/PhysRevA.83.053629, doi:10.1103/PhysRevA.83.053629.

[108] Chi-Ming Chang, Wei-Chao Shen, Chen-Yen Lai, Pochung Chen, and Daw-Wei Wang. Interaction-induced first-order correlation between spatially separated one-dimensional dipolar fermions. *Phys. Rev. A*, 79:053630, May 2009. URL: https://link.aps.org/doi/10.1103/PhysRevA.79.053630, doi:10.1103/PhysRevA.79.053630.

[109] M. Dalmonte, P. Zoller, and G. Pupillo. Trimer liquids and crystals of polar molecules in coupled wires. *Phys. Rev. Lett.*, 107:163202, Oct 2011. URL: https://link.aps.org/doi/10.1103/PhysRevLett.107.163202, doi:10.1103/PhysRevLett.107.163202.

[110] Vera Bendkowsky, Björn Butscher, Johannes Nipper, James P Shaffer, Robert Löw, and Tilman Pfau. Observation of ultralong-range Rydberg molecules. *Nature*, 458:1005, apr 2009. URL: http://dx.doi.org/10.1038/nature07945http://10.0.4.14/nature07945.

[111] J. D. Pritchard, K. J. Weatherill, and C. S. Adams. Non-linear optics using cold Rydberg atoms. In *Annual Review of Cold Atoms and Molecules*, volume Volume 1 of *Annual Review of Cold Atoms and Molecules*, pages 301–350. WORLD SCIENTIFIC, oct 2012. URL: http://arxiv.org/abs/1205.4890{%}0Ahttp://dx.doi.org/10.1142/9789814440400{_}0008, arXiv:1205.4890, doi:10.1142/9789814440400_0008.

[112] M. Saffman, T. G. Walker, and K. Mølmer. Quantum information with rydberg atoms. *Rev. Mod. Phys.*, 82:2313–2363, Aug 2010. URL: https://link.aps.org/doi/10.1103/RevModPhys.82.2313, doi:10.1103/RevModPhys.82.2313.

[113] Hendrik Weimer, Markus Müller, Igor Lesanovsky, Peter Zoller, and Hans Peter Büchler. A Rydberg quantum simulator. *Nature Physics*, 6(5):382–388, 2010.

[114] Thomas C. Killian and Steven L. Rolston. Ultracold neutral plasmas. *Physics Today*, 63(3):46–51, jan 2010. URL: http://stacks.iop.org/0034-4885/80/i=1/a=017001?key=crossref.2e1a8ba7578c9add94f8dd94c9e1392d, arXiv:0612097, doi:10.1063/1.3366240.

[115] M. Robert-de Saint-Vincent, C. S. Hofmann, H. Schempp, G. Günter, S. Whitlock, and M. Weidemüller. Spontaneous avalanche ionization of a strongly blockaded rydberg gas. *Phys. Rev. Lett.*, 110:045004, Jan 2013. URL: https://link.aps.org/doi/10.1103/PhysRevLett.110.045004, doi:10.1103/PhysRevLett.110.045004.

[116] T M Weber, M Höning, T Niederprüm, T Manthey, O Thomas, V Guarrera, M Fleischhauer, G Barontini, and H Ott. Mesoscopic Rydberg-blockaded ensembles in the superatom regime and beyond. *Nature Physics*, 11:157, 2015.

[117] N. Malossi, M. M. Valado, S. Scotto, P. Huillery, P. Pillet, D. Ciampini, E. Arimondo, and O. Morsch. Full counting statistics and phase diagram of a dissipative Rydberg gas. *Phys. Rev. Lett.*, 113:023006, Jul 2014. URL: http://link.aps.org/doi/10.1103/PhysRevLett.113.023006, doi:10.1103/PhysRevLett.113.023006.

[118] C. Simonelli, M. M. Valado, G. Masella, L. Asteria, E. Arimondo, D. Ciampini, and O. Morsch. Seeded excitation avalanches in off-resonantly driven Rydberg gases. *J.*

Phys. B: At. Mol. Opt. Phys., 49:154002, 2016. doi:10.1088/0953-4075/49/15/154002.

[119] B. J. DeSalvo, J. A. Aman, C. Gaul, T. Pohl, S. Yoshida, J. Burgdörfer, K. R. A. Hazzard, F. B. Dunning, and T. C. Killian. Rydberg-blockade effects in Autler-Townes spectra of ultracold strontium. *Phys. Rev. A*, 93:022709, Feb 2016. URL: https://link.aps.org/doi/10.1103/PhysRevA.93.022709, doi:10.1103/PhysRevA.93.022709.

[120] J. A. Aman, B. J. DeSalvo, F. B. Dunning, T. C. Killian, S. Yoshida, and J. Burgdörfer. Trap losses induced by near-resonant Rydberg dressing of cold atomic gases. *Phys. Rev. A*, 93:043425, Apr 2016. URL: http://link.aps.org/doi/10.1103/PhysRevA.93.043425, doi:10.1103/PhysRevA.93.043425.

[121] H. Schempp, G. Günter, M. Robert-de Saint-Vincent, C. S. Hofmann, D. Breyel, A. Komnik, D. W. Schönleber, M. Gärttner, J. Evers, S. Whitlock, and M. Weidemüller. Full counting statistics of laser excited Rydberg aggregates in a one-dimensional geometry. *Phys. Rev. Lett.*, 112:013002, Jan 2014. URL: http://link.aps.org/doi/10.1103/PhysRevLett.112.013002, doi:10.1103/PhysRevLett.112.013002.

[122] Martin Gärttner, Kilian P. Heeg, Thomas Gasenzer, and Jörg Evers. Dynamic formation of rydberg aggregates at off-resonant excitation. *Phys. Rev. A*, 88:043410, Oct 2013. URL: https://link.aps.org/doi/10.1103/PhysRevA.88.043410, doi:10.1103/PhysRevA.88.043410.

[123] A. Urvoy, F. Ripka, I. Lesanovsky, D. Booth, J. P. Shaffer, T. Pfau, and R. Löw. Strongly correlated growth of Rydberg aggregates in a vapor cell. *Phys. Rev. Lett.*, 114:203002, May 2015. URL: http://link.aps.org/doi/10.1103/PhysRevLett.114.203002, doi:10.1103/PhysRevLett.114.203002.

[124] Natalia R. de Melo, Christopher G. Wade, Nikola Šibalić, Jorge M. Kondo, Charles S. Adams, and Kevin J. Weatherill. Intrinsic optical bistability in a strongly driven rydberg ensemble. *Phys. Rev. A*, 93:063863, Jun 2016. URL: https://link.aps.org/doi/10.1103/PhysRevA.93.063863, doi:10.1103/PhysRevA.93.063863.

[125] C. Carr, R. Ritter, C. G. Wade, C. S. Adams, and K. J. Weatherill. Nonequilibrium phase transition in a dilute rydberg ensemble. *Phys. Rev. Lett.*, 111:113901, Sep 2013. URL: https://link.aps.org/doi/10.1103/PhysRevLett.111.113901, doi:10.1103/PhysRevLett.111.113901.

[126] F. Letscher, O. Thomas, T. Niederprüm, M. Fleischhauer, and H. Ott. Bistability versus metastability in driven dissipative Rydberg gases. *Phys. Rev. X*, 7:021020, May 2017. URL: https://link.aps.org/doi/10.1103/PhysRevX.7.021020, doi:10.1103/PhysRevX.7.021020.

[127] N. Šibalić, C. G. Wade, C. S. Adams, K. J. Weatherill, and T. Pohl. Driven-dissipative many-body systems with mixed power-law interactions: Bistabilities and temperature-driven nonequilibrium phase transitions. *Phys. Rev. A*, 94:011401, Jul 2016. URL: https://link.aps.org/doi/10.1103/PhysRevA.94.011401, doi:10.1103/PhysRevA.94.011401.

[128] N. R. de Melo, C. G. Wade, N. Šibalić, J. M. Kondo, C. S. Adams, and K. J. Weatherill. Intrinsic optical bistability in a strongly driven rydberg ensemble. *Phys. Rev. A*, 93:063863, Jun 2016. doi:10.1103/PhysRevA.93.063863.

[129] D. Weller, A. Urvoy, A. Rico, R. Löw, and H. Kübler. Charge-induced optical bistability in thermal rydberg vapor. *Phys. Rev. A*, 94:063820, Dec 2016. URL: https://link.aps.org/doi/10.1103/PhysRevA.94.063820, doi:10.1103/PhysRevA.94.063820.

[130] G Günter, H Schempp, M Robert-de Saint-Vincent, V Gavryusev, S Helmrich, C S Hofmann, S Whitlock, and M Weidemüller. Observing the dynamics of dipole-mediated energy transport by interaction-enhanced imaging. *Science (New York, N.Y.)*, 342(6161):954–6, 2013. URL: http://www.sciencemag.org/content/342/6161/954.abstracthttp://www.ncbi.nlm.nih.gov/pubmed/24200814, doi:10.1126/science.1244843.

[131] Jeonghun Lee, Phatthamon Kongkhambut, and T. F. Gallagher. Excitonlike exchange in two-photon transitions of pairs of cold rb rydberg atoms. *Phys. Rev. A*, 96:061401, Dec 2017. URL: https://link.aps.org/doi/10.1103/PhysRevA.96.061401, doi:10.1103/PhysRevA.96.061401.

[132] M. Hoening, W. Abdussalam, M. Fleischhauer, and T. Pohl. Antiferromagnetic long-range order in dissipative Rydberg lattices. *Phys. Rev. A*, 90:021603, Aug 2014. URL: https://link.aps.org/doi/10.1103/PhysRevA.90.021603, doi:10.1103/PhysRevA.90.021603.

[133] Tony E. Lee, H. Häffner, and M. C. Cross. Antiferromagnetic phase transition in a nonequilibrium lattice of rydberg atoms. *Phys. Rev. A*, 84:031402, Sep 2011. URL: https://link.aps.org/doi/10.1103/PhysRevA.84.031402, doi:10.1103/PhysRevA.84.031402.

[134] Sebastian Diehl, A Micheli, A Kantian, B Kraus, H P Büchler, and P Zoller. Quantum states and phases in driven open quantum systems with cold atoms. *Nature Physics*, 4(11):878–883, 2008.

[135] Carlos Pérez-Espigares, Matteo Marcuzzi, Ricardo Gutiérrez, and Igor Lesanovsky. Epidemic dynamics in open quantum spin systems. *Phys. Rev. Lett.*, 119:140401, Oct 2017. URL: https://link.aps.org/doi/10.1103/PhysRevLett.119.140401, doi:10.1103/PhysRevLett.119.140401.

[136] Andreas Geißler, Ivana Vasić, and Walter Hofstetter. Condensation versus long-range interaction: Competing quantum phases in bosonic optical lattice systems at near-resonant rydberg dressing. *Phys. Rev. A*, 95:063608, Jun 2017. URL: https://link.aps.org/doi/10.1103/PhysRevA.95.063608, doi:10.1103/PhysRevA.95.063608.

[137] Stefano Rossotti, Martina Teruzzi, Davide Pini, Davide Emilio Galli, and Gianluca Bertaina. Quantum critical behavior of one-dimensional soft bosons in the continuum. *Phys. Rev. Lett.*, 119:215301, Nov 2017. URL: https://link.aps.org/doi/10.1103/PhysRevLett.119.215301, doi:10.1103/PhysRevLett.119.215301.

[138] J. B. Balewski, A. T. Krupp, A. Gaj, S. Hofferberth, R. Löw, and T. Pfau. Rydberg dressing: Understanding of collective many-body effects and implications for experiments. *New J. Phys.*, 16:063012, 2014. URL: http://dx.doi.org/10.1088/1367-2630/16/6/063012, doi:10.1088/1367-2630/16/6/063012.

[139] B DeMarco and D S Jin. Onset of Fermi Degeneracy in a Trapped Atomic Gas. *Science*, 285(5434):1703 LP – 1706, sep 1999. URL: http://science.sciencemag.org/content/285/5434/1703.abstract.

[140] C S Hofmann, G Günter, H Schempp, N L M Müller, A Faber, H Busche, M Robert-de Saint-Vincent, S Whitlock, and M Weidemüller. An experimental approach for investigating many-body phenomena in Rydberg-interacting quantum systems, 2013. URL: http://dx.doi.org/10.1007/s11467-013-0396-7, arXiv:1307.1074, doi:10.1007/s11467-013-0396-7.

[141] Nils Pehoviak. Strongly interacting ultracold potassium atoms via rydberg dressing. Master thesis, University of Heidelberg, 2015.

[142] Silva Mežinska. Sub-doppler spectroscopy of rydberg states of potassium. Master thesis, University of Heidelberg, 2014.

[143] Alexander Sayer. Fiber-based beam-distribution-system for potassium magneto-optical traps. Bachelor thesis, University of Heidelberg, 2014.

[144] Christoph Schweiger. Laser excitation of ultracold potassium rydberg atoms. Bachelor thesis, University of Heidelberg, 2015.

[145] Henrik Hirzler. Analysis and reduction of spectral broadening in high resolution rydberg excitation. Master thesis, University of Heidelberg, 2017.

[146] Emil Pavlov. Setup and characterisation of stable optical traps for ultracold potassium. Master thesis, University of Heidelberg, 2016.

[147] Christoph Hofmann. *Emergence of correlations in strongly interacting ultracold Rydberg gases*. Dissertation, University of Heidelberg, 2013.

[148] Jacob F Sherson, Christof Weitenberg, Manuel Endres, Marc Cheneau, Immanuel Bloch, and Stefan Kuhr. Single-atom-resolved fluorescence imaging of an atomic Mott insulator. *Nature*, 467(7311):68–72, 2010. URL: http://dx.doi.org/10.1038/nature09378, arXiv:arXiv:1006.3799v1, doi:10.1038/nature09378.

[149] Waseem S. Bakr, Jonathon I. Gillen, Amy Peng, Simon Foelling, and Markus Greiner. A quantum gas microscope - detecting single atoms in a Hubbard regime optical lattice. *Changes*, 462:74, nov 2009. URL: http://arxiv.org/abs/0908.0174, arXiv:0908.0174.

[150] Giulia Faraoni. Nonlinear light propagation through a strongly interacting rydberg gas. Master thesis, Universitá di Pisa, 2014.

[151] E. L. Raab, M. Prentiss, Alex Cable, Steven Chu, and D. E. Pritchard. Trapping of Neutral Sodium Atoms with Radiation Pressure. *Physical Review Letters*, 59(23):2631–2634, dec 1987. URL: http://link.aps.org/doi/10.1103/PhysRevLett.59.2631, arXiv:arXiv:1009.2475v1, doi:10.1103/PhysRevLett.59.2631.

[152] H. J. Metcalf and P. Straten. *Laser Cooling and Trapping*. Springer, 2007.

[153] J. Dalibard and C. Cohen-Tannoudji. Laser cooling below the doppler limit by polarization gradients: simple theoretical models. *J. Opt. Soc. Am. B*, 6(11):2023–2045, Nov 1989. URL: http://josab.osa.org/abstract.cfm?URI=josab-6-11-2023, doi:10.1364/JOSAB.6.002023.

[154] Rudolf Grimm, Matthias Weidemüller, and Yurii B. Ovchinnikov. Optical Dipole Traps for Neutral Atoms. *Advances In Atomic, Molecular, and Optical Physics*, 42:95–170, jan 2000. URL: https://www.sciencedirect.com/science/article/pii/S1049250X0860186X?via{%}3Dihub, doi:10.1016/S1049-250X(08)60186-X.

[155] Tobias Martin Wintermantel. In-situ fluorescence imaging of ultracold potassium in an optical trap. Master thesis, University of Heidelberg, 2016.

[156] D. Rio Fernandes, F. Sievers, N. Kretzschmar, S. Wu, C. Salomon, and F. Chevy. Sub-Doppler laser cooling of fermionic ^{40}K atoms in three-dimensional gray optical molasses. *EPL (Europhysics Letters)*, 100(6):63001, dec 2012. URL: http://stacks.iop.org/0295-5075/100/i=6/a=63001?key=crossref.3e1a13e0529947724e0e1cb3db028418, doi:10.1209/0295-5075/100/63001.

[157] G. Salomon, L. Fouché, P. Wang, A. Aspect, P. Bouyer, and T. Bourdel. Gray-molasses cooling of ^{39}K to a high phase-space density. *EPL (Europhysics Letters)*, 104(6):63002, dec 2013. URL: http://stacks.iop.org/0295-5075/104/i=6/a=63002?key=crossref.68bf1c53d0aafa4a08720ea37c9f8b1f, doi:10.1209/0295-5075/104/63002.

[158] G. Salomon, L. Fouché, S. Lepoutre, A. Aspect, and T. Bourdel. All-optical cooling of ^{39}K to bose-einstein condensation. *Phys. Rev. A*, 90:033405, Sep 2014. URL: https://link.aps.org/doi/10.1103/PhysRevA.90.033405, doi:10.1103/PhysRevA.90.033405.

[159] T G Tiecke. Properties of Potassium. *Physics (College. Park. Md).*, 02(20):1–14, 2010. URL: http://staff.science.uva.nl/{~}walraven/walraven/Publications{_}files/PotassiumProperties.pdf.

[160] Alda Arias, Stephan Helmrich, Christoph Schweiger, Lynton Ardizzone, Graham Lochead, and Shannon Whitlock. Versatile, high-power 460 nm laser system for rydberg excitation of ultracold potassium. *Opt. Express*, 25(13):14829–14839, Jun 2017. URL: http://www.opticsexpress.org/abstract.cfm?URI=oe-25-13-14829, doi:10.1364/OE.25.014829.

[161] Wenchao Xu and Brian DeMarco. Velocity-selective electromagnetically-induced-transparency measurements of potassium rydberg states. *Phys. Rev. A*, 93:011801, Jan 2016. URL: https://link.aps.org/doi/10.1103/PhysRevA.93.011801, doi:10.1103/PhysRevA.93.011801.

[162] C. S.E. van Ditzhuijzen, A. F. Koenderink, L. D. Noordam, and H.B. van Linden van den Heuvell. Simultaneous position and state measurement of rydberg atoms.

The European Physical Journal D - Atomic, Molecular, Optical and Plasma Physics, 40(1):13–17, Oct 2006. URL: https://doi.org/10.1140/epjd/e2006-00140-1, doi:10.1140/epjd/e2006-00140-1.

[163] Lynton Ardizzone. Long-term frequency stabilization of a laser used for rydberg excitation. Bachelor thesis, University of Heidelberg, 2015.

[164] Eric D. Black. An introduction to Pound-Drever-Hall laser frequency stabilization. *American Journal of Physics*, 69(1):79–87, dec 2001. URL: http://aapt.scitation.org/doi/10.1119/1.1286663, doi:10.1119/1.1286663.

[165] R. V. Pound. Electronic frequency stabilization of micowave oscillators. *Rev. Sci. Instrum.*, 17(1946):490–505, nov 1946. URL: https://doi.org/10.1063/1.1770414, doi:10.1063/1.1770414.

[166] R. Potvliege and C. Adams. Photo-ionization in far-off-resonance optical lattices. *New Journal of Physics*, 8(8):163, 2006. URL: http://stacks.iop.org/1367-2630/8/i=8/a=163.

[167] M. Saffman and T. G. Walker. Analysis of a quantum logic device based on dipole-dipole interactions of optically trapped rydberg atoms. *Phys. Rev. A*, 72:022347, Aug 2005. URL: https://link.aps.org/doi/10.1103/PhysRevA.72.022347, doi:10.1103/PhysRevA.72.022347.

[168] Xiaopeng Li and S Das Sarma. Exotic topological density waves in cold atomic Rydberg-dressed fermions. *Nature Communications*, 6(May):7137, 2015. URL: http://arxiv.org/abs/1501.05320$\delimiter"026E30F$nhttp://dx.doi.org/10.1038/ncomms8137$\delimiter"026E30F$nhttp://www.nature.com/doifinder/10.1038/ncomms8137, doi:10.1038/ncomms8137.

[169] A. W. Glaetzle, R. Nath, B. Zhao, G. Pupillo, and P. Zoller. Driven-dissipative dynamics of a strongly interacting Rydberg gas. *Phys. Rev. A*, 86:043403, 2012. URL: http://link.aps.org/doi/10.1103/PhysRevA.86.043403, doi:10.1103/PhysRevA.86.043403.

[170] P Fabritius. Equilibrium and quench dynamics in a fermi-hubbard ladder. Master thesis, University of Heidelberg, 2017.

[171] M O Scully and M S Zubairy. *Control theory and physiological feedback mechanisms*. Williams & Wilkins, 1997.

[172] T F Gallagher. *Rydberg Atoms. Cambridge Monographs on Atomic, Molecular and Chemical Physics*. Cambridge: Cambridge University Press, 1994.

[173] C. J. Lorenzen and K. Niemax. Quantum Defects of the $n^2P_{1/2,3/2}$ Levels in ^{39}K I and ^{85}Rb I. *Physica Scripta*, 27(4):300–305, apr 1983. URL: http://stacks.iop.org/1402-4896/27/i=4/a=012?key=crossref.ab8abbacc20bd35dd7263afa47cbb98d, doi:10.1088/0031-8949/27/4/012.

[174] N. Šibalić, J.D. Pritchard, C.S. Adams, and Weatherill. K.J. Arc: An open-source library for calculating properties of alkali rydberg atoms. *Computer Physics Communications*, 220:319 – 331, 2017. URL: http://www.sciencedirect.com/science/

article/pii/S0010465517301972, doi:https://doi.org/10.1016/j.cpc.2017.06.015.

[175] Sarah E Anderson and Georg Raithel. Ionization of Rydberg atoms by standing-wave light fields. *Nature Communications*, 4:2967, dec 2013. URL: http://dx.doi.org/10.1038/ncomms3967http://10.0.4.14/ncomms3967.

[176] R. J. Le Roy. Energy levels of a diatomic near dissociation. In R. F. Barrow, D. A. Long, and D. J. Millen, editors, *Molecular Spectroscopy: Volume 1*, volume 1, pages 113–176. The Royal Society of Chemistry, 1973. URL: http://dx.doi.org/10.1039/9781847556684-00113, doi:10.1039/9781847556684-00113.

[177] Robert J. Buehler and Joseph O. Hirschfelder. Bipolar expansion of coulombic potentials. *Phys. Rev.*, 83:628–633, Aug 1951. URL: https://link.aps.org/doi/10.1103/PhysRev.83.628, doi:10.1103/PhysRev.83.628.

[178] C L J Valliant. *Long-Range Interactions in One- and Two-Electron Rydberg Atoms*. Dissertation, Durham University, 2014.

[179] A. Dalgarno and W.D. Davison. The calculation of van der waals interactions. In D.R. Bates and Immanuel Estermann, editors, *Advances in Atomic and Molecular Physics*, volume 2 of *Advances in Atomic and Molecular Physics*, pages 1 – 32. Academic Press, 1966. URL: http://www.sciencedirect.com/science/article/pii/S006521990860216X, doi:https://doi.org/10.1016/S0065-2199(08)60216-X.

[180] Daniel Cano and József Fortágh. Nonadditive potentials between three rydberg atoms. *Phys. Rev. A*, 86:043422, Oct 2012. URL: https://link.aps.org/doi/10.1103/PhysRevA.86.043422, doi:10.1103/PhysRevA.86.043422.

[181] I. I. Beterov, I. I. Ryabtsev, D. B. Tretyakov, and V. M. Entin. Quasiclassical calculations of blackbody-radiation-induced depopulation rates and effective lifetimes of rydberg ns, np, and nd alkali-metal atoms with $n \leq 80$. *Phys. Rev. A*, 79:052504, May 2009. URL: https://link.aps.org/doi/10.1103/PhysRevA.79.052504, doi:10.1103/PhysRevA.79.052504.

[182] Michael Fleischhauer and Jonathan P Marangos. Electromagnetically induced transparency: Optics in coherent media. *Rev. Mod. Phys.*, 77(April):633–673, 2005. URL: http://scitation.aip.org/getabs/servlet/GetabsServlet?prog=normal&id=RMPHAT000077000002000633000001&idtype=cvips&gifs=yes, doi:10.1103/RevModPhys.77.633.

[183] Sadaf Sultana and M. Suhail Zubairy. Effect of finite bandwidth on refractive-index enhancement and lasing without inversion. *Phys. Rev. A*, 49:438–448, Jan 1994. URL: https://link.aps.org/doi/10.1103/PhysRevA.49.438, doi:10.1103/PhysRevA.49.438.

[184] M D Lukin, M Fleischhauer, R Cote, L M Duan, D Jaksch, J I Cirac, and P Zoller. Dipole blockade and quantum information processing in mesoscopic atomic ensembles. *Phys. Rev. Lett.*, 87:037901, 2001. doi:10.1103/PhysRevLett.87.037901.

[185] E. Urban, T. A. Johnson, T. Henage, L. Isenhower, D. D. Yavuz, T. G. Walker, and M. Saffman. Observation of Rydberg blockade between two atoms. *Nature Physics*, 5(2):110–114, jan 2009. URL: http://dx.doi.org/10.1038/nphys1178http://10.0.4.14/nphys1178https://www.nature.com/articles/nphys1178{#}supplementary-information, arXiv:0805.0758, doi:10.1038/nphys1178.

[186] Alpha Gaëtan, Yevhen Miroshnychenko, Tatjana Wilk, Amodsen Chotia, Matthieu Viteau, Daniel Comparat, Pierre Pillet, Antoine Browaeys, and Philippe Grangier. Observation of collective excitation of two individual atoms in the Rydberg blockade regime. *Nature Physics*, 5(2):115–118, jan 2009. URL: http://dx.doi.org/10.1038/nphys1183http://10.0.4.14/nphys1183https://www.nature.com/articles/nphys1183{#}supplementary-information, arXiv:0810.2960, doi:10.1038/nphys1183.

[187] D. Jaksch, J. I. Cirac, P. Zoller, S. L. Rolston, R. Côté, and M. D. Lukin. Fast quantum gates for neutral atoms. *Phys. Rev. Lett.*, 85:2208–2211, Sep 2000. URL: https://link.aps.org/doi/10.1103/PhysRevLett.85.2208, doi:10.1103/PhysRevLett.85.2208.

[188] L. Isenhower, M. Saffman, and K. Mølmer. Multibit c k not quantum gates via rydberg blockade. *Quantum Information Processing*, 10(6):755, Sep 2011. URL: https://doi.org/10.1007/s11128-011-0292-4, doi:10.1007/s11128-011-0292-4.

[189] J. Zeiher, P. Schauß, S. Hild, T. Macrì, I. Bloch, and C. Gross. Microscopic characterization of scalable coherent Rydberg superatoms. *Phys. Rev. X*, 5:031015, 2015. URL: https://link.aps.org/doi/10.1103/PhysRevX.5.031015, doi:10.1103/PhysRevX.5.031015.

[190] H. Labuhn, D. Barredo, S. Ravets, S. de Léséleuc, T. Macrì, T. Lahaye, and A. Browaeys. Tunable two-dimensional arrays of single Rydberg atoms for realizing quantum Ising models. *Nature*, 534:667–670, 2016. doi:10.1038/nature18274.

[191] Peter Schauß, Marc Cheneau, Manuel Endres, Takeshi Fukuhara, Sebastian Hild, Ahmed Omran, Thomas Pohl, Christian Gross, Stefan Kuhr, and Immanuel Bloch. Observation of spatially ordered structures in a two-dimensional Rydberg gas. *Nature*, 491(7422):87–91, 2012. arXiv:1209.0944, doi:10.1038/nature11596.

[192] Ditte Møller, Lars Bojer Madsen, and Klaus Mølmer. Quantum gates and multiparticle entanglement by rydberg excitation blockade and adiabatic passage. *Phys. Rev. Lett.*, 100:170504, Apr 2008. URL: https://link.aps.org/doi/10.1103/PhysRevLett.100.170504, doi:10.1103/PhysRevLett.100.170504.

[193] Vladan Vuletic. When superatoms talk photons. *Nature Physics*, 2:801, dec 2006. URL: http://dx.doi.org/10.1038/nphys469http://10.0.4.14/nphys469.

[194] F. Robicheaux and J. V. Hernández. Many-body wave function in a dipole blockade configuration. *Phys. Rev. A*, 72:063403, Dec 2005. URL: https://link.aps.org/doi/10.1103/PhysRevA.72.063403, doi:10.1103/PhysRevA.72.063403.

[195] C. Ates, T. Pohl, T. Pattard, and J. M. Rost. Antiblockade in rydberg excitation of an ultracold lattice gas. *Phys. Rev. Lett.*, 98:023002, Jan 2007. URL: https://link.aps.org/doi/10.1103/PhysRevLett.98.023002, doi:10.1103/PhysRevLett.98.023002.

[196] Igor Lesanovsky and Juan P. Garrahan. Kinetic constraints, hierarchical relaxation, and onset of glassiness in strongly interacting and dissipative Rydberg gases. *Phys. Rev. Lett.*, 111:215305, Nov 2013. URL: http://link.aps.org/doi/10.1103/PhysRevLett.111.215305, doi:10.1103/PhysRevLett.111.215305.

[197] H. Weimer, R. Löw, T. Pfau, and H. P. Büchler. Quantum critical behavior in strongly interacting Rydberg gases. *Phys. Rev. Lett.*, 101:250601, Dec 2008. URL: http://link.aps.org/doi/10.1103/PhysRevLett.101.250601, doi:10.1103/PhysRevLett.101.250601.

[198] T. Pohl, E. Demler, and M. D. Lukin. Dynamical crystallization in the dipole blockade of ultracold atoms. *Phys. Rev. Lett.*, 104:043002, Jan 2010. URL: https://link.aps.org/doi/10.1103/PhysRevLett.104.043002, doi:10.1103/PhysRevLett.104.043002.

[199] Peter Schauß, Johannes Zeiher, Takeshi Fukuhara, S Hild, M Cheneau, T Macr\'\i, T Pohl, Immanuel Bloch, and Christian Groß. Crystallization in Ising quantum magnets. *Science*, 347(6229):1455–1458, 2015.

[200] Subir Sachdev. *Quantum phase transitions*. Cambridge University Press, Cambridge, U.K., 2nd ed edition, 2011. URL: http://proquest.tech.safaribooksonline.de/9781139636001.

[201] Robert Löw, Hendrik Weimer, Ulrich Krohn, Rolf Heidemann, Vera Bendkowsky, Björn Butscher, Hans Peter Büchler, and Tilman Pfau. Universal scaling in a strongly interacting rydberg gas. *Phys. Rev. A*, 80:033422, Sep 2009. URL: https://link.aps.org/doi/10.1103/PhysRevA.80.033422, doi:10.1103/PhysRevA.80.033422.

[202] L. Santos, G. V. Shlyapnikov, P. Zoller, and M. Lewenstein. Bose-Einstein condensation in trapped dipolar gases. *Phys. Rev. Lett.*, 85:1791–1794, 2000. URL: http://arxiv.org/abs/cond-mat/0005009, doi:10.1103/PhysRevLett.85.1791.

[203] N. Henkel, R. Nath, and T. Pohl. Three-Dimensional Roton Excitations and Supersolid Formation in Rydberg-Excited Bose-Einstein Condensates. *Phys. Rev. Lett.*, 104(MAY):195302, 2010. URL: http://link.aps.org/doi/10.1103/PhysRevLett.104.195302, doi:10.1103/PhysRevLett.104.195302.

[204] Alexander W Glaetzle, Marcello Dalmonte, Rejish Nath, Christian Gross, Immanuel Bloch, and Peter Zoller. Designing frustrated quantum magnets with laser-dressed rydberg atoms. *Phys. Rev. Lett.*, 114(17):173002, 2015.

[205] F. Maucher, N. Henkel, M. Saffman, W. Królikowski, S. Skupin, and T. Pohl. Rydberg-induced solitons: Three-dimensional self-trapping of matter waves. *Phys. Rev. Lett.*, 106:170401, Apr 2011. URL: http://link.aps.org/doi/10.1103/PhysRevLett.106.170401, doi:10.1103/PhysRevLett.106.170401.

[206] A W Glaetzle, R M W van Bijnen, P Zoller, and W Lechner. A coherent quantum annealer with Rydberg atoms. *Nature Communications*, 8:15813, jun 2017. URL: http://dx.doi.org/10.1038/ncomms15813http://10.0.4.14/ncomms15813https://www.nature.com/articles/ncomms15813{#}supplementary-information.

[207] Jens Honer, Hendrik Weimer, Tilman Pfau, and Hans Peter Büchler. Collective many-body interaction in Rydberg dressed atoms. *Phys. Rev. Lett.*, 105:160404, Oct 2010. URL: http://link.aps.org/doi/10.1103/PhysRevLett.105.160404, doi:10.1103/PhysRevLett.105.160404.

[208] Marcin Płodzień, Graham Lochead, Julius de Hond, N. J. van Druten, and Servaas Kokkelmans. Rydberg dressing of a one-dimensional bose-einstein condensate. *Phys. Rev. A*, 95:043606, Apr 2017. URL: https://link.aps.org/doi/10.1103/PhysRevA.95.043606, doi:10.1103/PhysRevA.95.043606.

[209] Rick Mukherjee, Thomas C. Killian, and Kaden R. A. Hazzard. Accessing rydberg-dressed interactions using many-body ramsey dynamics. *Phys. Rev. A*, 94:053422, Nov 2016. URL: https://link.aps.org/doi/10.1103/PhysRevA.94.053422, doi:10.1103/PhysRevA.94.053422.

[210] Y. Y. Jau, A. M. Hankin, T. Keating, I. H. Deutsch, and G. W. Biedermann. Entangling atomic spins with a Rydberg-dressed spin-flip blockade. *Nature Physics*, 12(1):71–74, jan 2016. URL: http://arxiv.org/abs/1501.03862, arXiv:1501.03862, doi:10.1038/nphys3487.

[211] Johannes Zeiher, Rick van Bijnen, Peter Schauß, Sebastian Hild, Jae-yoon Choi, Thomas Pohl, Immanuel Bloch, and Christian Gross. Many-body interferometry of a Rydberg-dressed spinÂ lattice. *Nature Physics*, 12:1095, aug 2016. URL: http://dx.doi.org/10.1038/nphys3835http://10.0.4.14/nphys3835https://www.nature.com/articles/nphys3835{#}supplementary-information.

[212] Johannes Zeiher, Jae-yoon Choi, Antonio Rubio-Abadal, Thomas Pohl, Rick van Bijnen, Immanuel Bloch, and Christian Gross. Coherent many-body spin dynamics in a long-range interacting ising chain. *Phys. Rev. X*, 7:041063, Dec 2017. URL: https://link.aps.org/doi/10.1103/PhysRevX.7.041063, doi:10.1103/PhysRevX.7.041063.

[213] C. Ates, T. Pohl, T. Pattard, and J. M. Rost. Many-body theory of excitation dynamics in an ultracold Rydberg gas. *Phys. Rev. A*, 76:013413, Jul 2007. URL: https://link.aps.org/doi/10.1103/PhysRevA.76.013413, doi:10.1103/PhysRevA.76.013413.

[214] Amodsen Chotia, Matthieu Viteau, Thibault Vogt, Daniel Comparat, and Pierre Pillet. Kinetic Monte Carlo modeling of dipole blockade in Rydberg excitation experiment. *New Journal of Physics*, 10(4):045031, apr 2008. URL: http://stacks.iop.org/1367-2630/10/i=4/a=045031?key=crossref.a038e6c41dffcad4768f257b031ddb93, arXiv:0803.4481, doi:10.1088/1367-2630/10/4/045031.

[215] D W Schöenleber. Dissipative dynamics in many-body rydberg systems. Master thesis, University of Heidelberg, 2013.

[216] B. P. Lanyon, C. Hempel, D. Nigg, M. Müller, R. Gerritsma, F. Zähringer, P. Schindler, J. T. Barreiro, M. Rambach, G. Kirchmair, M. Hennrich, P. Zoller, R. Blatt, and C. F. Roos. Universal digital quantum simulation with trapped ions. *Science*, 334(6052):57–61, 2011. URL: http://science.sciencemag.org/content/334/6052/57, arXiv:http://science.sciencemag.org/content/334/6052/57.full.pdf, doi:10.1126/science.1208001.

[217] R. Landig, L. Hruby, N. Dogra, M. Landini, R. Mottl, T. Donner, and T. Esslinger. Quantum phases from competing short-and long-range interactions in an optical lattice. *Nature*, 532:476–479, 2016. doi:10.1038/nature17409.

[218] J. E. Johnson and S. L. Rolston. Interactions between Rydberg-dressed atoms. *Physical Review A*, 82(3):033412, sep 2010. URL: http://link.aps.org/doi/10.1103/PhysRevA.82.033412, doi:10.1103/PhysRevA.82.033412.

[219] Weibin Li, Lama Hamadeh, and Igor Lesanovsky. Probing the interaction between rydberg-dressed atoms through interference. *Phys. Rev. A*, 85:053615, May 2012. URL: http://link.aps.org/doi/10.1103/PhysRevA.85.053615, doi:10.1103/PhysRevA.85.053615.

[220] Alexander Carmele, Berit Vogell, Kai Stannigel, and Peter Zoller. Optonanomechanics strongly coupled to a Rydberg superatom: coherent versus incoherent dynamics. *New J. Phys.*, 16(6):63042, 2014.

[221] Jia Wang, Jason N. Byrd, Ion Simbotin, and R. Côté. Tuning Ultracold Chemical Reactions via Rydberg-Dressed Interactions. *Phys. Rev. Lett.*, 113(2):025302, 2014. URL: http://link.aps.org/doi/10.1103/PhysRevLett.113.025302, doi:10.1103/PhysRevLett.113.025302.

[222] S Wüster, C Ates, A Eisfeld, and J M Rost. Excitation transport through Rydberg dressing. *New J. Phys.*, 13(7):073044, 2011. URL: http://stacks.iop.org/1367-2630/13/i=7/a=073044?key=crossref.e5aa4ccbeffdc0e2088bcfebd2384693, doi:10.1088/1367-2630/13/7/073044.

[223] S. Möbius, M. Genkin, A. Eisfeld, S. Wüster, and J. M. Rost. Entangling distant atom clouds through rydberg dressing. *Phys. Rev. A*, 87:051602, May 2013. URL: http://link.aps.org/doi/10.1103/PhysRevA.87.051602, doi:10.1103/PhysRevA.87.051602.

[224] T. Macrì and T. Pohl. Rydberg dressing of atoms in optical lattices. *Phys. Rev. A.*, 89(1):011402(R), 2014. doi:10.1103/PhysRevA.89.011402.

[225] Martin Gärttner, Shannon Whitlock, David W Schönleber, and Jörg Evers. Collective Excitation of Rydberg-Atom Ensembles beyond the Superatom Model. *Phys. Rev. Lett.*, 113:233002, 2014. URL: http://journals.aps.org/prl/abstract/10.1103/PhysRevLett.113.233002, doi:PhysRevLett.113.233002.

[226] S Helmrich, A Arias, N Pehoviak, and S Whitlock. Two-body interactions and decay of three-level Rydberg-dressed atoms. *Journal of Physics B: Atomic, Molecular and Optical Physics*, 49(3):03LT02, 2016. URL: http://stacks.iop.org/0953-4075/49/i=3/a=03LT02.

[227] E. Brion, L. H. Pedersen, and K. Mølmer. Adiabatic elimination in a lambda system. *Journal of Physics A: Mathematical and Theoretical*, 40(5):1033–1043, feb 2007. URL: http://stacks.iop.org/1751-8121/40/i=5/a=011?key=crossref.ea31ad51fffd7ebb5112775b070ce6a0, arXiv:0610056, doi:10.1088/1751-8113/40/5/011.

[228] C. Gaul, B. J. DeSalvo, J. A. Aman, F. B. Dunning, T. C. Killian, and T. Pohl. Resonant rydberg dressing of alkaline-earth atoms via electromagnetically induced transparency. *Phys. Rev. Lett.*, 116:243001, Jun 2016. URL: https://link.aps.org/doi/10.1103/PhysRevLett.116.243001, doi:10.1103/PhysRevLett.116.243001.

[229] H. Schempp, G. Günter, S. Wüster, M. Weidemüller, and S. Whitlock. Correlated exciton transport in rydberg-dressed-atom spin chains. *Phys. Rev. Lett.*, 115:093002, Aug 2015. URL: http://link.aps.org/doi/10.1103/PhysRevLett.115.093002, doi:10.1103/PhysRevLett.115.093002.

[230] B. Zhao, a. W. Glaetzle, G. Pupillo, and P. Zoller. Atomic Rydberg reservoirs for polar molecules. *Physical Review Letters*, 108(19):1–5, 2012. arXiv:arXiv:1112.4170v1, doi:10.1103/PhysRevLett.108.193007.

[231] S. D. Huber and H. P. Büchler. Dipole-Interaction-Mediated Laser Cooling of Polar Molecules to Ultracold Temperatures. *Phys. Rev. Lett.*, 108(May):193006, 2012. URL: http://link.aps.org/doi/10.1103/PhysRevLett.108.193006, doi:10.1103/PhysRevLett.108.193006.

[232] R. E.E. Van Bijnen and T. Pohl. Quantum Magnetism and Topological Ordering via Rydberg Dressing near Förster Resonances. *Physical Review Letters*, 114(24):1–5, 2015. URL: http://arxiv.org/abs/1411.3118http://dx.doi.org/10.1103/PhysRevLett.114.243002, arXiv:arXiv:1411.3118v1, doi:10.1103/PhysRevLett.114.243002.

[233] S Hensler, J Werner, A Griesmaier, P.O. Schmidt, A. Görlitz, T. Pfau, S. Giovanazzi, and K. Rzazewski. Dipolar relaxation in an ultra-cold gas of magnetically trapped chromium atoms. *App. Phys. B.*, 77(8):765–772, 2003. URL: http://arxiv.org/abs/quant-ph/0307184$\delimiter"026E30F$nhttp://www.springerlink.com/openurl.asp?genre=article{&}id=doi:10.1007/s00340-003-1334-0, doi:10.1007/s00340-003-1334-0.

[234] S. Helmrich, A. Arias, and S. Whitlock. Uncovering the non-equilibrium phase structure of an open quantum spin system. *arxiv:1605.08609v3*, mar 2018. URL: http://arxiv.org/abs/1605.08609, arXiv:1605.08609.

[235] R. Heidemann, U. Raitzsch, V. Bendkowsky, B. Butscher, R. Löw, L. Santos, and T. Pfau. Evidence for coherent collective Rydberg excitation in the strong blockade regime. *Physical Review Letters*, 99(16):163601, 2007. doi:10.1103/PhysRevLett.99.163601.

[236] H. Weimer. Variational analysis of driven-dissipative rydberg gases. *Phys. Rev. A*, 91:063401, Jun 2015. URL: https://link.aps.org/doi/10.1103/PhysRevA.91.063401, doi:10.1103/PhysRevA.91.063401.

[237] V. R. Overbeck, M. F. Maghrebi, A. V. Gorshkov, and H. Weimer. Multicritical behavior in dissipative Ising models. *Phys. Rev. A*, 95:042133, Apr 2017. URL: https://link.aps.org/doi/10.1103/PhysRevA.95.042133, doi:10.1103/PhysRevA.95.042133.

[238] F. Letscher, O. Thomas, T. Niederprüm, H. Ott, and M. Fleischhauer. Anomalous excitation facilitation in inhomogeneously broadened rydberg gases. *Phys. Rev. A*, 95:023410, Feb 2017. URL: https://link.aps.org/doi/10.1103/PhysRevA.95.023410, doi:10.1103/PhysRevA.95.023410.

[239] U. Raitzsch, R. Heidemann, H. Weimer, B. Butscher, P. Kollmann, R. Löw, H. P. Büchler, and T. Pfau. Investigation of dephasing rates in an interacting Rydberg gas. *New Journal of Physics*, 11(5):055014, may 2009. URL: http://stacks.iop.org/1367-2630/11/i=5/a=055014?key=crossref.3a996a8fffd5c3d4e342f25b92e11d5d, arXiv:0811.4185, doi:10.1088/1367-2630/11/5/055014.

[240] M. Gärttner, S. Whitlock, D. W. Schönleber, and J. Evers. Semianalytical model for nonlinear absorption in strongly interacting Rydberg gases. *Phys. Rev. A*, 89:063407, Jun 2014. URL: https://link.aps.org/doi/10.1103/PhysRevA.89.063407, doi:10.1103/PhysRevA.89.063407.

[241] F. Brennecke, T. Donner, S. Ritter, T. Bourdel, M. Köhl, and T. Esslinger. Cavity QED with a Bose–Einstein condensate. *Nature*, 450(7167):268–271, 2007. doi:10.1038/nature06120.

[242] Y. O. Dudin, L. Li, F. Bariani, and A. Kuzmich. Observation of coherent many-body Rabi oscillations. *Nature Physics*, 8(11):790 – 794, 2012. doi:doi:10.1038/nphys2413.

[243] R. Gutiérrez, J. P. Garrahan, and I. Lesanovsky. Self-similar nonequilibrium dynamics of a many-body system with power-law interactions. *Phys. Rev. E*, 92:062144, Dec 2015. URL: https://link.aps.org/doi/10.1103/PhysRevE.92.062144, doi:10.1103/PhysRevE.92.062144.

[244] Richard P. Feynman. Simulating physics with computers. *International Journal of Theoretical Physics*, 21(6):467–488, Jun 1982. URL: https://doi.org/10.1007/BF02650179, doi:10.1007/BF02650179.

[245] Alessandro Vespignani and Stefano Zapperi. How self-organized criticality works: A unified mean-field picture. *Phys. Rev. E*, 57:6345–6362, Jun 1998. URL: https://link.aps.org/doi/10.1103/PhysRevE.57.6345, doi:10.1103/PhysRevE.57.6345.

[246] Didier Sornette. *Critical phenomena in natural sciences*. Physics and astronomy online library. Springer, Berlin ; Heidelberg [u.a.], 2nd ed. edition, 2004.

[247] Deepak Dhar. Self-organized critical state of sandpile automaton models. *Phys. Rev. Lett.*, 64:1613–1616, Apr 1990. URL: https://link.aps.org/doi/10.1103/PhysRevLett.64.1613, doi:10.1103/PhysRevLett.64.1613.

[248] Ronald Dickman, Miguel A. Muñoz, Alessandro Vespignani, and Stefano Zapperi. Paths to self-organized criticality. *Brazilian Journal of Physics*, 30:27 – 41, 03 2000. URL: http://www.scielo.br/scielo.php?script=sci_arttext&pid=S0103-97332000000100004&nrm=iso.

[249] B. Drossel and F. Schwabl. Self-organized critical forest-fire model. *Phys. Rev. Lett.*, 69:1629–1632, Sep 1992. URL: https://link.aps.org/doi/10.1103/PhysRevLett.69.1629, doi:10.1103/PhysRevLett.69.1629.

[250] Zeev Olami, Hans Jacob S. Feder, and Kim Christensen. Self-organized criticality in a continuous, nonconservative cellular automaton modeling earthquakes. *Phys. Rev. Lett.*, 68:1244–1247, Feb 1992. URL: https://link.aps.org/doi/10.1103/PhysRevLett.68.1244, doi:10.1103/PhysRevLett.68.1244.

[251] I Manek, Yu.B Ovchinnikov, and R Grimm. Generation of a hollow laser beam for atom trapping using an axicon. *Optics Communications*, 147(1):67 – 70, 1998. URL: http://www.sciencedirect.com/science/article/pii/S0030401897006457, doi:https://doi.org/10.1016/S0030-4018(97)00645-7.

[252] Norman F. Ramsey. A molecular beam resonance method with separated oscillating fields. *Phys. Rev.*, 78:695–699, Jun 1950. URL: https://link.aps.org/doi/10.1103/PhysRev.78.695, doi:10.1103/PhysRev.78.695.